Impact of Non-gravitational Forces on Magellan Orbit Determination

A Historic Mission To Venus

Jayraj A. Inamdar

Technische Universiteit Delft

TU Delft Delft University of Technology

AIUB

Challenge the future

Impact of Non-gravitational Forces on Magellan Orbit Determination

A Historic Mission To Venus

by

Jayraj A. Inamdar

in partial fulfillment of the requirements for the degree of

Master of Science
in Aerospace Engineering

at the Delft University of Technology,
to be defended publicly on Friday September 21, 2018 at 1:00 PM.

Student Number:	4619439	
Project Duration:	November, 2017-July, 2018	
Daily Supervisor(s):	Prof. Dr. Ir. P.N.A.M. Visser,	TU Delft, The Netherlands
	Dr. Stefano Bertone,	Astronomical Institute University of Bern, Switzerland
	Dr. Daniel Arnold,	Astronomical Institute University of Bern, Switzerland
Thesis committee:	Dr. Ir. E.J.O. Schrama,	TU Delft, The Netherlands | Chair
	Dr. Ir. C.J. (Carlos) Simao Ferreira,	TU Delft, The Netherlands | External Examiner
	Prof. Dr. Ir. P.N.A.M. Visser,	TU Delft, The Netherlands
	Dr. Daniel Arnold,	Astronomical Institute University of Bern, Switzerland

Dedicated to my grandmother

Acknowledgment

This report is the culmination of a year-long work carried out at the Astronomical Institute University of Bern, Switzerland. The implementations, necessary for this project, were done as a part of internship program. First and foremost, I would like to thank my supervisor at TU Delft, Dr. Ir. Pieter Visser, for introducing me to this stimulating project, despite of my different master profile, and for his mentorship. His unparalleled guidance during weekly Skype meetings helped me whenever I was stuck somewhere in the project, while at the same time giving me freedom and responsibility to conduct systematic research. Apart from hard skills and POD jargons acquired through this research, I will be taking his valuable lessons on realizing the big picture of a project and to be sufficiently critical towards own's work.

I would like to thank my daily supervisor Dr. Stefano Bertone for his exceptional support and patience during the entire course of this project, especially during my early days with Bernese GNSS Software framework, FORTRAN programming and Linux ecosystem. I would also like to thank him for giving me the freedom to make mistakes and to explore, without which I could not have learned scientific programming so well. I wish him all the best for his new scientific endeavors at Goddard Spaceflight Center, NASA. I would like to thank my daily supervisor Dr. Daniel Arnold for making me an integral part of LEO Gravity research group at AIUB and for always being open to discussions. He was proactive and enthusiastic to clear variety of doubts–from Doppler modeling to LSQ-estimation process in POD. I would also like to thank him for not being easy on me during my first snow fight at Zimmerwald Observatory. I would like to thank Valère for endless entertainment in the office and for helping me with non-gravitational force modeling in Bernese GNSS Software whenever required. I wish him all the best for his new journey at ESA. To my colleagues and now friends, Andreja, Lauren, Pierre, Arturo, and Florian, thanks for letting me be a part of the office shenanigans at AIUB– from ordering a Hawaii pizza for Stefano to having fun on Snow Day. I am confident that there are more mischiefs and adventures waiting for us in future. Lastly, I would like to thank Dr. Sander Goossens (GSFC, NASA) and Dr. Marty Jean-Charles (CNES) for their timely support in validation of Doppler modeling and for sharing their orbit-processing data whenever required.

A big thank you goes to my Gäbelbach flatmates, Aude, Andri, Stefano, Betty, Linda, Terrence for providing me with distractions and good company not only when I wanted them, but also when I needed them. My stay in the beautiful country of Switzerland wouldn't be so memorable without their warmth and friendship. I am sure we will be seeing each other very soon. To my friends in Delft, Shreyas, Abhishek, Thomas, Pratik, Digvijay, thank you for always being there unconditionally.

I would especially like to thank my parents, whose support has been invaluable for any and all of my endeavors. They have, and always will be, my biggest source of motivation and inspiration.

Lastly, I would like to thank Dr. Ir. E.J.O Schrama, Dr. Ir. C. J. (Carlos) Simao Ferreira and Dr. Daniel Arnold for taking the time to read this report and for being on my graduation committee.

Jayraj A. Inamdar
Delft, August 2018

The computations done in this project were carried out on the UBELIX Cluster of University of Bern, Switzerland. The author is thankful for the excellent IT infrastructure and timely support, kindly provided by AIUB.

Cover Image Source: `https://hdwallsource.com/venus-wallpaper-hd-62405.html`

Summary

One of the main objectives of Magellan mission to Venus (1990-1994) was to map the Venusian gravity field. The spacecraft was tracked at periapsis during gravity-field measurement phase by using X-band Doppler links from the Deep Space Network. With a near-circular orbit and periapsis altitude as low as 170 km during gravity cycles (starting from 3rd August, 1994), Magellan tracking data still constitute the main source of information to develop high resolution gravity field models for Venus.

The state-of-art Venusian gravity field model, i.e., SHGJ180U, is now almost two decades old and starts to show its limitations when used to constrain increasingly precise geophysical models of Venus interior and surface processes. New missions (VEX, Akatsuki) have explored Venus since Magellan and computational power has become much more accessible. This motivates the development of a new high resolution gravity field model for Venus, that could be potentially used for planning future missions and to study Venusian geodynamics. The process of developing gravity model requires explicit modeling of all the forces acting on the spacecraft (potential and non-potential forces). In past analyses of Magellan data in the framework of gravity field development, the extensive modeling of non-gravitational/ surface forces (in particular the forces induced by radiation pressures and air-drag) was left relatively unexplored due to lacking knowledge of Magellan's attitude and material properties. As a result, past orbit analyses have limited the spacecraft modeling to a simple cannon-ball which is eventually corrected by a set of scaling factors.

AIUB is working since years on the precise orbit determination and gravity recovery from observation data of Low-Earth orbiters (LEOs) and has recently extended their expertise for gravity field analysis of Venus. The work done in this project shall support an ongoing Magellan reprocessing efforts at AIUB. The main objective of this project was to analyze the impact of non-gravitational forces and spacecraft model on orbit determination of Magellan. A development version of AIUB's Bernese GNSS Software was used for orbit determination and tracking data processing. However, considering the novelty of deep space processing capabilities in Bernese GNSS Software and challenges in Magellan tracking data processing, the main goal of this thesis was supported by four objectives: 1) Verification and Validation of current implementation for non-gravitational forces in Bernese GNSS Software v5.3, 2) Characterization of challenges in Doppler processing, 3) Development and implementation of macro-model and attitude laws for Magellan, 4) Investigation of the impact of surface forces and spacecraft model on orbit determination.

Verification and Validation (V & V) was done in three steps. First, the correct physical behavior of the implemented models was verified, followed by "back of the envelope" validation. Second, V & V was further supported with orbit determination tests, with only the initial conditions being estimated, where the sensitivity of orbits for two different days, with different orbit characteristics, was assessed with each surface force switched on one at a time. Third, the orbit sensitivity to each surface force was analyzed by estimating additional set of parameters, such as constant empirical accelerations and Piecewise Constant Accelerations (PCAs), along with the initial conditions. From the first step, the magnitude and direction of acceleration due to each surface force was found to be in excellent agreement with the expected physical behavior and "back of the envelope" calculations. From the second step, it was confirmed that the implemented surface models affect the orbit mainly along expected axis of orbital reference frame (for e.g.: the along-track component of the orbit is sensitive to acceleration due to drag). However, it was observed that orbit of one day was more sensitive to the surface forces than of the other day. This observation was further supported by estimation of additional parameters, which showed that the estimated values of the parameters were more sensitive for the day with high orbit sensitivity to the surface forces. It was concluded that the likely reason is the choice of fixed values C_D and C_R which suggested that the values were "more correct" for one day than the other. Nevertheless, the implemented surface forces were verified and validated, and any modeling defect arising from surface forces can be suspected due to incorrect assumptions of C_D and C_R values.

While the next milestone of the project was to estimate Doppler-based orbits, processing Magellan's tracking data is not a straightforward task. The inherent problems in the tracking data, such as ramp error, were accompanied with several unforeseeable issues/bottlenecks that were not solved on time. As a result, one objective of this project was to characterize the bottlenecks in Doppler-based orbit determination for future investigations.

One of the objectives for this project was to use an extended macro-model, with moving solar panels, and implement attitude based on limited information on the orbit design of gravity phase. A 3D CAD model of Magellan was developed by using commercially available software Autodesk 360 with reference to the dimensions of the major components available in the literature. Based on the 3D CAD model, a 16-plate macro-model, that specifies the plate-area of each surface component, was created. To compensate for the lack of information on attitude, two assumptions, minimum drag and maximum power output, were implemented and tested with the extended macro-model.

The impact of non-gravitational forces and choice of spacecraft model was assessed with two different approaches: 1) Analysis by empirical and pseudo-stochastic parameters with SPICE orbits as observations, and 2) Doppler-based orbit determination, with real tracking data as observations. For the first approach, the estimated empirical acceleration biases and Piecewise Constant Accelerations (PCAs) for each spacecraft model, over one month starting from 8-August-1993, were compared to those of setup with surface forces inactive. For the second approach, the drag scaling factor for each spacecraft model and attitude assumption was estimated along with six initial conditions over a data arc containing Days 146 and 147 of 1994 of SPICE positions. Subsequently, the drag scale estimate, corresponding to each spacecraft model, was multiplied with fixed $C_D = 1.25$ and the estimation of only the six initial conditions was done with Doppler observations. From first approach, the statistical properties of PCAs and acceleration biases show that the parameters are more sensitive to the presence of non-gravitational forces than to the choice of spacecraft model and attitude assumption. This is further supported by Doppler-based orbit determination test (or the second approach), where the presence of surface forces, irrespective of the spacecraft model, has larger impact on the orbits than the spacecraft models. Speaking of choosing the favorable attitude assumption, a clear conclusion cannot be yet derived for two reasons: 1) a test with "tuned" C_D and C_R is not yet done, and 2) the test was not done for several data arcs, which could otherwise give a clear picture.

Speaking purely from orbit determination perspective, it was observed that the Doppler residuals are significantly less for each LSQ-adjustment when surface forces are active. Smaller Doppler residuals are strong indication of better estimation of initial conditions during LSQ-adjustment. Furthermore, the position residuals show that the surface forces have immediate impact on the orbit determination. Significant reduction in standard deviation and RMS of position residuals, in along-track and cross-track direction, by introducing a simple surface force modeling with cannonball affirms that the precise orbit determination of Magellan is characterized by accurate modeling of the surface forces. However, non-gravitational force models are often the largest source of errors in orbit determination. This is also true in case of Venus orbiters due to imperfect atmosphere models and lack of accurate physical properties of spacecraft, particularly C_D and C_R. However, these imperfections can be easily tuned by estimation of scaling factors for surface forces. It was indirectly shown through Doppler-based orbit determination that "scaled" values of C_D alone are capable of improving the orbits, where the Doppler residuals in the orbit propagation alone is significantly less than those for an orbit setup without surface forces. This means that, out of all the parameters for surface force accelerations, C_D and C_R are the most important parameters that determine the quality of non-gravitational force modeling.

This work done in this project assess the impact of spacecraft macro-model by implementing attitude assumptions, when not explicitly available. As a result, the outcome of this project could aid towards formulating a guideline to improve non-gravitational force modeling (or to choose effective orbit parametrization that can enhance the quality of the recovered orbits) when limited or no information is available on the probe's geometrical and optical properties and/or its attitude, which is often the case for old (and sometimes recent) planetary missions.

List of Abbreviations

3D	Three Dimensional
AIUB	Astronomical Institute University of Bern
ASCII	American Standard Code for Information Interchange
AMD	Angular Momentum Desaturation
BNMS	Bus Neutral Mass Spectrometer
CHAMP	CHallenging Mini-satellite Payload
CoM	Center-of-Mass
CPR	Cycle Per Revolution
CAD	Computer Aided Design
CNES	Centre National d'études Spatiales
D/O	Degree & Order
DD:MM:YYYY	Date format in Day: Month: Year
DSN	Deep Space Network
ESA	European Space Agency
E-PRP	Emitted Planetary Radiation Pressure
FEM	Forward Equipment Module
GPS	Global Position System
GINS	Geodesy by Simultaneous Digital Integration
GSFC	Goddard Spaceflight Center
GNSS	Global Navigation Satellite System
GRAIL	Gravity Recovery and Interior Laboratory
HGA	High Gain Antenna
HH:MM:SS	Time format Hour: Minute: Second
IUS	Inertial Upper Stage
ICRS	International Celestial Reference System
ITRF	International Terrestrial Reference Frame
IAU	International Astronomical Union
JPL	Jet Propulsion Laboratory, NASA
LGA	Low Gain Antenna
LOS	Line-of-Sight
LSQ	Least Squares Adjustment
LEO	Low Earth Orbit
MGA	Medium Gain Antenna
NASA	National Aeronautics & Space Administration
NAIF	Navigation and Ancillary Information Facility
ONMS	Orbital Neutral Mass Spectrometer
OINMS	Orbital Ion Neutral Mass Spectrometer
OUVS	Orbiter Ultraviolet Spectrometer
OIR	Orbiter Infrared Radiometer
OAD	Orbiter Atmospheric Drag
ODF	Orbit Data File
PVO	Pioneer Venus Orbiter
POD	Precise Orbit Determination
PCA	Piece-wise Constant Acceleration
PRP	Planetary Radiation Pressure
R-PRP	Reflected Planetary Radiation Pressure
R.H.S	Right Hand Side
RSW	Radial(R), Along-track (S), Cross-track (W)
SAR	Synthetic Aperture Radar

SRP	Solar Radiation Pressure
SZA	Solar Zenith Angle
ST	Station Time (UTC)
TT	Terrestrial Time
TDB	Barycentric Dynamical Time
UTC	Coordinated Universal Time
USA	United States of America
VIRA	Venus International Reference Atmosphere
Venus-GRAM	Venus Global Reference Atmosphere Model
VOI	Venus Orbit Insertion
VLBI	Very Long Baseline Interferometry

List of Symbols

In case the units are not specified, it means that the units can vary depending on the implementation.

Symbol	Description	Unit
A	Spacecraft area	$[m^2]$
A	Illuminated surface area of the spacecraft	$[m^2]$
$A_{\oplus}$	Planetary area	$[m^2]$
c	Speed of light	$[ms^{-1}]$
C_D	Drag coefficient	$[-]$
$\bar{C}_{n,m}$	Geopotential coefficient	$[-]$
C_R	Radiation coefficient of spacecraft's body (reflectivity coefficient)	$[-]$
$D_{\odot}$	Distance of Planet's center to the solar center	$[m]$
f	Eclipse parameter	$[-]$
f_g	Geometric shadowing function	
GM	Gravity constant times planetary mass	$[m^3s^{-2}]$
g	Acceleration due to gravity	$[ms^{-2}]$
h	Height above the geoid	$[km]$
H_0	Atmospheric scale height	$[km]$
h_c	Height of center beam from Planetary surface	$[km]$
h_b	Height of bottom beam from Planetary surface	$[km]$
K_2	Love number	$[-]$
L	Longitudinal resolution	$[deg]$
M	Latitudinal resolution	$[deg]$
M	Modulation ratio	$[-]$
$M_{SC,D}$	Drag scaling factor	$[-]$
$M_{SC,SRP}$	SRP scaling factor	$[-]$
$M_{SC,PRP}$	PRP scaling factor	$[-]$
m	Order of spherical harmonic expansion	$[-]$
m	Spacecraft mass	$[kg]$
n	Degree of spherical harmonic expansion	$[-]$
$P_{\odot}$	Mean solar radiation pressure at spacecraft's location	$[Nm^{-2}]$
P_{R-PRP}	R-PRP	$[Nm^{-2}]$
P_{E-PRP}	E-PRP	$[Nm^{-2}]$
$\bar{P}_{n,m}$	Normalized associated Legendre function of degree n and order m	$[-]$
q_i	i^{th} empirical and/or pseudo-stochastic parameter	$[-]$
r	Spacecraft's geocentric distance from central planet	$[m]$
R	Mean semi-major axis of ellipsoid planet	$[m]$
R	Universal gas constant	$[Jmol^{-1}K^{-1}]$
$R_{\oplus}$	Planetary radius	$[m]$
$\bar{S}_{n,m}$	Geopotential coefficient	$[-]$
t_{1s}	Signal emission start time at DSN station	$[s]$
t_{1e}	Signal emission end time at DSN station	$[s]$
t_{2s}	Signal reception start time at spacecraft	$[s]$
t_{2e}	Signal reception end time at spacecraft	$[s]$
T	Integration time	$[s]$
T	Mean atmospheric temperature	$[K]$
V_{atm}	Spacecraft's velocity w.r.t. atmosphere	$[ms^{-1}]$

Vector	Description	Unit
$\mathbf{A}$	Jacobi matrix	
$\mathbf{a}$	Non-conservative acceleration vector	$[ms^{-2}]$

$\mathbf{a_1}$	Empirical acceleration vector	$[ms^{-2}]$
$\hat{\mathbf{e}}_{\mathbf{x}}$	Unit vector along X-axis	$[-]$
$\hat{\mathbf{e}}_{\mathbf{y}}$	Unit vector along Y-axis	$[-]$
$\hat{\mathbf{e}}_{\mathbf{z}}$	Unit vector along Z-axis	$[-]$
$\hat{\mathbf{e}}_{\odot}$	Spacecraft-to-Sun unit vector	$[-]$
$\mathbf{F}(\mathbf{X})$	Non-linear function of parameter X	
$\mathbf{L}^{'}$	Real observation vector	
$\hat{\mathbf{r}}_{Earth}$	Spacecraft-to-Earth unit vector	$[-]$
$\hat{\mathbf{n}}_{ELE}$	Surface normal unit vector	$[-]$
$\hat{\mathbf{n}}_{j}$	j^{th} macro-model plate normal unit vector	$[-]$
$\ddot{\mathbf{r}}$	Acceleration vector	$[ms^{-2}]$
$\mathbf{r}$	Position vector	$[m]$
$\ddot{\mathbf{r}}_{SRP}$	SRP acceleration vector	$[ms^{-2}]$
$\hat{\mathbf{r}}_{\odot}$	Sun-to-spacecraft unit vector	$[-]$
$\ddot{\mathbf{r}}_{E-PRP}$	E-PRP acceleration vector	$[ms^{-2}]$
$\ddot{\mathbf{r}}_{Drag}$	Drag acceleration vector	$[ms^{-2}]$
$\ddot{\mathbf{r}}_{R-PRP}$	R-PRP acceleration vector	$[ms^{-2}]$
$\hat{\mathbf{r}}_{\oplus}$	Source-to-spacecraft unit vector	$[-]$
$\hat{\mathbf{r}}_{ELE\odot}$	Surface element-to-Sun unit vector	$[-]$
$\hat{\mathbf{u}}$	Unit vector of incoming particles	$[-]$

Greek	**Description**	**Unit**
α	Planetary albedo	$[-]$
β	Angle between orbital plane and the Sun	$[deg]$
β	Spacecraft visibility angle	$[rad]$
δ	Diffusion coefficient	$[-]$
$\epsilon^{'}$	Planetary emissivity	$[-]$
ϵ	LSQ-fit error or residual	
π	Mathematical constant	$[-]$
$\epsilon_{d,j}$	Diffuse reflection coefficient of panel j	$[-]$
$\epsilon_{s,j}$	Specular reflection coefficient of panel j	$[-]$
Δ	Difference operator	$[-]$
ψ	Solar illumination angle	$[rad]$
λ	Longitude	$[deg]$
ϕ	Latitude	$[deg]$
∇	Nabla operator	$[-]$
τ	One-way light time	$[s]$
μ	Molecular weight of one gas particle	$[kgmol^{-1}]$
ρ	Atmospheric density	$[kgm^{-3}]$
ρ_{∞}	Free-stream atmospheric density	$[kgm^{-3}]$
$\Phi_{\odot 1AU}$	Solar flux at 1 AU	$[Wm^{-2}]$
η	Geometric parameter	$[-]$

Contents

List of Tables

List of Figures

1

Introduction

This chapter provides first an overview about Magellan mission and its objectives in Sections 1.1 and 1.2 respectively. Subsequently, a brief explanation of gravity recovery procedure is provided in Section 1.3 with relevance to Magellan mission. Later, challenges encountered during previous work for dynamic orbit modeling in framework of gravity recovery is discussed in Section 1.4 and a potential improvement using macro-model for spacecraft is discussed in Section 1.5. Finally, based on the synthesis of the literature study, thesis objectives and scope are defined in Section 1.8, followed by an overview of the report layout in Section 1.9.

1.1. Magellan Mission

Magellan spacecraft was launched on May 4, 1989 and arrived at Venus on August 10, 1990. The primary objectives of the mission were to map an entire Venusian surface with Synthetic Aperture Radar (SAR) and to obtain the topographic relief of the planet [1]. Magellan is a special interplanetary mission that had achieved several feats and had set a new benchmark for the preceding exploration missions. The spacecraft was first of its kind to be launched from a space shuttle (Space Shuttle Atlantis) and was the first probe to successfully demonstrate the aerobraking maneuver, that was required to circularize its orbit for achieving mission objectives. Named in the honor of 16th century Portuguese explorer, Ferdinand Magellan, the spacecraft arrived at Venus to “explore” the veiled planet and its surface features. For this purpose, the entire Magellan mission was divided into “Cycles” and each Cycle lasted for one full rotation of Venus beneath the spacecraft (approximately 243 Earth days). The mission time-line is given in Table 1.1.

Date	Milestone
4-May-1989	Launch
10-Aug-1990	Venus Orbit Insertion
15-Sept-1990	Cycle 1: Radar Mapping (left-looking)
15-May-1991	Cycle 2: Radar Mapping (right-looking)
15-Jan-1992	Cycle 3: Radar Mapping (left-looking)
14-Sept-1992	Cycle 4: Gravity Data Acquisition
24-May-1993	Aerobraking Maneuver
3-Aug-1993	Cycle 5: Gravity Data Acquisition
30-Aug-1994	Cycle 6: Windmill Experiment
12-Oct-1994	Termination Maneuver
13-Oct-1994	Signal Loss (end of mission)

Table 1.1: Magellan mission time-line

An interesting fact to be mentioned here is that Magellan was originally conceived with the primary intention of mapping the Venusian surface with SAR. Magellan’s initial orbit was highly elliptical (294 Km × 8,543 km). Being in a polar orbit, the spacecraft moved from northern to southern hemisphere (and vice versa) with an orbital period of approximately 3 hours, 15 minutes [11]. During the part of its orbit closest to Venus, Magellan's SAR mapped a swath of the Venusian surface (approximately 17-28 km wide) and radioed a ribbon-like strip of radar data back to Earth at the end of every orbit. As Venus rotates once every 243 Earth days, the spacecraft was able to map almost 84% of the planet's surface by the end of the first Cycle [11]. It then continued to map for the next two Cycles which allowed 98% of Venusian surface to be mapped. With a different "look angle", the radar mapping data acquired during the SAR phase allowed the scientists to construct 3D views of the Venusian surface.

After a successful completion of SAR mapping phase, the mission was extended to collect the information on gravity field of Venus, starting from September 1992, by capturing the Doppler shift in tracking frequency due to gravity anomalies that affected the spacecraft's motion in its orbit [12]. During this phase, the High Gain Antenna (HGA), that was initially nadir-pointing, was oriented towards Earth and the spacecraft was tracked continually by the Deep Space Network (DSN), at least when a favorable line-of-sight visibility was available. However, the elliptical orbit, designed for the primary phase, was not suitable for uniform measurement of global gravity field [8]. At the end of fourth Cycle, that marked the beginning gravity acquisition phase, Magellan was lowered into the Venusian atmosphere at its periapsis using then-untried maneuver known as Aerobraking that caused the orbit to be nearly circular (180 Km × 541 km) due to the increasing atmospheric drag force acting on the spacecraft that lowered the orbital height, and consequently its apoapsis [6]. With low altitudes, and a circular orbit, Magellan circled around Venus more quickly, completing one orbit in 94 minutes. Nevertheless, at the start of fifth Cycle (post-aerobraking phase), Magellan was ready to be tracked by DSN, providing tracking data full with high-resolution information of the Venusian gravity field.

After April 1994, Magellan began its sixth, and final phase, of the mission. During this phase, in addition to mapping the gravity field, Magellan conducted "Windmill" experiment during which its solar panels were broadly aligned with the orbital path to act as paddles (or sails) while being impacted by molecules of the upper Venusian atmosphere. The torque generated by such impact was countered by firing the thrusters that prevented the spacecraft from spinning around. The thruster data during this experiment provided valuable information on the lift, drag and atomic oxygen-surface interaction for the first time in a free-molecular gas flow conditions [13]. On October 11, 1994, Magellan began its mission termination maneuver and plunged into Venusian atmosphere resulting into loss of signal.

1.2. The Spacecraft

A desire to build a low-cost, high performance vehicle motivated the design team to take advantage of already-proven technologies and components from historic missions. Table 1.2 shows an inventory of the heritage that Magellan derives upon.

Component	Source
Medium Gain Antenna (MGA)	Mariner Mars 1971
High-and Low Gain Antennas (HGA, LGA)	Voyager
Equipment bus	Voyager
Radio-frequency traveling-wave tube assemblies	Ulysses
Attitude-control computer	Galileo
Command and data subsystem	Galileo
Thruster rockets	Voyager
Electric-power distribution unit	Galileo
Power control unit	P-80 Satellite
Pyrotechnic control	Galileo
Solid-rocket motor design	Space Shuttle Payload Assist Module (PAM)
Propellant tank design	Space Shuttle Auxilliary Power Unit (APU)

Table 1.2: Magellan's equipment inventory and the missions from which they are derived [1].

Weighing approximately 3,453 kg while mounted on the cargo-bay of Space Shuttle Atlantis, the spacecraft consists of the following major components:

1. Antennas (HGA, MGA, LGA and Altimeter)
2. Forward Equipment Module (FEM)
3. Equipment bus
4. Solar panels
5. Solid-rocket orbit-insertion motor
6. Propulsion module
7. Inertial Upper Stage (IUS) adapter

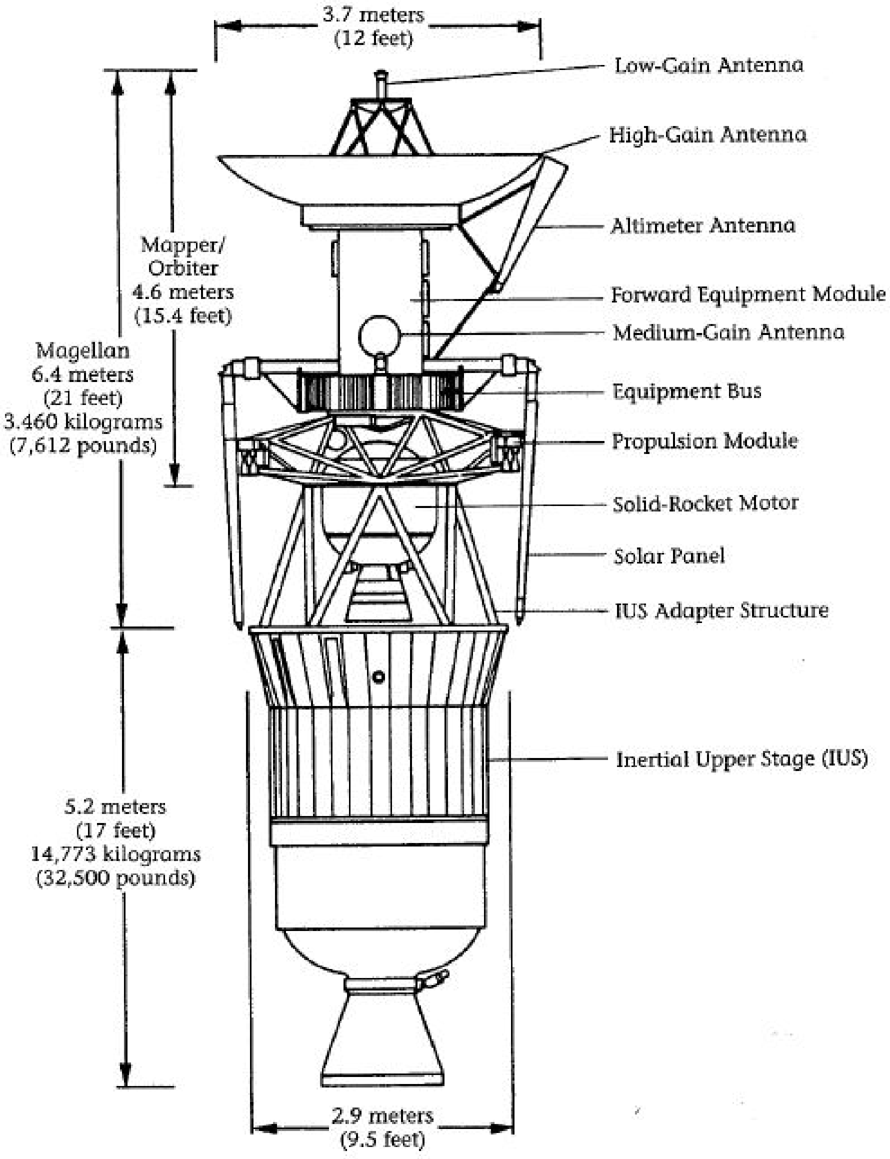

Figure 1.1: Top view of Magellan when loaded into cargo-bay [1]

Referring to Figure 1.1, the parabolic, dish-shaped HGA, of about 3.7 m in diameter, is the primary antenna for radar operations. During SAR phase, the HGA carried out SAR measurements of the Venusian surface and transmitted the radar data back to Earth during DSN tracking. Subsequent to SAR-phase, HGA's primary purpose was reduced to DSN tracking only. Nevertheless, in addition to tracking and transmission of scientific measurements, HGA transmitted spacecraft health data and received commands during manual control/emergencies.

The MGA is the cone shaped structure on the top side of the bus and was mainly used for sending engineering data and to receive commands from ground stations during Venus Orbit Insertion (VOI) maneuver and for cruise period of 15-months. Once Magellan was in the orbit, MGA was intended to be used only during situations when spacecraft pointing was not correct for DSN tracking.

The LGA, mounted on top of HGA dish structure, was placed at that specific position so that no part of the spacecraft can interfere with its broad beam. The main purpose of LGA was to support mission operations during critical situations due to its wide beam-width that allowed the spacecraft to be tracked even during incorrect orientation of HGA with respect to Earth.

The altimeter antenna, mounted on the side of FEM was used exclusively for radar altimetry. During mapping Cycle, the altimeter antenna was "looking" directly at the planet to provide one-dimensional measurements of heights of the Venusian surface features.

The FEM, shown in Figure 1.2, is a box-like structure below the HGA assembly and houses radar electronics, equipment for radio telecommunication, attitude-control unit, batteries and power-conditioning unit. The two sides of the FEM contain louvers for thermal regulation. Furthermore, the outer surface of FEM is highly reflective to shield the internal components from intense sunlight. In addition to housing the electro-mechanical equipments, FEM supports the solar panel boom. The panels are free to rotate about an axis that passes through the boom from tip of one panel to another. Two pair of solar senors, each mounted at the tip of one panel, function together with a control package in the equipment bus to maintain the panels' orientation towards Sun.

Immediately below the FEM, a 10-sided equipment bus houses the liquid-propulsion system and flight computers. The section of Magellan, from HGA to the equipment bus, collectively form the orbiter that embarked upon a journey to Venus; whereas the IUS was discarded immediately after Magellan was jettisoned into an interplanetary trajectory.

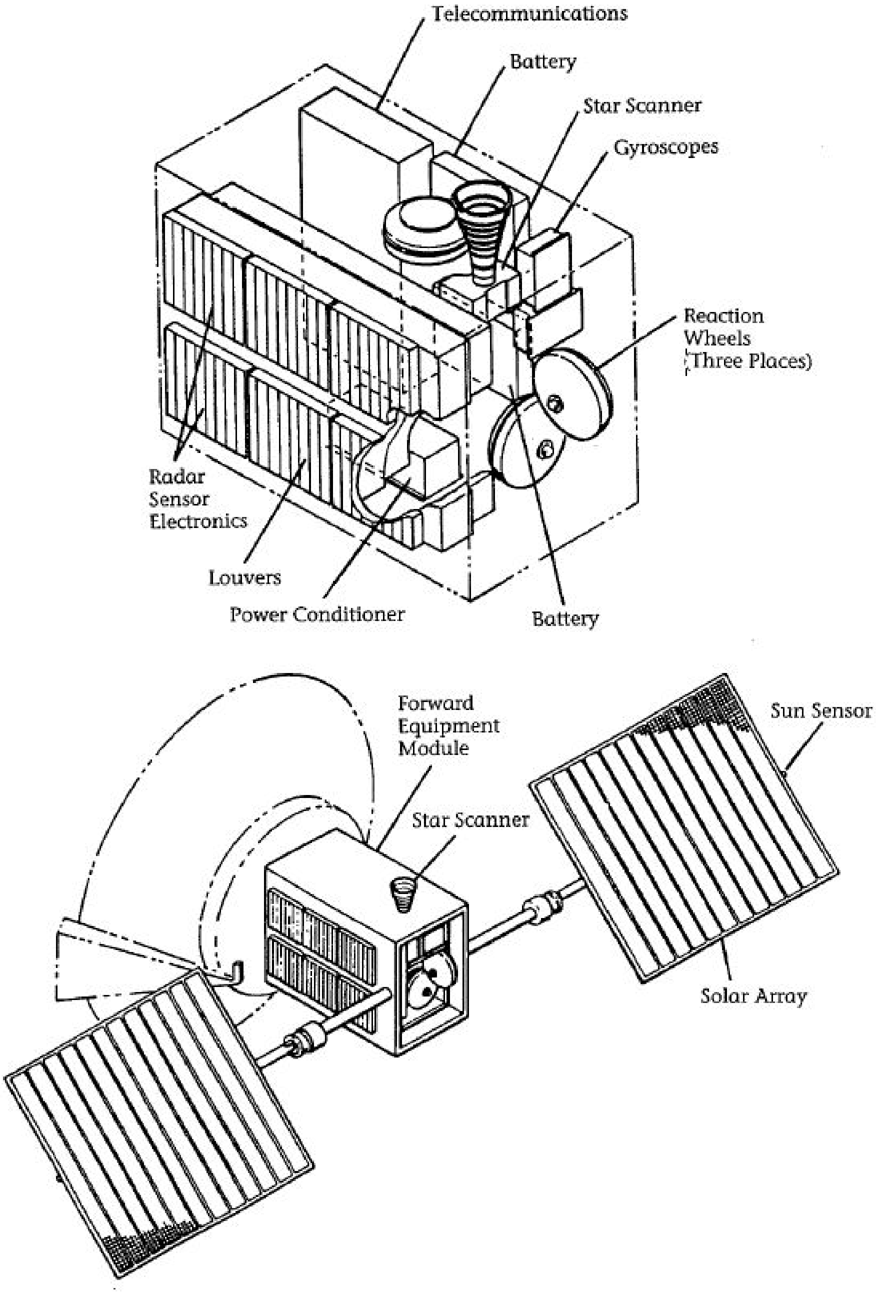

Figure 1.2: FEM assembly (top) and illustration of FEM with solar panels (bottom) [1]

1.3. Gravity Recovery

Any spacecraft orbiting a planet with non-uniform spherical mass distribution will experience a varying gravitational acceleration, depending on the latitude and longitude of the planet over which the spacecraft is moving in its orbit. For example, a spacecraft “senses” increased gravitational pull over a region with stronger gravity that causes it to speed up slightly (and vice versa, when it passes over a region with slightly weaker gravity). This change in acceleration, due to gravity, creates a Doppler shift in the tracking frequency due to an apparent change in Line-of-Sight (LOS) velocity between the DSN and spacecraft. Thus, in context of inter-planetary missions, tracking data are used to measure gravitational perturbations that affect the motion of the spacecraft in its orbit. These perturbations due to zone-varying gravity field of the central body can be stored separately in form of spherical harmonic coefficients of geopotential model that represents the gravity field of the planet [14].

While gravity models are important to understand the planetary interior and its geodynamics, they are also widely used for Precise Orbit Determination and planning navigation operations for future missions [15]. Tracking data of Magellan (in particular, the gravity acquisition phase starting from Cycle 5) have been extensively used in combination with the tracking data of Pioneer Venus Orbiter (PVO) to develop high-resolution gravity models, up to Degree and Order (D/O) 180, by Barriot et al., (1998) and Konopliv et al., (1999) [4], [12].

It is important to mention that the process of developing a gravity model requires an explicit modeling of all the forces that are acting on the spacecraft in its orbit.The first step to be taken is the pre-processing of tracking data to eliminate outliers and bad observations due to poor observation geometry and large maneuvers. Once the observations are prepared, dynamic models are introduced as “apriori” to account for all the accelerations that are acting on the spacecraft at a given instant of time in its orbit. The main goal of using dynamical models is to estimate spacecraft’s state from known initial conditions, by means of orbit integration and LSQ-adjustment, thus allowing to produce a computed value of observation. Once the best orbits are achieved that give minimum differences between observed and computed values of observations, it is possible to co-estimate the gravity field along with the spacecraft state by allowing the gravity terms (or coefficients) to be treated as free parameters.

However, the dynamic orbit modeling of a planetary probe which experiences various perturbations in a relatively unknown environment is a complex matter. In particular, uncertainties in the modeling of non-gravitational forces can introduce errors that can cause the results of integration to deviate from the actual motion of the spacecraft. These errors in the orbit estimation can eventually affect the quality of estimated gravity field that can render it useless for future use[1]. Thus, it is understood that accurate modeling of non-gravitational forces, while being a challenging task, is necessary to obtain best gravity field model.

1.4. Non-gravitational Force Modeling Challenges

The lack of extensive information on Venusian atmosphere was a major bottleneck for the development of early iterations of Venusian gravity models. The tracking data sets produced by PVO, in its early mission phase, were used by Ananda et al, (1980) and Williams et al., (1983) to develop first series of gravity models up to D/O 7 and 10 respectively [16], [17]. However, data surrounding few minutes of periapsis pass had to be removed due to poor knowledge on the Venusian atmosphere [17]. Venus’ atmosphere is thick and PVO’s periapsis was located at an altitude of about 160 km [18]. As a result, it was expected that the atmosphere will have a strong impact on the trajectory of the orbiter in periapsis region, which at the that time couldn’t be modeled extensively. By the time Magellan’s tracking data from primary mission phase were available, Keating et al, [1985] developed an empirical atmosphere model, VIRA[2], for Venus from in-situ observations of PVO, Venera 9, 10, 11, 12, and Mariner 4, 5, 10 [19]. The first extensive use of VIRA model was done in the framework of supporting the design of aerobraking maneuver for Magellan, that was required to have near- circular orbit for high quality gravity measurement, see Wong et al., (1994) [20]. The empirical values of the atmospheric scale heights, given by VIRA, were used to estimate the base densities at spacecraft altitudes by implementing simple exponential density model [20]. Since then, VIRA has been extensively used in the dynamic orbit modeling of Venus orbiters that aimed to develop high resolution gravity models [4].

However, the scale heights and densities of VIRA model are up to 250 km altitude [19]. This means that one has to extrapolate the given values of densities to estimate base densities at spacecraft altitudes beyond 250 km. In an effort to develop the state-of-art gravity model for Venus, Konopliv et al., (1999) implemented a similar exponential density model as that of Wong et al., (1994) to extrapolate densities for altitudes higher than 250 km [6]. However, they further investigated the consistency of such extrapolation by estimating base densities for PVO POD within the VIRA altitude range over a period of one day and then by comparing them with those of VIRA. It was concluded from the comparison that extrapolation leads to underestimation of atmospheric density at a given altitude (see Figure 1.3),

---

[1] The errors in non-gravitational force modeling are absorbed by the estimated gravity field coefficients.

[2] VIRA- Venus International Reference Atmosphere

which suggests that the aerodynamic forces can be undermined leading to error in the orbit solution [6]. The inconsistencies were even more severe for orbit modeling of Magellan mission. The primary reason for such inconsistency is the empirical nature of the VIRA model, that was developed using the parametrization that was best suited for PVO–which was one of the data source to develop VIRA.

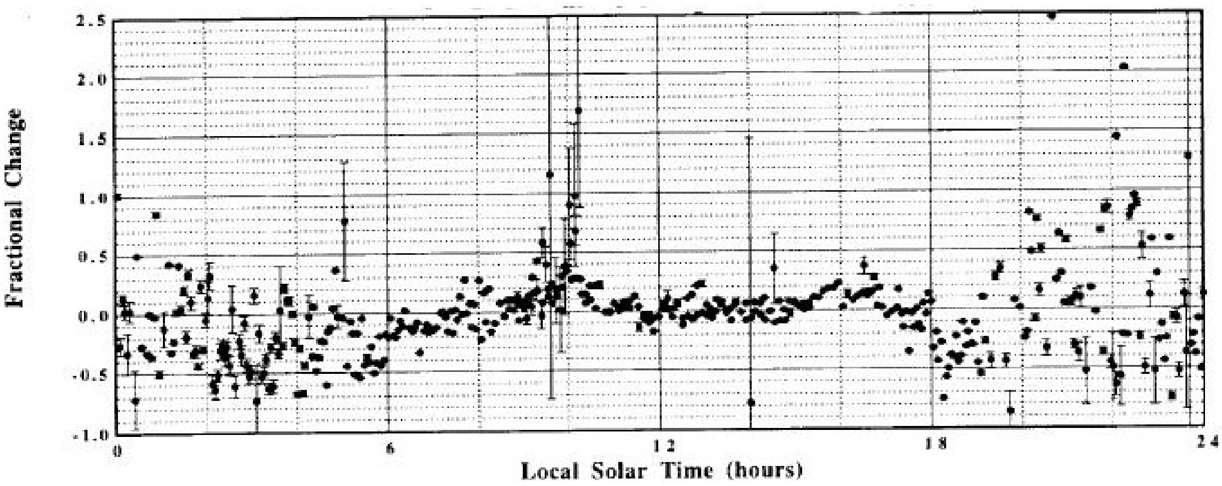

Figure 1.3: Difference between PVO density solutions and VIRA values at an altitude of 140 Km for local solar time indicating underestimation of densities for major part of the day [6].

Thus, it is expected that the modeling of aerodynamic forces will be far from perfect due to uncertainty associated with atmospheric densities at spacecraft altitudes. While an error-free model is impossible to achieve, one can tune the modeling process by setting up empirical parameters (explained extensively in Chapter 2) to minimize (or absorb) the errors due to imperfect densities of empirical atmosphere models.

While radiation forces are independent of the planet's atmospheric properties, errors still arise in the modeling process due to lack of information about exact dimensions of the spacecraft body. Radiation forces are functions of the number of photons bombarding the spacecraft body per square meter [21]. Thus, a detailed modeling of radiation forces is only possible when the physical properties, like dimensions and optical specifications of the spacecraft surfaces, are sufficiently known. The dimensions of major surfaces are well documented by Boyce et al, (1990) for Magellan [1]. Unfortunately, the optical properties, that define the reflectivity and emissivity of the surfaces, are not easily available in the literature due to confidentiality of the mission. In addition to this, lack of attitude information (or quaternions) further makes it difficult to account for the orientation of spacecraft with respect to an inertial reference frame. Being aware of such challenges, previous developments of Venusian gravity models have restricted the radiation force modeling by implementing cannon-ball model for the spacecraft. Briefly speaking, a cannon-ball model is a simplified form factor of the spacecraft that assumes uniform surface properties and assumes that the spacecraft is a non-rotating sphere [21]. Cannon-ball models are used when the spacecraft specifications are unknown and no information on attitude is available. However, such simplified spacecraft model cannot resolve the torques and linear accelerations due to non-gravitational forces and changing orientation of the spacecraft in its local reference frame [22].

1.5. Macro-model Approach

Recently, spacecraft macro-models have been extensively used for non-gravitational force modeling for Earth-based missions [21], [22], [23]. Macro-models are spacecraft models that approximate major parts of the spacecraft body with plates and the orientation of each plate in spacecraft reference frame is specified by normal unit vector (see Figure 1.4).

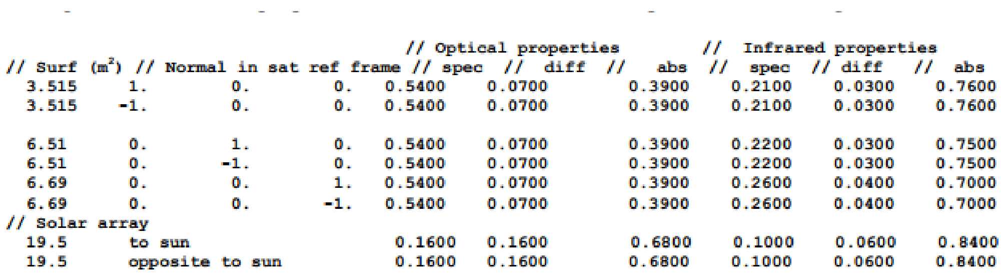

```
                                        // Optical properties        //  Infrared properties
// Surf (m²) // Normal in sat ref frame // spec  //  diff  //    abs  //  spec  // diff   //  abs
  3.515      1.        0.         0.   0.5400   0.0700        0.3900   0.2100   0.0300   0.7600
  3.515     -1.        0.         0.   0.5400   0.0700        0.3900   0.2100   0.0300   0.7600

  6.51       0.        1.         0.   0.5400   0.0700        0.3900   0.2200   0.0300   0.7500
  6.51       0.       -1.         0.   0.5400   0.0700        0.3900   0.2200   0.0300   0.7500
  6.69       0.        0.         1.   0.5400   0.0700        0.3900   0.2600   0.0400   0.7000
  6.69       0.        0.        -1.   0.5400   0.0700        0.3900   0.2600   0.0400   0.7000
// Solar array
  19.5       to sun                     0.1600   0.1600        0.6800   0.1000   0.0600   0.8400
  19.5       opposite to sun            0.1600   0.1600        0.6800   0.1000   0.0600   0.8400
```

Figure 1.4: An example macro-model file for SPOT satellite contains the plate area, plate normal unit vectors, and optical properties [7].

The surface forces on each plate are predicted individually and then are summed to give the total surface forces acting on the spacecraft. Thus, use of spacecraft macro-model allows the non-gravitational forces to be intricately modeled because the orientation of each plate with respect to the direction of the force is considered [21].

However, sufficient knowledge of attitude, that gives the information on spacecraft's orientation with respect to an inertial reference frame at a given epoch, is mandatory to implement macro-models. While precise knowledge of Magellan's attitude is not available in literature, the orbit design of the gravity phase has been documented by Lyons et al (1993) [8].

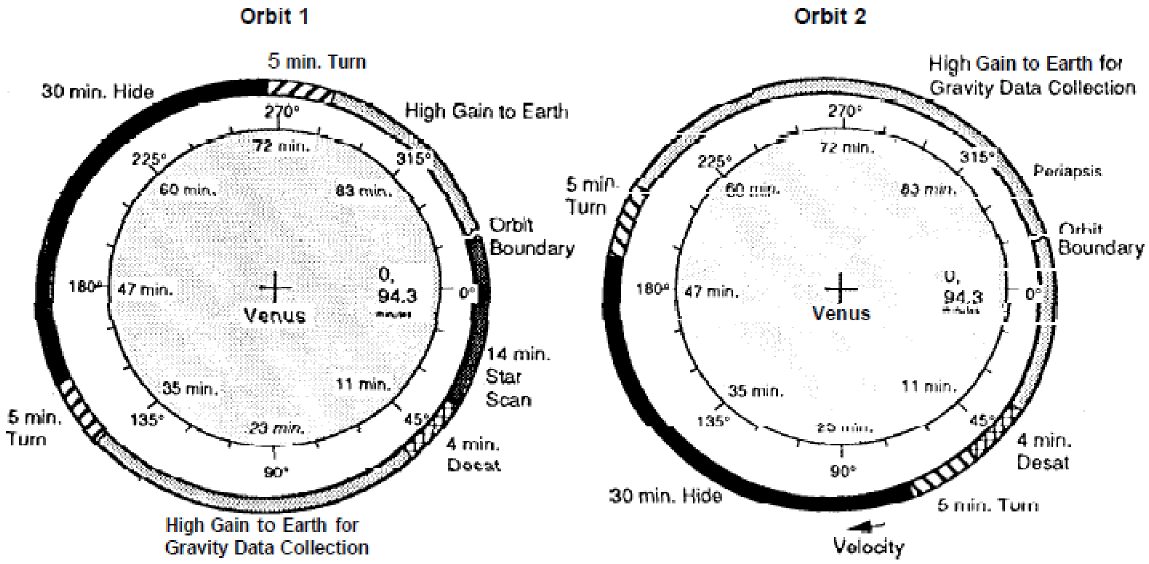

Figure 1.5: Two-Orbit Sequence of Events [8]. The spacecraft is moving clockwise and orbit boundary refers to the point in first orbit before the star tracking event. At the boundary, the spacecraft switches to second orbit as shown on the right.

In a nutshell, the following series of events were planned for the orbit design for gravity phase of the mission, (also, see Figure 1.5 for graphical illustration, starting from Orbit 1 on the left side):

- ⇒ Star scan starts to update attitude knowledge,
- ⇒ Initiate Angular Momentum Desaturation (AMD),
- ⇒ Turn HGA towards Earth for DSN tracking,
- ⇒ Turn to the hide attitude near apoapsis[3],

---

[3] Hide maneuver is the change in attitude of the spacecraft during which the High Gain Antenna (HGA) is pointed towards the Sun, thereby shielding the light-sensitive instruments like star tracker and cool down the spacecraft surface.

- ⇒ Turn HGA towards Sun and hide behind the large parabolic antenna dish,
- ⇒ Turn the HGA towards Earth for DSN tracking,
- ⇒ Switch to Orbit-2 at the orbit boundary,
- ⇒ Initiate AMD,
- ⇒ Turn to hide attitude,
- ⇒ Turn the HGA towards Earth for DSN tracking.

While the sequence of hide event was not well-defined, it is certain that the HGA (Z-axis of the spacecraft reference frame) would be pointed towards the Earth at least during DSN tracking [8]. Furthermore, hide events were rather spurious and had no fixed time-stamps in the orbit[4]. However, to fully define an attitude of the spacecraft at a given epoch, it is necessary to know the orientation of the second axis of the spacecraft reference frame. In this context, Konopliv et al., (1996) briefly discuss that the orientation of solar panels is along the direction of velocity for the gravity phase [6], thereby providing the necessary knowledge of the second axis (Y-axis of the spacecraft reference frame). Thus, we have a reasonable, but not well-defined, details on Magellan's attitude.

1.6. Magellan Doppler Tracking Challenges

Before using the Doppler tracking data to extract scientific information, it is important to filter out bad observations due to plasma interference and undocumented maneuvers. [4]. However, tracking data of Magellan have additional problems that are associated with incorrect ramp and reference frequency recording [6]. There were some undocumented instances between August 1993 and November 1993 where incorrect ramp rates were reported due to round off in the last significant digit of the ramp frequency that can be detected only by analyzing the Doppler residuals. In addition to this, incorrect reference frequencies have been reported from December 1993 to January 1994 that requires an estimation of Doppler bias of about 1 m/s [6].

While Magellan's X-band Doppler frequency spectrum is less affected by solar plasma as compared to S-band spectrum, extreme Sun-Venus-Earth angles associated with Solar Conjunction have corrupted the Doppler data due to which Konopliv et al. had to exclude a month of tracking data in the start of cycle 5 centered around the Conjunction [6], [4]. The corruption of data is mainly associated with increasing noise in the Doppler data due to solar interference during Cycle 5 (see Figure 1.6).

Thus it can be seen that working with Doppler data is not a straight-forward process, and as a first-step in Doppler processing, one needs to characterize the potential challenges in Doppler processing and then attempt to rectify them one-by-one. Nevertheless, as a starting reference, one could refer to Venus Gravity Handbook compiled by Konopliv et al., (1996) to know data arcs containing healthy tracking data [6]. Lastly, previous uses of the orbit determination software used in this project, Bernese GNSS v5.3 (more details can be found in Chapter 4), were mainly for Earth-Moon system, with newly implemented capability for Doppler processing. As a result, it is mandatory to verify and validate Doppler processing for deep space missions, in this case, for Magellan mission to Venus.

---

[4] The duration of hides, including the start-stop time, are available on daily basis starting from Cycle 4 and are well documented in Venus Gravity Handbook [6]

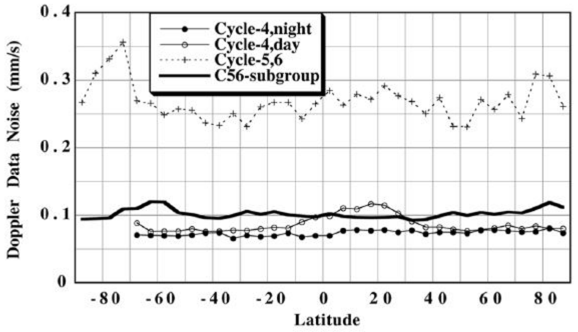

Figure 1.6: Magellan X-band Doppler data noise versus lattitude for each gravity cycle.[4].

1.7. Motivation

The state-of-art Venusian gravity model, SHGJ180U, complete to D/O 180, dates back to 1999–an era when computational power was limited [4]. Due to computational limitations, Konopliv et al., (1999) developed this model in three steps: 1) First a gravity field of D/O 120 was developed; 2) A gravity field of 155 D/O was developed from 120 model; and finally 3) A 180 D/O gravity field model was developed from 155 degree apriori [4]. Thus, each new iteration, with higher degree terms, was developed by freezing the prior known coefficients. However, developing a high resolution gravity field model in steps is not recommended because the higher order terms are weak and highly correlated with each other that are sensed by the spacecraft in combined amplitudes [24]. The error in power spectrum of 180 degree model confirmed this problem associated with freezing the correlated higher frequency terms and one can see the discontinuities in RMS power spectrum in Figure 1.7. Nevertheless, step-wise approach to construct a gravity model was the only possible way-around to deal with output files size as large as 4GB [4].

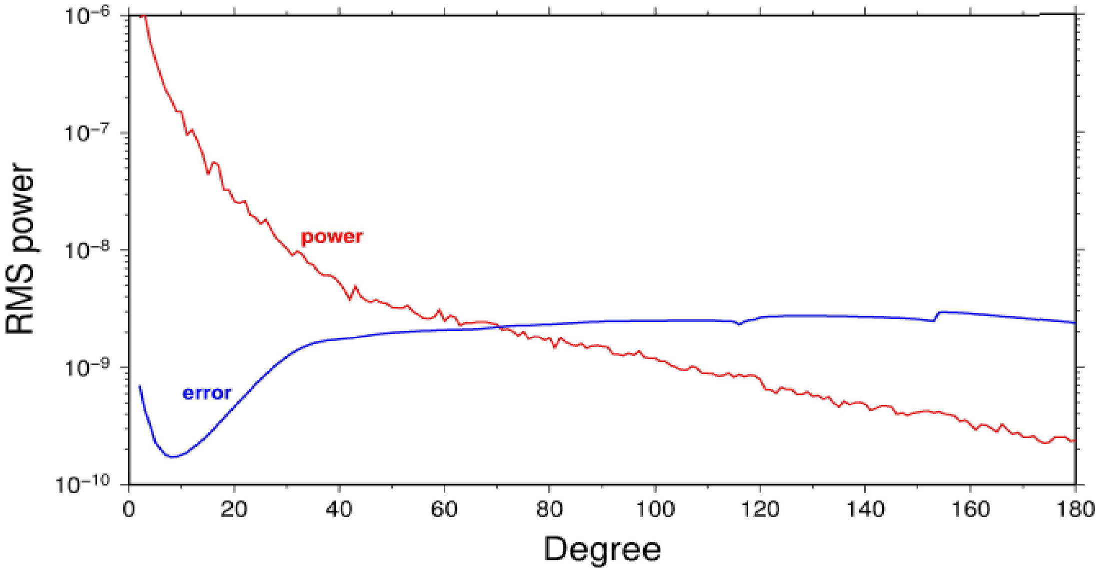

Figure 1.7: RMS power spectrum of 180 degree model showing the breaks in the error spectrum [4].

While the present computer infrastructure can allow for the estimation of gravity field in one single step, modeling of non-gravitational forces is an area that has been relatively left unexplored in the past studies for Venus orbiters. To this date, Venusian gravity models have been developed without extensive modeling for non-gravitational forces due to imperfect knowledge of Venusian atmosphere and spacecraft attitude, and have rather restricted the spacecraft modeling to a simple cannon-ball model. Magellan is an enormous spacecraft (4.9 m × 2.6 m) and one can expect significant influence of non-gravitational forces on the its trajectory due to its larger surfaces [1][5]. Contemporary researches on non-gravitational force modeling, particularly for Earth-based missions, have begun to put a lot of emphasis on the form factor of spacecraft due to the fact that a direct proportionality exists between the magnitude of non-gravitational forces and the exposed area of the spacecraft [21], [23], [22]. As a result, it is important to extend the framework of these studies (in particular, impact of macro-models on modeled acceleration due to surface forces) to support the planned exploration missions to Venus with possible impacts in wide areas of Planetary Sciences [25].

1.8. Objectives & Scope

Based on the synthesis of the literature study, this project aims to explore possible room for improvements in non-gravitational force modeling of Magellan mission in support of Venusian gravity field recovery. Motivated by the prospect of a new high-resolution gravity model for Venus, that could be potentially used for planning future missions and to study the Venusian geodynamics, the main objective of this project is to implement spacecraft macro-model with an attitude law and analyze its impact on the modeled non-gravitational accelerations, and consequently on the estimated orbit solutions. Regarding the attitude law, whose knowledge is also required when using an extended macro-model, this project will base its analysis on limited information available in the literature and then shall attempt to establish a framework upon which the macro-model can be refined further. However, before attempting scientific analysis, the first step is to verify and validate the current implementations of surface forces and Doppler modeling to ensure that the outputs are reliable and valid.

Thus, in a broader framework of gravity field recovery, this project will try to answer the following low-level research question (LQx) by estimating precise orbits for Magellan:

LQ1: How important are the surface force models in the orbit determination of Magellan?

To answer the above question, following objectives (OBJx) are defined for this research:

1. ***OBJ1: Verification and Validation of current implementation for non-gravitational forces in Bernese GNSS Software v5.3.***
2. ***OBJ2: Characterization of challenges in Doppler processing.***
3. ***OBJ3: Development and implementation of macro-model and attitude laws for Magellan.***
4. ***OBJ4: Investigation of the impact of surface forces and spacecraft model on orbit determination.***

1.9. Report Layout

This report is divided into seven main chapters:

- Chapter 1 introduces the background about the Magellan mission and its role in gravity recovery. Furthermore, a compact literature review is covered that highlights the open areas that this project attempts to investigate.
- Chapter 2 introduces the reader to the mathematical backbone of POD and gravity recovery by using DSN tracking data.
- Chapter 3 provides the mathematical framework for the dynamic orbit modeling for non-gravitational forces.
- Chapter 4 introduces the reader to the software framework that is required for this thesis.
- Chapter 5 is dedicated to the Verification & Validation to confirm the robustness of the implemented non-gravitational force models.

---

[5] Aerodynamic forces with magnitudes of $10^{-8}\ km/s^2$ have been reported by using a cannon-ball spacecraft model for Magellan at periapsis altitude of about 220 km [6].

- Chapter 6 presents the results and analyses of the impact of non-gravitational force models on Magellan POD.
- Finally, Chapter 7 wraps up this project with conclusion and recommendations for future work.

2

Precise Orbit Determination

This chapter provides a theoretical overview of POD methodologies. First, equations of motion, representing the trajectory of spacecraft around a planet, are discussed in Section 2.2. Subsequently, contemporary practices to tackle model deficiencies in dynamic orbit model are given in Section 2.3. Finally, Sections 2.4 and 2.6 introduces a conceptual detail on how precise science orbits are obtained from 2-way Doppler tracking data.

2.1. Introduction

Precise Orbit Determination (POD) is an application of Astrodynamics that is used to accurately estimate spacecraft's orbit around a planet. Estimation of spacecraft state vectors is based on a sequence of observations. POD of a spacecraft is usually done by integrating the equations of motion, starting from a reference epoch. The initial condition (or state vector at t_0) given at a reference epoch is propagated in time by integrating the equations of motion to produce predicted (or computed) observations. Generally, this initial orbit is not good but can still serve as a starting point for further orbit improvements. So how is the initial orbit improved? It is important to highlight that the number of tracking observations are usually greater than the parameters to be estimated [26]. As a result, the formulation of orbit determination problem, that relates observations to state vectors, leads to an over-determined system that has more number of equations than the number of unknowns. For this purpose, one can use Least Squares (LSQ) estimator that attempts to minimize the sum of the squares of the residuals [27][1]. In addition to the position and velocity vectors, the state vector can also be composed of empirical forces and measurement model parameters. The apriori components of a state vector are then adjusted in a least squares sense to minimize the observation residuals. Thus for orbit determination, one fundamentally needs:

- Equations of motion that describe (or model) the accelerations due to the forces acting on the spacecraft.
- A system of equation(s) that relates the observed parameters and spacecraft's state vector.
- A Least Squares Estimation algorithm.

Before proceeding towards a recapitulation of its mathematical foundation, it is important to mention that there are three main approaches followed for POD: 1) Dynamical approach, 2) Reduced-dynamic approach, and 3) Kinematic approach. The Kinematic POD requires no dynamical model and purely relies on the strength of observation data and is generally suitable for observations with high data sampling rate, such as Global Positioning System (GPS) techniques [28]. The Dynamical POD uses dynamical models that define the motion of the spacecraft around a central body. However, the accuracy of Dynamic POD is limited by modeling errors, for example, due to inaccurate atmospheric drag model

---

[1] Residual is the difference between an observed value and the computed (or estimated) value that is predicted by the model describing a dynamical system. However, for this thesis, residuals explicitly pertain to the difference between observed value and the computed value of the observations (positions or tracking data).

[29]. In order to overcome the negative impact on orbit determination due to imperfect dynamic models, Reduced-dynamic approach has been widely used in recent years. In this case, additional empirical (and/or stochastic parameters) are set up in the orbit modeling process to absorb mis-modeling errors [30]. A kinematic POD is generally not possible (till this date) for deep-space missions because the tracking observations are in line-of-sight only and are not continuous, and depend on several factors (for example, when the spacecraft is "behind" the planet in which case we have no tracking). On the other hand, a pure dynamical POD will still fail to produce accurate orbits because the dynamical modeling will be far from perfect. As a result, Reduced-dynamic approach is suitable for deep space missions where one has freedom to set up additional empirical/stochastic accelerations to absorb errors due to imperfect modeling. Thus, the approach followed in this research will be mainly based on Reduced-dynamic approach. Now, with a conceptual overview and rationale to follow Reduced-dynamic POD, the next sections shall be focusing on the mathematical back-bone of Reduced-dynamic orbit determination setup used for this thesis.

2.2. Dynamic Orbit Modeling

The motion of a spacecraft (in particular, its center of mass) around a planet is governed by the sum of all forces acting on it. As a result a very detailed modeling of the forces is needed to accurately represent the motion of the spacecraft, which is often given by the equations of motion (one for each axis in a reference frame). In their simplest form, equations of motion in the inertial frame can be represented by eq. (2.1) [26],

$$\ddot{\mathbf{r}} = -GM\frac{\mathbf{r}}{r^3} + \mathbf{a}, \tag{2.1}$$

where

GM → gravity constant times the mass of the planet $[m^3/s^2]$,

$\mathbf{r}$ → spacecraft's geocentric position vector, expressed in the inertial reference frame $[m]$,

$\mathbf{a}$ → accelerations due to non-conservative forces $[m/s^2]$.

The first term of R.H.S of the eq. (2.1) is the gravitational acceleration that is valid for a perfectly spherical body. In reality, a planet's gravity field is complex due to its non-spherical mass distribution and is often represented by an extended geopotential model given by eq. (2.2) [30]

$$V(r,\phi,\lambda) = \frac{GM}{R}\sum_{n=0}^{n_{max}}\left(\frac{R}{r}\right)^{n+1}\sum_{m=0}^{n}\bar{P}_{n,m}(\sin\phi)\,(\bar{C}_{n,m}\cos(m\lambda) + \bar{S}_{n,m}\sin(m\lambda), \tag{2.2}$$

where

r, ϕ, λ → spherical geocentric coordinates (height $[m]$, latitude $[deg]$, longitude $[deg]$),

GM → gravity constant times the mass of the planet $[m^3/s^2]$,

R → the mean semi-major axis of ellipsoidal planet $[m]$,

n, m → the degree and order of the spherical harmonic expansion,

n_{max} → the maximum degree of spherical harmonic expansion,

$\bar{P}_{n,m}$ → normalized associated Legendre function of degree n and order m,

$\bar{C}_{n,m}$, $\bar{S}_{n,m}$ → the normalized spherical harmonic and global gravity field model parameters, respectively.

Thus, eq. (2.1) can be modified for extended gravity potential model as

$$\ddot{\mathbf{r}} = \nabla V + \mathbf{a}, \tag{2.3}$$

Now, **a** of eq.(2.3) contains accelerations due to gravity perturbations such as third body perturbation effects due to the Sun and neighboring planets (also known as potential forces), and non-gravitational forces such as [29] [31]:

- Aerodynamic Drag (AD) due to interaction of neutral atmospheric molecules with spacecraft body.
- Solar Radiation Pressure, (SRP), force due to impact of radiation on the spacecraft emitted by the Sun in visible spectrum.
- Reflected Planetary Radiation Pressure, (R-PRP), due to reflected solar radiation by the planet in visible spectrum.
- Emitted Planetary Radiation Pressure (E-PRP) in infrared spectrum by the planet.
- Infrared emission by the body of the spacecraft.
- Small accelerations due to impulsive thrust and Angular Momentum Dumps (AMD) that are required for orbit and attitude maintenance.
- Small acceleration due to antenna thrust caused by signal transmission.
- Acceleration due to solid tides of the central body.
- Relativistic perturbations due to periapsis precession, geodesic precession and precession due to angular momentum of the rotating planet.

While the above list is not exhaustive, it is important to highlight that aerodynamic and radiation forces are the major contributers to non-gravitational accelerations compared to the other perturbations. In particular for Venus orbiters, with low periapsis altitude, aerodynamic forces can have significant impact on the their orbital motion. Furthermore, Venus' close proximity to the Sun can lead to strong presence of accelerations due to radiation forces. Free-stream atmospheric densities at spacecraft altitudes, required for modeling of aerodynamic forces, are usually obtained from planetary atmospheric models that are empirically constructed from in-situ observations of the orbiters (or probes). Modeling of radiation forces is usually done analytically (a detailed treatment is given in Chapter 3). Thus, accelerations due to non-gravitational forces, i.e. the second term of R.H.S of eq. (2.3), are evaluated by introducing relevant force models for perturbations in the equation of motions.

Finally, one can see that the equations of motion, represented by eq. (2.3), form a system of second order differential equations that can be integrated starting from known a state vector (or initial conditions) at a reference epoch to obtain the spacecraft state at any desired time.

2.3. Reduced-dynamic Orbit Modeling

The foundation of orbit modeling has been introduced to the reader in Section 2.2. It has been repeatedly mentioned that modeling of non-gravitational forces is far from being perfect. However, in order to meet the demand for precise orbits, one has to find a way-around to compensate for the errors in the orbit estimation due to inaccurate force modeling. As a result, a purely dynamic orbit modeling, as given by eq. (2.3), is subjected to the introduction of additional set of empirical and pseudo-stochastic parameters whose purpose is to either absorb errors in acceleration of modeled forces or to compensate for a lack of modeling of a particular force. Keeping this in mind, this section presents a conceptual overview of empirical and pseudo-stochastic parameterizations, introduced in addition to purely dynamical orbit model, that contribute to the process of reduced-dynamic orbit modeling.

A Reduced-dynamic orbit modeling allows the flexibility to fine-tune the orbit model, that can give the best LSQ fit of the observations, by setting up accelerations for additional parameters in the estimation process. Thus, the equations of motion, eq. (2.3) for Reduced-dynamic setup can be re-formulated as

$$\ddot{\mathbf{r}} = \Delta V + \mathbf{a} + \mathbf{a_1}(q_1, q_2, ..., q_n), \tag{2.4}$$

where $q_1, q_2, ..., q_n$ are additional set of empirical and/or pseudo-stochastic parameters.

2.3.1. Empirical Parameters

Constant Accelerations

The constant acceleration (or bias) parameters, one in each RSW-direction, absorb the mean part of the non-modeled acceleration component in radial, along-track and cross-track direction. On the other hand, acceleration biases are particularly effective for absorbing cross-track errors in SRP model for days during which Sun is perpendicular to the orbital plane, i.e. the spacecraft is in constant sunlight. The constant acceleration parameters, when active, are estimated along with initial conditions in the LSQ fit.

1-CPR Accelerations

The errors in non-gravitational forces can induce 1-CPR variations in estimated Kepelerian elements, particularly the errors in node, inclination, argument of periapsis and eccentricity [32]. Therefore, a parametrization is provided in precise orbit determination wherein 1-CPR accelerations are introduced in the orbit model.

2.3.2. Pseudo-stochastic Parameters

It is to be considered that pseudo-stochastic orbit modeling is different from stochastic orbit modeling. While the later is characterized by an orbit (or trajectory) that is modeled by a solution of stochastic differential equations, pseudo-stochastic orbit modeling simply introduces additional parameters that are statistically estimated by apriori known statistical properties that constrain the estimated parameters to user-specified expectations [30].

Instantaneous Velocity Changes (Pulses)

The parameters describing instantaneous velocity changes are referred to as pseudo-stochastic pulses. The orbit parametrization with pulses is characterized by a continuous trajectory between the predefined epochs for pulses, while exhibiting discontinuities in velocities at epochs pertaining to the pulses [33]. This concept can be visualized in Figure 2.1.

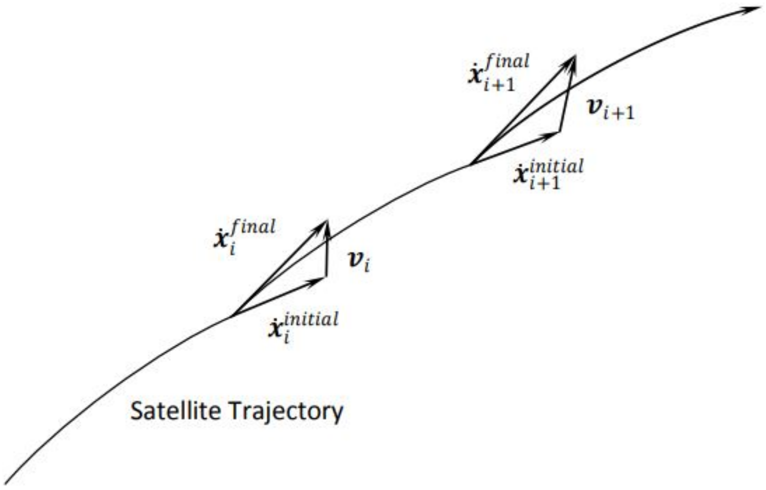

Figure 2.1: Concept of parametrization with pseudo-stochastic pulses. The “initial” state refer to user-specified apriori values (or constraints) and “final” is the estimated state during LSQ fit.

Since pulses represent a sudden change in the magnitude and direction of spacecraft’s velocity, they can be used to compensate for instantaneous velocity changes due to maneuvers. In recent years, it has been a common practice to set up a pulse in each direction of orbital reference frame (radial, along-track and cross-track) for orbit determination of GPS and GLONASS satellites to counter mis-modeling of mainly SRP and aerodynamic drag [34]. Any mis-modeling of SRP can be mitigated by setting up the estimation of pulses for once per orbital revolution. However, in order to compensate for aerodynamic forces, higher number of pulses, estimated at smaller intervals, is required. Estimation of pulses at higher frequencies is not recommended for gravity recovery because of the artificial discontinuities, introduced at velocity level, that can propagate into higher frequency spherical harmonics of geopotential model (see eq. (2.2)) while co-estimating of the gravity field [30][2]. Nevertheless, by constraining the pulses to a reasonable extent, they can be used to compensate for maneuvers given that they are estimated at larger intervals[3].

Piece-wise Constant Accelerations (PCAs)

Before proceeding with presenting a conceptual detail, it is important to note that gravity recovery (or estimation of harmonic coefficients of the potential model) is done simultaneously with the estimation of spacecraft state vector (in particular, position and velocity). As a result, artificial discontinuities in spacecraft velocities must be avoided as much as possible. With this in mind, we already know that setting up pseudo-stochastic pulses in orbit determination is disadvantageous. Therefore, a refined pseudo-stochastic parametrization, Piece-wise Constant Accelerations (PCAs) was developed by Jäggi et al., 2005 [9]. The resultant orbit parametrized with PCAs are continuous at velocity level because the discontinuities are shifted to the derivative of velocity (acceleration) [9]. The procedure to set up PCAs is similar to that for the pulses (i.e. one PCA in each direction in orbital reference frame at a pre-defined epoch).

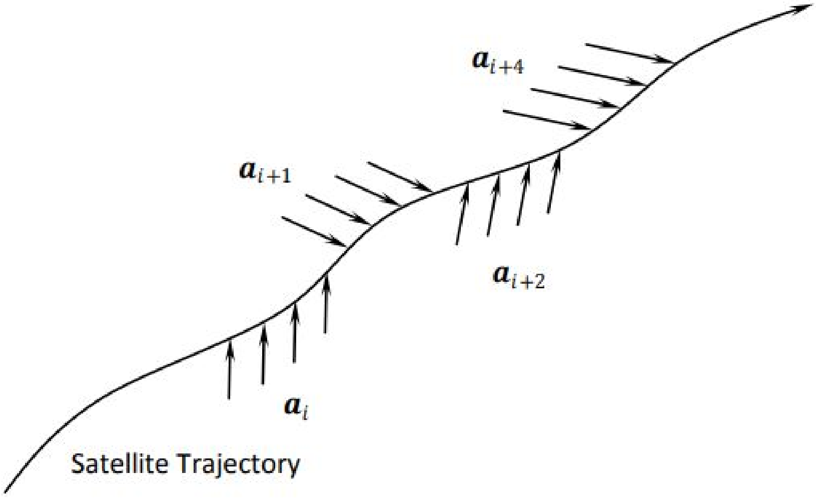

Figure 2.2: Concept of parametrization with pseudo-stochastic PCAs at predefined epochs $i, .., i+n$.

PCAs can compensate for the dynamical deficiencies more continuously at discrete epochs than the pulses and the resulting spacecraft velocities are continuous over an entire orbital arc. In fact, when constrained appropriately, PCAs can mimic the non-gravitational acceleration. In Figure 2.3, it can be seen that the estimated PCAs in the along-track direction closely follow the time-series of acceleration data measured in the same direction.

Pseudo-stochastic parameters (pulses and PCAs) have been used efficiently to replace the dynamic models for non-gravitational forces, in context of gravity recovery. However, the velocity-level discontinuities due to pulses leads to a poor gravity recovery as compared to that of PCAs. In Figure 2.4, it can be seen that the differences in degree amplitudes are larger for pulses as compared to PCAs for Earth's gravity recovery from CHAMP positions.

---

[2] Gravity recovery is highly sensitive to velocity errors.

[3] In reality, the pulses are constrained to an expected ΔV induced by the maneuvers. Furthermore, depending on how many time maneuvers occurs per orbit, the user chooses the interval of estimation of pulses.

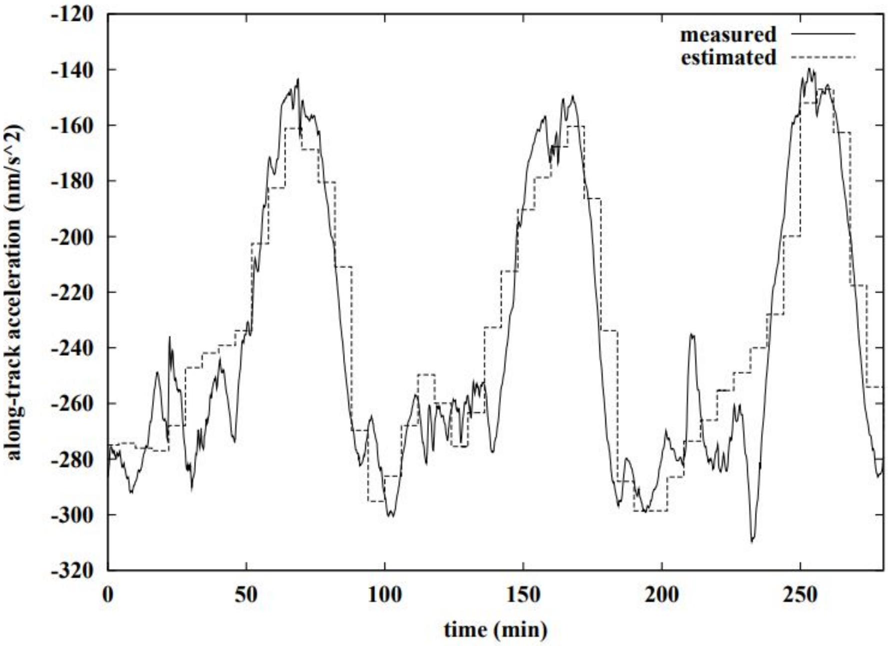

Figure 2.3: PCAs estimated every six minutes compared in along-track direction with accelerometer data from CHAMP [9].

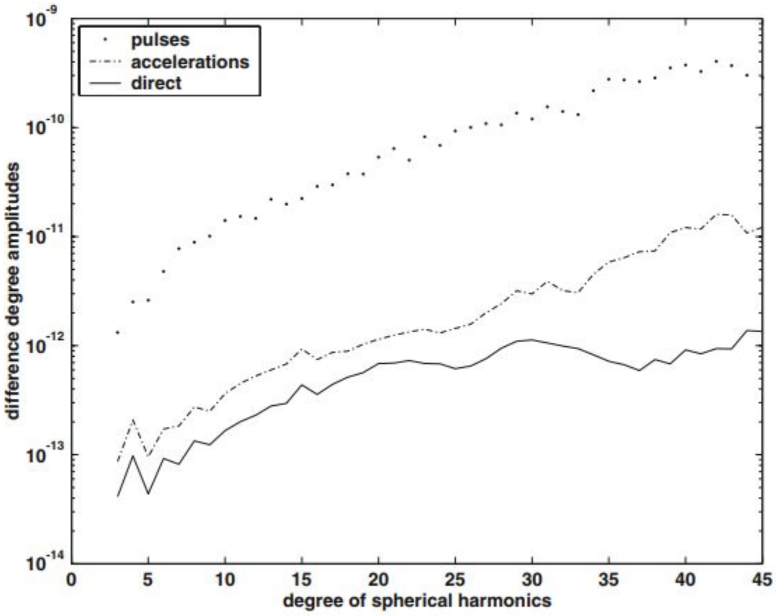

Figure 2.4: Earth's Gravity recovery from CHAMP positions comparison for PCAs and pulses estimated for 30 s [9].

2.4. 2-Way Doppler Modeling

Communications between Earth and spacecraft are made by DSN network over internationally allocated frequency bands (see Table 2.1).

Band	Uplink Frequency (MHz)	Downlink Frequency (MHz)
S	2110-2120	2290-2300
X	7145-7190	8400-8450
Ka	34,200-24,700	31,800-32,300

Table 2.1: Internationally allocated up-link and down-link frequency bands for deep-space communications [2].

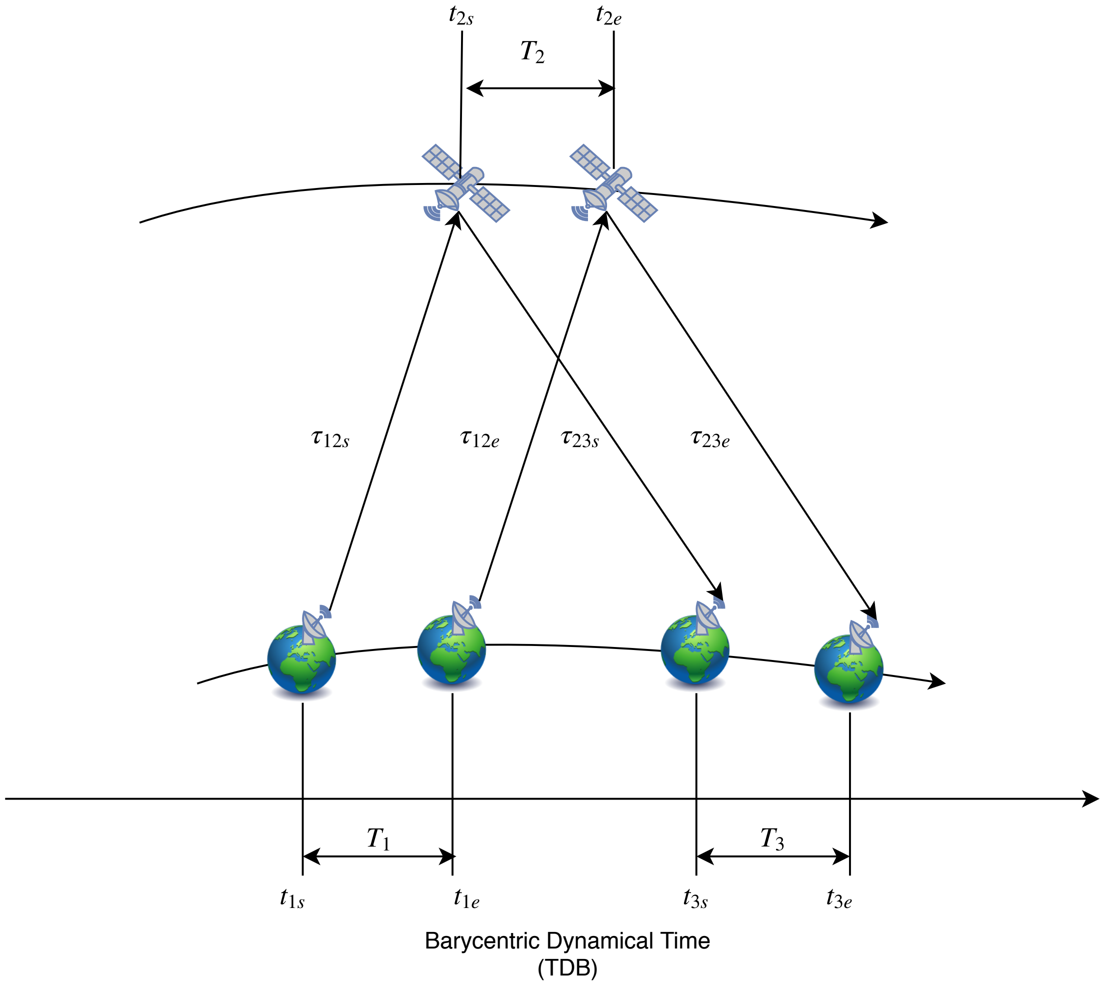

Figure 2.5: Doppler signal transmission and reception in Barycentric Dynamical Time (TDB).

Spacecraft range is measured by the round-trip transit time of a ranging signal that is generated by one of the DSN stations. The signal received by the tracking station will have a frequency that is slightly different from the original value during transmission due to the relative LOS motion between spacecraft and the station. This change in frequency of the tracking signal is known as the Doppler shift, and is recorded by the tracking stations to generate observation data.

Referring to Figure 2.5, a DSN station starts to emit signal at t_{1s} for a specific duration T_1. The transmitted signal is received by the spacecraft and is modulated by the HGA and transmitted back to Earth over a duration T_2 and is received by the station over a duration T_3. This fixed duration (T), over which tracking signals are collected by DSN or spacecraft is known as integration time[4]. The Doppler observable received by the DSN station over integration time T_3 can be related as a function of difference in light-time of the first signal and the last signal received by the DSN station and is given by eq. (2.5) [35]

$$F_{23} = \frac{M f_T}{T_3}\,(\tau_{23e} - \tau_{23s}), \tag{2.5}$$

where,
M → the turn-around ratio applied by the spacecraft on signal frequency (or modulation ratio); for two-way X-band the ratio is 880/749 [35],
f_T → the reference frequency at the DSN station at a given transmission epoch,
T_3 → the integration time,
τ_{23s}, τ_{23e} → the one-way signal time of the first and the last signal respectively, received at DSN station.

Conceptually speaking, one can see that the computed value of observable, F_{23}, is estimated from computing the difference of one-way trip signal time of first and last signal, received by the station. However, precise estimation of signal light-time requires an accurate knowledge of distance between spacecraft and the tracking station in a common reference frame. This distance can be computed from the knowledge of the geocentric position of DSN station (from Earth's center), geocentric location of spacecraft (from planet's center), and the geocentric distance between Earth and the planet (see Figure 2.6). The planetary and station state vector is known (i.e. positions and velocities are known parameters), while the spacecraft's state with respect to the center of the planet is unknown and is estimated by LSQ estimator. Thus, we now know the dependency of computed observations with the spacecraft's states (in particular, its position and velocity). To know more on the mathematical framework to compute light-time values from position and velocity vectors, the reader is directed to Section 12.4.1 of [35].

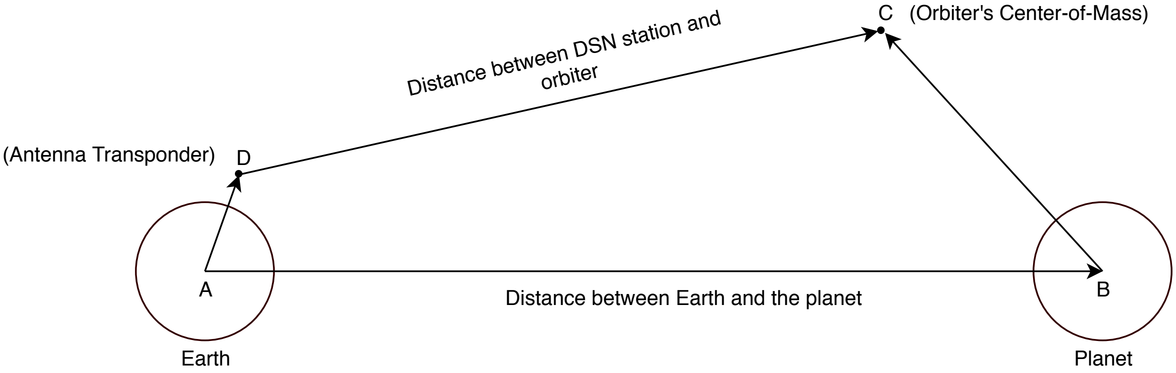

Figure 2.6: Illustration of the distances between Earth and planet, and spacecraft and DSN station. **AD** is the geocentric distance of antenna transponder from the center of Earth, **DC** is the distance between transponder and spacecraft's Center-of-Mass (CoM), **BC** is the position of spacecraft's CoM from planet's center and **AB** is the distance between the centers of Earth and the planet respectively.

2.5. Reference Frames

A reference frame is given by an ordered set of three mutually orthogonal and time dependent unit vectors that define the sense of direction. It is usually complimented by a coordinate system that specifies the logic to locate a point in the reference frame. In order to use (or generate) states, like position and velocity, or orientation data, it is important to understand the choice of reference frame and the coordinate system being used [36].

---

[4] Integration time is also defined as the time between the first signal reception (or transmission), t_s, and the last signal reception (or transmission), t_e

Inertial Frame

An inertial frame is a non-rotating frame with respect to stars and has a non-accelerating origin. The states of spacecraft and astronomical bodies are often expressed in inertial reference frame.

One commonly used inertial frame is the J2000 frame that is defined with the Earth's Mean Equator and Equinox on 1 January 2000 at 12:00 Terrestrial Time (TT). The X-axis is aligned with the Vernal equinox, while Y-axis is oriented with the Earth's spin axis (or the Celestial North Pole) and Y-axis completes the right-hand coordinate system [36]. In reality, J2000 is not purely an inertial reference frame. However the equinox and plane of the equator move very slowly over time that can allow us to treat J2000 as quasi-inertial frame [37]. The equations of motion are integrated in J2000 reference frame. For planet other than Earth, J2000 frame is translated to the origin of that planet (also known as True-of Date reference frame).

Body-fixed Frame

A body-fixed frame shares the same origin with that of inertial. However, the X-Y plane rotates along with the planet, with Z-axis coinciding with its rotational axis. A body-fixed reference frame is commonly used to model aerodynamic forces where densities at spacecraft altitude are estimated based on its latitudinal and longitudinal location over the planet.

Spacecraft Frame

The spacecraft reference frame is specified by three mutually orthogonal axes, each along spacecraft's roll, pitch and yaw axis. Generally, the roll axis passes through the HGA, the pitch axis passes through solar panels and is orthogonal to the roll axis, while the yaw axis completes the right-hand system. The origin of spacecraft reference frame is located at the center of mass of the spacecraft. Its commonly used to express the instrument positions on spacecraft body.

2.6. Orbit Determination Problem

It has been mentioned in Section 2.1 that the first step of orbit determination is integration of the equations of motion from initial conditions at a reference epoch to some later time, which is then followed by using a system of equations that relate the observed parameters (or measured data) with spacecraft's state vector (in particular, position and velocity) to predict the computed values of the observations. Since, the number of equations is greater than number of unknowns (or the parameters to be estimated) for orbit determination problem, LSQ algorithm is used for orbit improvement and for estimation of unknown parameters, where the initial conditions are also adjusted to minimize the squares of the differences (or errors) between observed and computed values of observation. So how is this practically done?

In order to have a conceptual understanding, let us assume that each observation may be expressed as a function of parameters $\mathbf{X}$ of the mathematical models used in orbit determination [26]. Based on modeled function $\mathbf{F}$, the system of observation equations can be represented along with observation errors as [26], [30]

$$\mathbf{L}^{'} + \epsilon = \mathbf{F}(\mathbf{X}), \tag{2.6}$$

where
$\mathbf{F}(\mathbf{X})$ is a non-linear function of parameters $\mathbf{X}$ that can be represented as a linearized function

$$\mathbf{L}^{'} + \epsilon = \mathbf{F}(\mathbf{X_0}) + \mathbf{Ax}, \tag{2.7}$$

with column arrays
$\mathbf{L}^{'}$ → the real observation values,
ϵ → the observational errors (residuals),
$\mathbf{X_0}$ → the initial values (apriori) of the model parameters,
$\mathbf{x}$ → the model parameter corrections with respect to $\mathbf{X_0}$, and
$\mathbf{A}$ → the Jacobi matrix (or the first design matrix).

The first design matrix is defined as

$$\mathbf{A} = \left.\frac{\partial \mathbf{F}(\mathbf{X})}{\partial \mathbf{X}}\right|_{X=X_0}, \tag{2.8}$$

Rearranging eq. (2.7), the system of correction equations can be obtained as

$$\epsilon = \mathbf{Ax} - (\mathbf{L}^{'} - \mathbf{F}(\mathbf{X_0})), \tag{2.9}$$

For least-squares adjustment, the solution of eq. (2.9) is obtained by minimizing

$$\epsilon^{\mathbf{T}}\epsilon. \tag{2.10}$$

Thus, we can see that the least-squares adjustment minimizes the difference (errors or residuals) between observed and the computed values. The spacecraft states are obtained from orbit integration, starting from initial conditions, over a user-specified time frame (or data arc) and are used to analytically compute the observations over the data arc. Since, initial conditions are treated as free (or unknown) parameters, they are adjusted by the LSQ estimator that attempts to minimize the squares of the error as given by eq. (2.10) and the orbit is integrated again with adjusted initial conditions, which can further be subjected to LSQ adjustment until a convergence is reached. Once an orbit parametrization that results in best observation residuals is achieved, the gravity terms (or spherical harmonic coefficients) can also be treated as free parameters to co-estimate the gravity field. Please note that it is possible to co-estimate the gravity field along with the orbits (or positions) right from the beginning. However, as a good practice, it is worthwhile to first obtain best orbit parametrization that gives best orbits and, consequently best observation residuals.

3

Spacecraft Environment Modeling

In Chapter 2, the dynamic orbit model has been introduced to the reader. It is now understood that a spacecraft orbiting a planet is not only under the influence of gravity field of the planet, but its orbit is also perturbed by non-gravitational forces, the behavior of which depends on planetary atmosphere and its proximity to Sun. Considering this, the present chapter presents an overview of the modeling procedure of the environment around Magellan's orbit. Section 3.1 discusses on the Venusian atmosphere and highlights the density model selected to model drag acceleration. Subsequently, analytical framework is provided to model Solar Radiation Pressure (SRP) and Planetary Radiation Pressure (PRP) in Sections 3.2 and 3.3, respectively.

3.1. Atmosphere

Magellan was in a near-circular orbit with periapsis between 160 km to 220 km and apoapsis between 600-350 km during gravity acquisition cycles [6]. As per Taylor et al., (2014), the periapsis lie in thermosphere, whereas the apoapsis is in Exosphere during the entire gravity phase of the mission [38]. Nevertheless, in order to model acceleration due to aerodynamic forces, it is important to have a knowledge of densities at spacecraft altitudes.

Quantitative data pertaining to the Venusian atmosphere have been gathered from Earth-based observations and from missions that have either entered the Venusian atmosphere or have passed within several radii of Venus. Yet, due to lack of in-situ observational data and custom extrapolation within acceptable limits of relevant theories, robust density models for the atmosphere of Venus are lacking till this date, particularly for upper atmosphere (above 100 km from the surface) [39], [40]. An extensive literature study has been done to have a choice of density models for this project. However, given the time-frame and scope of this research, a detailed comparison between different density models, and their impact on orbit solutions, has not been pursued. Nevertheless, the following criteria have been established for selecting appropriate density model:

1. Developed from in-situ observations of multiple missions.
2. Tightly constrained to observation data.
3. Ease of integration into orbit determination software.

Two empirical atmospheric density models for upper atmosphere, namely VTS3 developed by Hedin et al., 1983 and VIRA developed by Keating et al., 1985, were available for this project. However, both the models were benchmarked against the above criteria to select the best model for this project and VIRA model was deemed to be the most suitable density model. To provide a justification, both the models shall be scrutinized.

VTS3 is a semi-empirical model to predict variations in temperature, atmospheric compositions and densities above 100 km as a function of latitude, local solar time and solar-flux. The information of upper atmosphere is mainly constrained by in-situ observations of CO_2, CO, He, O, N, N_2 neutral densities between 142 km to 250 km from Pioneer Venus Orbiter's (PVO) Orbital Neutral Mass Spectrometer (ONMS) [41]. Beyond 250 km, it is assumed that the densities of each specie decreases exponentially with the altitude, which can easily contribute to the errors in modeling of aerodynamic forces. Furthermore, VTS3 was not readily available to be implemented in the orbit determination software due to untimely procurement.

On the other hand, the VIRA model for upper atmosphere considers extensive observations from PVO's ONMS, Bus Neutral Mass Spectrometer (BNMS), Orbiter Ion Neutral Mass Spectrometer (OINMS), Orbiter Ultraviolet Spectrometer (OUVS), Orbiter Infrared Radiometer (OIR), Orbiter Atmospheric Drag (OAD), Venera 9-12 and Mariner 4, 5 and 10. The construction of VIRA for altitudes 100-250 km is substantially different from that of VTS3. Contrary to the exponential decay assumption by Hedin et al., 1983, the upper atmosphere for VIRA model is divided into two regions: 100-150 km and 150-250 km [19]. The atmospheric densities in the regions between 100-150 km are constrained by observations from BNMS, ONMS and OAD and are modeled as a function of height and Local Solar Time (LST) (see Figure 3.1). The densities for regions between 150-250 km are based on the OAD and ONMS observation; and are dependent on height and Solar Zenith Angle (SZA) (see Figure 3.5) [41][1]. VIRA atmosphere model is available in stand-alone FORTRAN package known as Venus-GRAM, developed by Marshal Spaceflight Center, NASA [42][2]. Thus, based on the benchmark against the above discussed criteria, VIRA model was selected for this project.

While a detailed study on Venusian atmosphere is beyond the scope of this project, a short discussion on the variation in atmospheric properties may still be appropriate to understand the physical structure of the Venusian atmosphere. It can be seen from Figures 3.1 and 3.5 that the densities decay exponentially with increase in altitude. This behavior can be approximated by an exponential density model given as

$$\rho = \rho_0 e^{-h/H_0}, \tag{3.1}$$

where

ρ_0 → the atmospheric density given at a reference height $[kg/m^3]$,

H_0 → the increase in altitude where the atmospheric density reduces by a factor of e $[km]$, also known as scale height. In case of Venus, the scale height from the surface is 15.9 km [43].

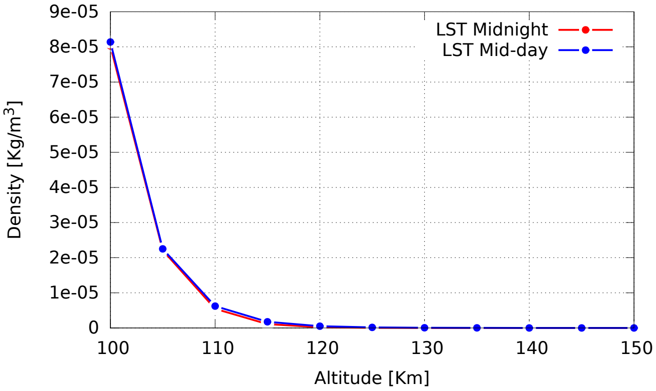

Figure 3.1: VIRA atmospheric densities given for two Local Solar Times (LST) between 100-150 Km altitude. There are no significant diurnal changes in the atmospheric densities.

The atmospheric scale height can be conveniently represented by the following equation

$$H_0 = \frac{RT}{\mu g}, \tag{3.2}$$

---

[1] SZA is defined as the angle between the zenith and the centre of the Sun's disc

[2] Venus-GRAM: Venus Global Reference Atmosphere Model is a software package for implementing Venusian atmosphere model. The atmospheric properties from surface to 250 km is based on VIRA model. For altitudes beyond 250 km, an empirical model that assumes a constant exospheric temperature (specified at 250 km by VIRA) developed by MSFC is used [42].

where
$R \rightarrow$ the universal gas constant $[J/(mol-K)]$,
$T \rightarrow$ mean atmospheric temperature $[K]$,
$\mu \rightarrow$ the molecular weight of one gas particle $[kg/mol]$,
$g \rightarrow$ acceleration due to gravity $[m/s^2]$.

The thermosphere region is mainly characterized by increase in atmospheric temperature with altitude, and large dichotomy between diurnal temperatures that is mainly driven by solar ultraviolet radiation (this dichotomy can be clearly seen in Figure 3.2). However, this difference in temperatures has no substantial effect on the densities for extreme LSTs and this is evident in Figure 3.1. The main source of thermal energy in thermosphere region is the dissociation of atmospheric species. As per Schubert, 1983, the dissociation of CO_2 leads to abundance of CO and O, this can be seen in Figure 3.4 for altitudes between 100-130 km. Furthermore, it can be seen from Figure 3.3 that there is no significant diurnal change in abundance of $CO2$ and N_2 molecules which confirms the dominance of greenhouse gases in Venusian atmosphere [44].

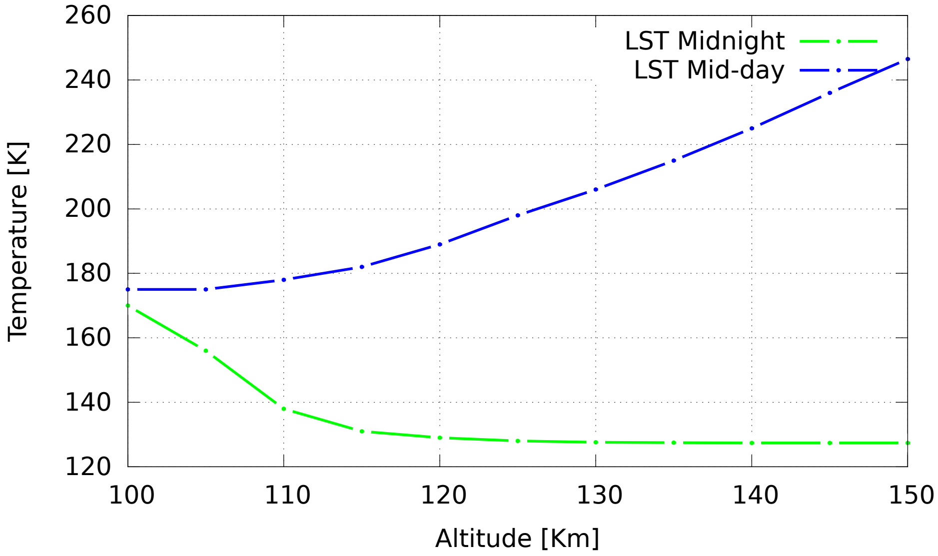

Figure 3.2: VIRA atmospheric temperature profile for altitudes between 100-150 km at two Local Solar Times (LST). A large temperature differences, observed at midnight and mid-day respectively, is driven by solar ultraviolet radiation.

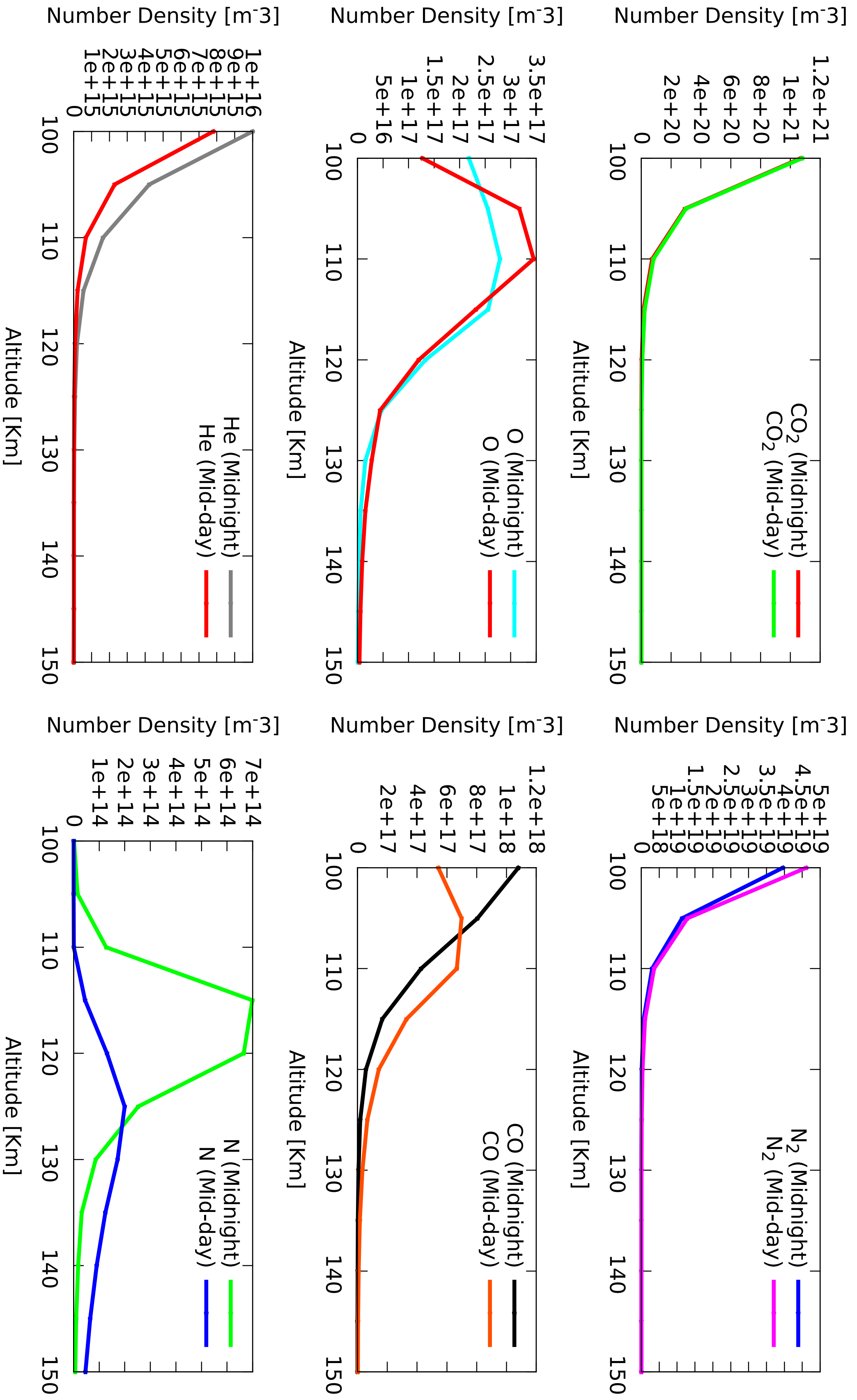

Figure 3.3: Number densities for atmospheric species shown at two Local Solar Times (LST) for altitudes between 100-150 km, given by VIRA. Compared with night-side, the dissociation of CO_2 into CO and O on the day-side of Venus can be characterized by increase in number densities of O and CO constituents at altitudes between 100-130 km.

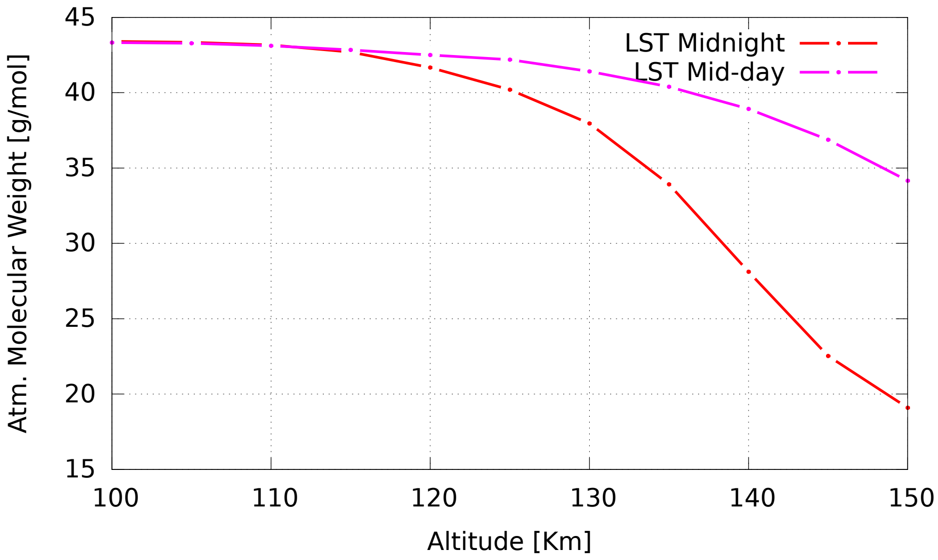

Figure 3.4: Molecular weight of atmospheric gases at two Local Solar Time (LST) for altitudes between 100-150 Km , given by VIRA. The difference in molecular weight between day-side and night-side become more evident starting from an altitude of approximately 115 Km.

The properties of atmosphere and its constituents become increasingly dependent on SZA for altitudes between 150-250 km. In other words, the diurnal variations are larger in this region as compared to the region between 100-150 km. From Figure 3.5, it can be seen that atmospheric densities are also functions of SZA in addition to the altitude. As SZA increases, the atmosphere densities reduce. However, the decrease in the densities with increase in SZA can be attributed to the mitigation of solar radiation with increase in SZA, leading to reduction in dissociation activity on the night-side of Venusian atmosphere. This can also be characterized by the decreasing number densities of each atmosphere species and the atmospheric molecular weight given in Figures 3.8 and 3.9 respectively for increasing SZA.

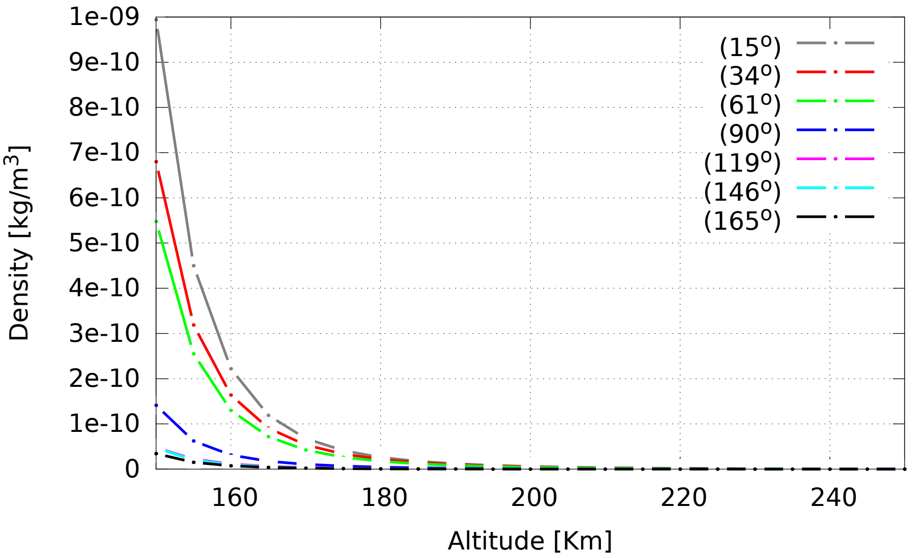

Figure 3.5: VIRA atmospheric densities for different values of SZA, for altitudes between 150-250 km. The densities decrease with increase in SZA.

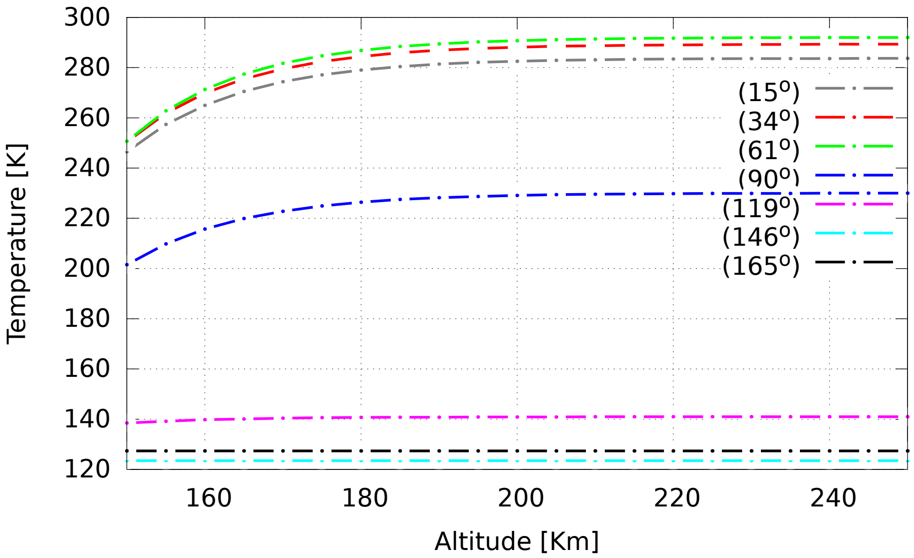

Figure 3.6: VIRA atmospheric temperature profile for different values of SZA, for altitudes between 150-250 km. The ambient temperature reduce with increase in SZA.

The diurnal variations in ambient temperature are observed in Figures 3.2 and 3.6 respectively. This indicates that the atmospheric properties of upper atmosphere are mainly dependent on SZA, i.e. they become even more sensitive to SZA above 150 km.

Another interesting fact to be mentioned is that Venus experiences no substantial seasonal variation because it's obliquity to ecliptic is approximately 177.4 degrees (retro-grade rotation). As a result similar variations in the atmospheric properties are observed in the northern and southern hemisphere, and are symmetric around equator throughout the Venusian year (see Figure 3.7).

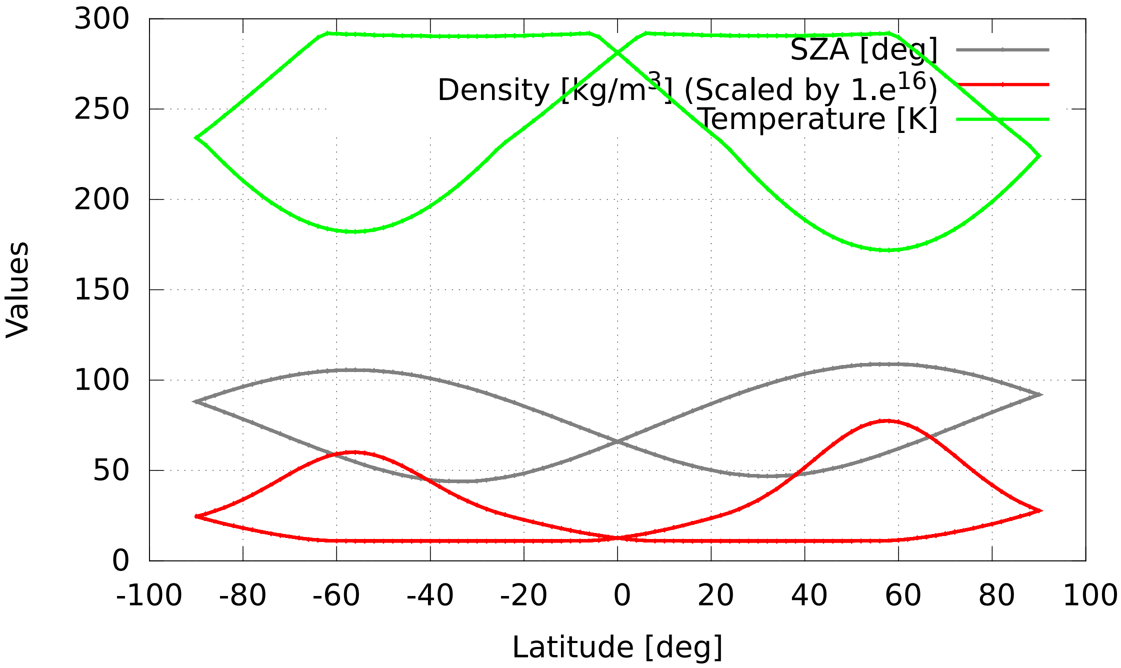

Figure 3.7: Variation in SZA, atmospheric densities and temperatures expressed as functions of latitudes at 400 km, shown for Day 122 of 1994. The atmospheric properties show similar trend for both the hemispheres, indicating an absence of seasonal variations in atmosphere of Venus.

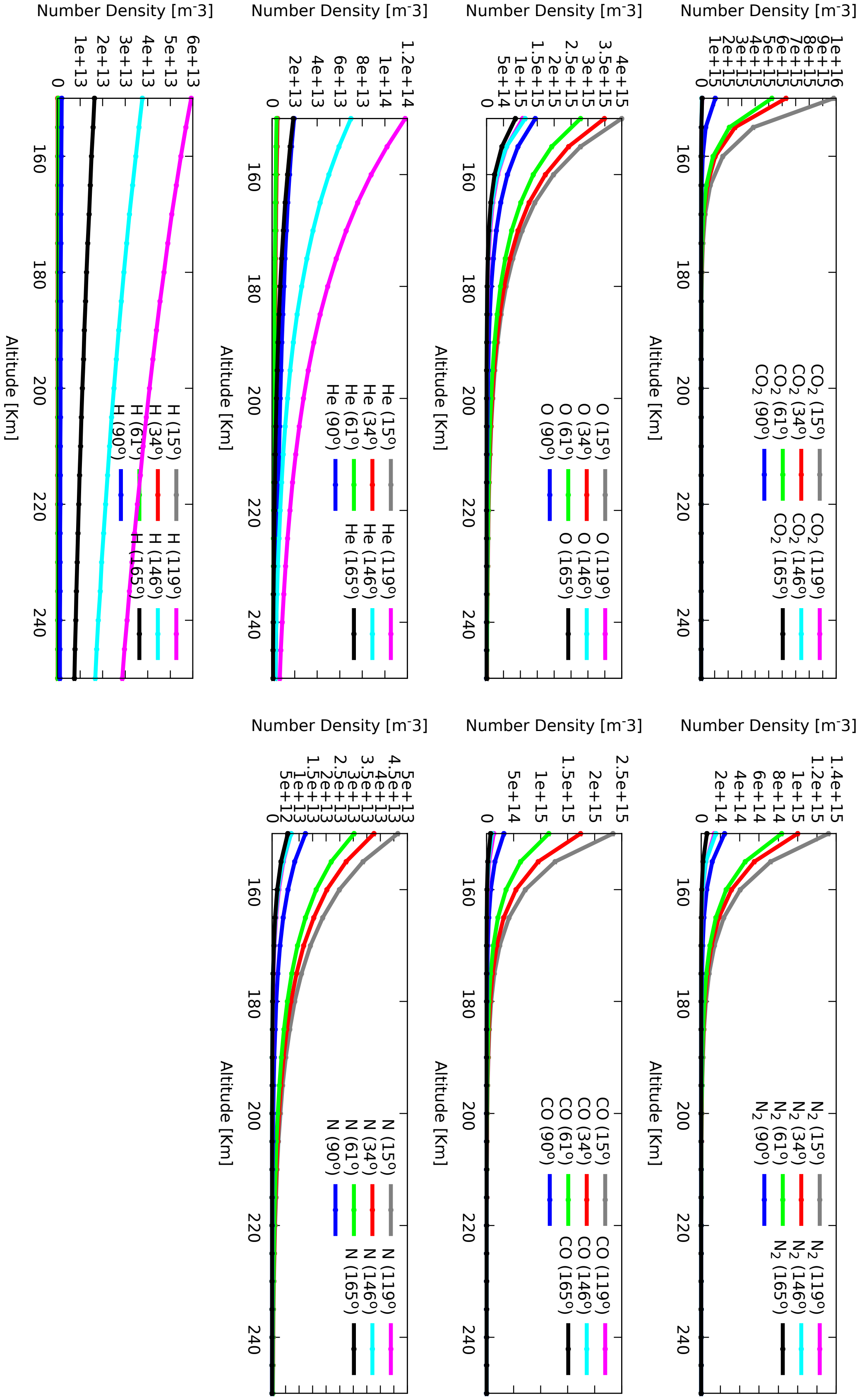

Figure 3.8: Number densities for atmospheric species shown at different values of SZA for altitudes between 150-250 km, given by VIRA.

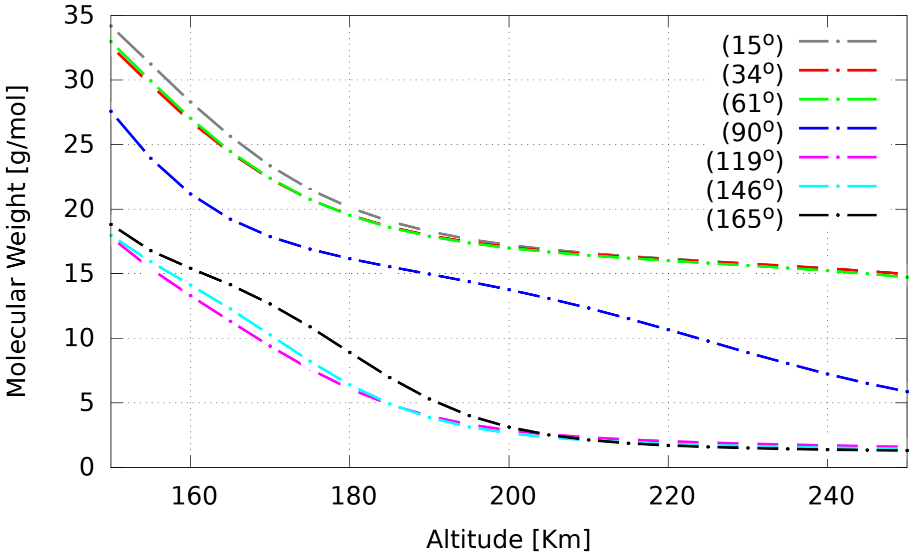

Figure 3.9: Molecular weight of atmospheric gas for different SZA angles for altitudes between 150-250 km , given by VIRA

Once the atmospheric densities are known, the acceleration due to drag force can be modeled as

$$\ddot{\mathbf{r}}_{Drag} = \frac{1}{2}\frac{A}{m}\rho_\infty V_{atm}^2 C_D \hat{\mathbf{u}}, \tag{3.3}$$

where
C_D → spacecraft drag coefficient [-],
A → spacecraft area $[m^2]$,
m → spacecraft mass $[kg]$,
ρ_∞ → free stream atmospheric density $[kg/m^3]$,
V_{atm} → Spacecraft velocity with respect to the atmosphere $[m/s]$,
$\hat{\mathbf{u}}$ → unit vector of incoming particles.

The drag coefficient, C_D, can be modeled analytically or kept fixed. For this project, the analytical modeling of drag coefficient is not pursued and is rather fixed apriori value which can be empirically estimated during each LSQ iteration.

3.2. Solar Radiation Pressure

It has been seen in Section 3.1 that a change in SZA can have effect on the Venusian atmosphere. However, apart from manipulating atmospheric properties, solar radiation can have secular effect on a spacecraft's orbit. Given the close proximity of Venus to Sun, it is important to account for the acceleration experienced by Magellan due to incident solar radiation.

For a simple spherical spacecraft with uniform optical properties, the acceleration due to solar radiation pressure, assuming that the spacecraft is in constant sunlight, can be modeled by the eq. (3.4).

$$\ddot{\mathbf{r}}_{SRP} = C_R \frac{A}{m} P_\odot \hat{\mathbf{r}}_\odot \tag{3.4}$$

where,
C_R → spacecraft radiation coefficient (also modeled as $C_R = 1 + \frac{4}{9}\delta$, where δ is diffusion coefficient [45]) [-],
A → area of the spacecraft illuminated by Sun $[m^2]$,
m → spacecraft mass $[kg]$,
$P_\odot$ → mean solar radiation pressure at spacecraft's position $[N/m^2]$,

$\hat{\mathbf{r}}_{\odot}$ → Sun-to-spacecraft unit vector.

The mean solar radiation pressure at 1 AU is given as

$$P_{\odot 1AU} = \frac{\Phi_{\odot 1AU}}{c}, \tag{3.5}$$

where
$\Phi_{\odot 1AU}$ → the mean solar flux which is approximately equal to 1370 W/m^2,
c → speed of light approximated as $3 \times 10^8\ m/s$.

Thus, $P_{\odot 1AU}$ is approximately $4.56 \times 10^{-6}\ N/m^2$. However, it is important to note that the mean solar flux, $\Phi_{\odot 1AU}$, is not always constant and varies roughly by ±3.3% over a period of 1 Earth year due to Earth's eccentricity roughly ±0.1% over one solar cycle. Nevertheless, it is possible to extrapolate the value of known mean solar radiation pressure, $P_{\odot 1AU}$, at spacecraft distance for a planetary orbiter and is given as

$$P_{\odot} = \left(\frac{1\ AU}{r_{\odot}}\right)^2 P_{\odot 1AU}, \tag{3.6}$$

where
$r_{\odot}$ → the varying distance of spacecraft's Center-of-Mass (CoM) from Sun's center $[m]$.

While eq. (3.4) is the simplest form to express acceleration on the spacecraft due to SRP, its physical significance shall be understood before adding more details to account for additional physical phenomena like eclipse. From eq. (3.4), we can see that the acceleration due to solar radiation pressure is directed away from Sun, and depends on spacecraft's physical and optical properties. For a perfectly reflecting spacecraft body, i.e. $C_R = 1$, the acceleration due to direct radiation pressure will be maximum assuming that the mass and area are fixed.

Eq. (3.4) is valid only when the spacecraft is in sunlight. For real conditions, this is not always true and the spacecraft experiences eclipse conditions too[3]. In order to model the eclipse, a shadow function, f, is introduced in eq. (3.4) and the acceleration due to SRP can be reformulated as [46]

$$\ddot{\mathbf{r}}_{SRP} = C_R \frac{A}{m} P_{\odot} f \hat{\mathbf{r}}_{\odot}, \tag{3.7}$$

where,
$f = 0$ for full eclipse, when the spacecraft is in umbra,
$0 < f < 1$ for partial eclipse, when the spacecraft is in penumbra,
$f = 1$ when spacecraft is in full sunlight.

The shadow function, f, contains the geometric shadowing of the fractional part of Sun by the planet and the fractional part of sunlight that is not absorbed by the atmosphere. Thus, f can be expressed as the product of these effects and can be represented as

$$f = f_g f_a, \tag{3.8}$$

where, f_g is the geometric shadowing factor and f_a is the atmospheric reflection factor.

The geometric shadowing function, f_g, can be derived by considering the geometry between planet, spacecraft and Sun. While a full mathematical treatment is not presented here, one can refer to the work done by Montenbruck et al., [2000] for complete derivation [47]. The final equation relevant for the implementation of eclipse is given as

$$f_g = 1 - \frac{1}{\pi}\arccos(\eta) + \frac{\eta}{\pi}\sqrt{1-\eta^2}, \tag{3.9}$$

---

[3] Assuming a polar orbit, the eclipse condition depend on the angle between Sun and the orbital plane, also commonly known as β-angle. When this angle is 90 degrees, the spacecraft is always in the sunlight, hence no eclipse.

where η is a geometric parameter defined as:

$$\eta = \frac{h_c}{h_c - h_b}, \tag{3.10}$$

where,
h_c → apparent height of center beam of the solar disc from planet's surface,
h_b → apparent height of bottom beam of the solar disc from planet's surface.

From eq. (3.10) the following conditions can be observed:

$\eta < -1$ when spacecraft is in total eclipse,
$-1 < \eta \leq 1$ when spacecraft is in partial eclipse,
$\eta > 1$ when spacecraft is in full sunlight.

Considering large uncertainties in upper atmosphere model, the atmospheric reflection and refraction to model f_a shall not be pursued for this research and it will be fixed to unity.

3.3. Planetary Radiation Pressure

Venus is the third brightest object in the sky after Sun and Moon. Its close proximity to Sun can subject it to intense solar irradiation of about 2601.3 W/m^2, which is roughly twice the amount of flux received by Earth. However, higher solar radiance is not the only reason why Venus is so bright. The planet has a dense atmosphere and is blanketed by highly reflective clouds made of sulphuric acid crystals, with effective crystal radius of 0.6-1.5 μm, that are suspended in mixture of gases [48], [49]. As a result light can easily bounce off these crystals, which is the reason why Venus is so bright. In quantitative terms, the brightness of an astronomical body is given by the ratio of diffuse reflection of solar radiation and the total solar radiation received by the body, called Albedo. While Earth has an albedo of around 0.33, Venus has an albedo of approximately 0.76, thereby making it the brightest planet in our solar system. In other words, 76% of the total solar radiation is reflected back into the space diffusively, that will hit the spacecraft and can disturb the nominal orbit. In addition to reflected radiation pressure, a spacecraft orbiting around Venus will experience a near-constant emitted radiation in the infrared wavelengths due to the planet's powerful greenhouse effect. As a result, modeling planetary radiation pressure to account for the perturbing accelerations due to reflectivity and emissivity of Venus is critical for a spacecraft orbiting the Venusian surroundings.

Analogous to the acceleration due to SRP, the accelerations on the spacecraft due to Reflected Planetary Radiation Pressure (R-PRP) and Emitted Planetary Radiation Pressure (E-PRP) are directly proportional to the exposed area of the spacecraft and inversely proportional to its mass.

For the sake of easy understanding, let us assume a simple case of a spherical spacecraft that is orbiting a spherical planet, of radius R, with uniform irradiance. In this case, the acceleration of the spacecraft due to R-PRP can be given by

$$\ddot{\mathbf{r}}_{R-PRP} = C_R \frac{A}{m} P_{R-PRP} \hat{\mathbf{r}}_{\oplus}, \tag{3.11}$$

where
C_R → spacecraft radiation coefficient (also modeled as $C_R = 1 + \frac{4}{9}\delta$, where δ is diffusion coefficient [45]) [-],
A → exposed area of the spacecraft [m^2],
m → satellite mass [kg],
P_{R-PRP} → reflected radiation pressure from the source [N/m^2],
$\hat{\mathbf{r}}_{\oplus}$ →unit vector of spacecraft's CoM distance from the source [m].

Similarly, the acceleration on the spacecraft due to E-PRP is given as:

$$\ddot{\mathbf{r}}_{E-PRP} = C_R \frac{A}{m} P_{R-ERP} \hat{\mathbf{r}}_{\oplus}, \tag{3.12}$$

where
P_{E-PRP} → emitted radiation pressure from the source $[N/m^2]$.
The reflected radiation pressure, (P_{R-PRP}), experienced by the spacecraft due to a planetary surface under constant sunlight is given as:

$$P_{R-PRP} = \frac{1\ AU}{|D_{\odot} - R_{\oplus}|^2} P_{\odot 1AU} \frac{A_{\oplus}\alpha}{(\pi|\mathbf{r}|)^2}, \tag{3.13}$$

where
$D_{\odot}$ → planetary distance from the Sun $[m]$,
$\mathbf{r}$ → spacecraft's position from center of the planet expressed in inertial reference frame $[m]$,
α → planetary albedo,
$A_{\oplus}$ illuminated planetary area $[m^2]$.

Similarly, emitted planetary radiation pressure at spacecraft location can be given as

$$P_{E-PRP} = \frac{1\ AU}{|D_{\odot} - R_{\oplus}|^2} P_{\odot 1AU} \frac{A_{\oplus}\epsilon^{'}}{4\pi(|\mathbf{r}|)^2}, \tag{3.14}$$

where
$\epsilon^{'}$ → planetary emissivity (can be represented as $1-\alpha$).

However, eqs. (3.13) and (3.14) are valid when the planet is treated as a single light source and the spacecraft is at large distance from the planetary surface ($|\mathbf{r}| >> R_{\oplus}$, where $R_{\oplus}$ is planetary radius). Given the close proximity of the spacecraft to the surface of the planet, it is possible that each part of the planetary surface will contribute with different acceleration magnitude, depending on the location of spacecraft. As a result, the planetary radiation pressure accelerations are calculated by summation of the accelerations due to discretized surface elements with latitudinal and longitudinal dimensions. This method is based on the model proposed by Knocke et al, [1988] that divides a part of the planet's surface, that can be seen by the spacecraft, into discrete elements [50]. Furthermore, each element is approximated with a plane surface that forms tangent to the center of the element [50]. The acceleration experienced by the spacecraft due to planet's albedo and infrared radiation from each element is calculated by using Lambert's Law of diffusion [50].

For a theoretical understanding, let us divide the planetary surface into L longitudinal elements and M latitudinal elements. Then each element on the planetary surface, will be of measurement $\Delta\lambda \times \Delta\phi$ degrees, where the longitudinal elements, $\Delta\lambda$, and latitudinal elements, $\Delta\phi$, are given as

$$\Delta\lambda = \frac{360^o}{L}, \tag{3.15}$$

and

$$\Delta\phi = \frac{180^o}{M}. \tag{3.16}$$

Now that the planetary surface is divided globally into discrete grids, the accelerations due to planetary radiation pressures will depend on two additional factors: 1) whether the element is illuminated by the sunlight, 2) whether the element is visible to the spacecraft. The angle to check solar illumination on an element can be known by taking the dot product of element-Sun unit vector, $\hat{\mathbf{r}}_{ELE\odot}$, and the surface-normal unit vector, $\hat{\mathbf{n}}_{ELE}$:

$$\psi = \hat{\mathbf{r}}_{ELE\odot}.\hat{\mathbf{n}}_{ELE}. \tag{3.17}$$

Similarly, to know the spacecraft visibility with respect to the element, the angle between spacecraft-element unit vector, $\hat{\mathbf{r}}_{ELE}$, and the unit vector normal to the element surface, $\hat{\mathbf{n}}$, can be estimated by

$$\beta = \hat{\mathbf{r}}_{ELE}.\hat{\mathbf{n}}, \tag{3.18}$$

Thus, the planetary radiation pressures can be modified for each discrete element, i, with a condition for solar illumination and spacecraft visibility. They are given as follows:

$$P_{R-PRP,i} = \begin{cases} 0, & \text{if } \psi_i \leq 0\ or\ \beta_i \leq 0. \\ \left(\frac{1\ AU}{|\mathbf{r}_{ELE\odot,i}|}\right)^2 P_{1AU} \frac{A_i\alpha_i}{|\pi\mathbf{r}_{ELE,i}|^2}\phi_i\beta_i, & \text{if } \phi_i > 0\ and\ \beta_i > 0 \end{cases} \tag{3.19}$$

$$P_{E-PRP,i} = \begin{cases} 0, & \text{if } \psi_i \leq 0 \; or \; \beta_i \leq 0. \\ \left(\frac{1\ AU}{|\mathbf{r}_{ELE\odot,i}|}\right)^2 P_{1AU} \frac{A_i \epsilon_i}{4\pi |\mathbf{r}_{ELE,i}|^2} \phi_i \beta_i, & \text{if } \phi_i > 0 \; and \; \beta_i > 0 \end{cases} \tag{3.20}$$

The total accelerations due to planetary radiation pressures for i surface elements can be given as

$$\ddot{\mathbf{r}}_{R-PRP} = \sum_{i=1}^{M} C_R \frac{A}{m} P_{R-PRP,i} \hat{\mathbf{r}}_{ELE,i}, \tag{3.21}$$

and

$$\ddot{\mathbf{r}}_{E-PRP} = \sum_{i=1}^{M} C_R \frac{A}{m} P_{E-PRP,i} \hat{\mathbf{r}}_{ELE,i}. \tag{3.22}$$

From eqs. (3.21), (3.19) and (3.22), (3.20), it can be seen that the modeling of PRP considers only that part of the planetary surface which is visible to the spacecraft and is illuminated by Sun. However, the accuracy of estimated accelerations due to PRP depends on the resolution of the surface grids. On the other hand, higher resolution requires a longer compute time. For this project, the planetary surface is divided into grids of resolution 1^o for the best quality.

4

Implementation

Previous chapters introduced the reader to the theoretical backbone of this project. In this Chapter, the relevant software and computational tools used for orbit determination are discussed in Section 4.1. Subsequently, preparation of Doppler observations and preprocessing is discussed in Section 4.2. The geometric models for station coordinates and planetary ephemeris is discussed in Section 4.3. Finally, implementation of spacecraft macro-model and mathematical formulation of the attitude assumptions is presented in Section 4.4

4.1. Software & Computational Tools

4.1.1. Bernese GNSS v5.3

The Bernese GNSS Software is a scientific software package for geodesy and LEO precise orbit determination applications, and is developed and maintained by the Astronomical Institute University of Bern, Switzerland (AIUB)[1]. The high performance and high accuracy software encapsulates state-of-the-art dynamic and kinematic orbit modeling techniques and offers detailed control over observation processing and powerful tools for automation for orbit determination. The typical users of the software are:

- Scientists working in research institutions and academia.
- Agencies that are responsible for the maintenance of permanent GNSS receivers.
- Commercial users working in the domain of precise orbit determination.
- Cartography and land survey agencies that asses the accuracy of GNSS.

The above list of users is not exhaustive and also includes several institutions and universities world wide that are working with large observation data generated by GPS, SLR and GLONASS. The modular design of the software gives it the flexibility to tailor the routines based on the user requirement and allows the users to test their own implementations for Earth-based missions (e.g. non-gravitational force models, troposphere and ionosphere models).

Recently, AIUB has extended geodesy studies to other astronomical bodies in the Solar System. For this purpose, a development version of Bernese GNSS Software (V5.3) has been extensively used to process DSN tracking data to extract gravity field information of the body under investigation [2].

In a nutshell, a typical process flow followed by Bernese GNSS Software V5.3 user is given in Figure 4.1

---

[1] The recent stable release of *Bernese GNSS* is V5.2 and V5.3 is still in continuous development phase, and is commercially unavailable.

[2] The newly-implemented capability to process DSN data was used to obtain Lunar gravity field from primary phase of GRAIL mission (see [51] for more information).

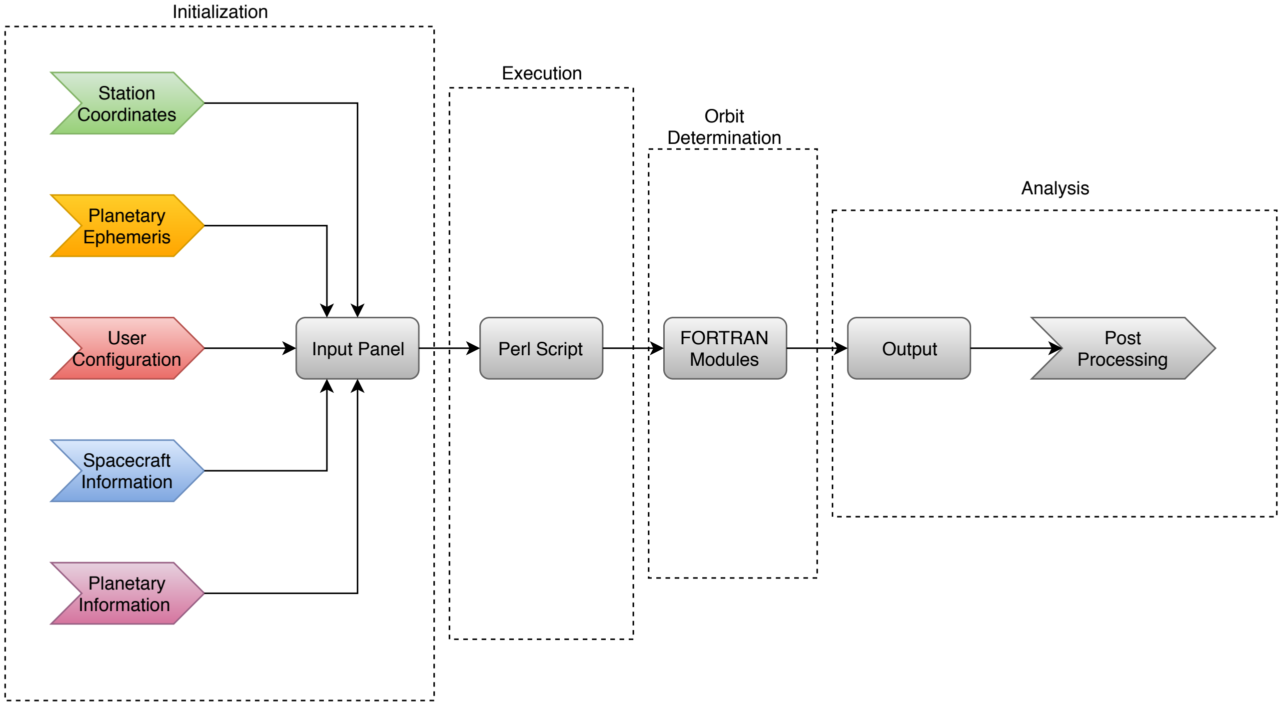

Figure 4.1: The general process flow for using *Bernese GNSS Software*. The User Configuration also includes apriori orbits.

Referring to Figure 4.1, the orbit determination begins at input panel where the user specifies the path of the files containing apriori values for station coordinates, planetary ephemeris, apriori state vectors, observation files, gravitational field and spacecraft specification (e.g.: Spacecraft macro-model). In addition to this, the user specifies the desired configuration for orbit determination (for example, kind of atmosphere model, choice of empirical parameters.). Once the orbit determination scheme has been set up by saving the choice from input panel, the executable FORTRAN modules are launched by a Perl script that also invokes the automated Bernese Processing Engine containing the logical process flow of the software.

The FORTRAN modules are central to Bernese GNSS Software and contain the routines and mathematical models that are required for POD. Each component of orbit modeling has its own modular script. This means that there are separate scripts for non-gravitational forces (SRP, PRP, and Aerodynamic Forces). Thus, by having modular and self-contained scripts, one can test their own implementations of a particular orbit model without affecting other routines. For this project, Bernese GNSS v5.3 is used for Doppler data processing, POD and scientific analysis.

4.1.2. SPICE Toolkit

SPICE toolkit is an information system that was developed to assist the scientists in planning and analyzing scientific observations from space instruments. It is developed and maintained by NAIF that operates under NASA's Planetary Science Division. Beyond scientific investigations, SPICE toolkit is also used by space agencies to model, plan and execute operations that are needed to design planetary exploration missions. For this project, the main purpose of SPICE toolkit (FORTRAN version) is to obtain the state vectors for Magellan mission, estimated by Konopliv et al., [1999], that shall also be used as initial conditions (state vectors or Keplerian elements) to perform POD and to test the implementation of non-gravitational models.

4.1.3. Venus-GRAM

Venus-GRAM is an atmosphere package that provides extensive atmospheric data for Venus at any altitudes from the surface. It is an automated implementation software of empirical Venusian atmosphere model, VIRA, that was developed by Keating et al., [1985] by using in-situ measurements from PVO, Venera 9, 10, 11, 12 and Mariner 4, 5, 10 [19]. Venus-GRAM is developed and maintained by NASA Marshal Spaceflight Center, and is a FORTRAN based tool that can be used in aerodynamic force routine to obtain density estimates at spacecraft altitudes. However, Venus-GRAM cannot be readily integrated into the larger software framework because it is a standalone tool and one has to re-program the main routine (or wrapper) to accept inputs in form of arguments instead of reading from input file. Nevertheless, Venus-GRAM has been successfully implemented in the airdrag routine where the elliptical coordinates of Magellan, epoch in HH:MM:SS UTC format, and day of the year in DD:MM:YYYY format are passed directly to the main wrapper.

4.2. Doppler Processing

The deep space Doppler tracking data for Magellan mission are available publicly at the Planetary Geoscience Node of Washington University, USA[3]. The data files are given in binary custom format called Orbit Data File (ODF). The first step of using Doppler observation is to convert the binary file into Bernese-compatible ASCII file using Bernese GNSS' `ODF2ASCII` tool. The ASCII observation file contains tabulated details of observations and their corresponding epoch, and tracking station (see Figure 4.2). The observation files are created for each day during the entire gravity phase of the mission, i.e. from 3-August-1993 to 30-August-1994.

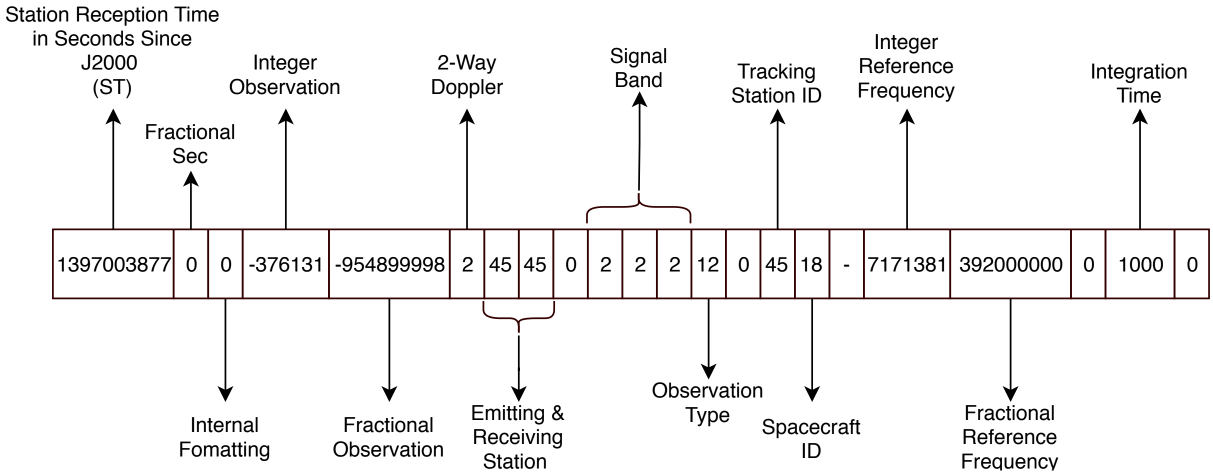

Figure 4.2: An illustration of Bernese-compatible format. The integer part and fractional part of observations are tabulated separately for extended precision. The observation type that corresponds to Magellan mission is 2-way X-band Doppler and the observations are sampled with 10 seconds integration time. Unlabeled zeros indicate internal formatting.

It is important to highlight that the precise time stamps (in ST, which is equal to UTC) of the received signal at the DSN station is used to derive reception time at spacecraft and signal emission time at the tracking station (both in TDB, this requires conversion from ST to TDB) which are then used to determine observed values of the Doppler observations (see Section 2.4 of Chapter 2). The signal emitted at the station can either be ramped or un-ramped[35]. A ramped signal is a time-dependent frequency signal. While a detailed understanding of the ramp mechanism is beyond the scope of this project, it is important to note that the ODF files for Magellan contain ramp tables for the tracking instances that used ramped frequencies. Thus, for each day, the properties of ramped signal (e.g.: start-end time, ramp frequency), corresponding to each actively tracking station, is extracted from ODF files and stored separately.

Once the observation files are prepared for each day (24 hour arcs), the next step is to pre-process the daily observations to eliminate poor tracking data-points that can degrade the orbits during LSQ fit. There are several established procedures to pre-process the tracking data. One convenient and easy-to-follow procedure is to compute Doppler observation data with the best available spacecraft states, that give minimum residuals, and then eliminate the data points that are larger than a factor times

---

[3] `http://pds-geosciences.wustl.edu/missions/magellan/index.htm`

standard deviation of the residuals. For the case of working with Bernese GNSS, the orbits determined by Konopliv et al., [1999] for developing state-of-art gravity model of 180 D/O were used to compute Doppler observables. The spacecraft states were directly extracted from SPICE kernels, compiled by Konopliv et al., [1999], and were used to generate computed value of the tracking data. In order to do this, SPICE toolkit was integrated into the routine that computes Doppler observations[4]. The outlying data points, as a rule of thumb beyond 2 times the standard deviation of the residuals, were eliminated.

Another point to be mentioned is that observation sampling time of 10 seconds was selected to extract the Doppler data. A sampling time less than 10 seconds leads to more observations but also more noise. Statistically, the reduction in noise with increase in sampling time can be understood as follows.

For observation distribution of x_i, averaged over N observation epochs, the sum of observation is formulated as:

$$x_{sum} = \sum_{i=0}^{N-1} x_i \tag{4.1}$$

with variance,

$$\sigma_{sum}^2 = \sum_{i=0}^{N-1} \sigma_i^2 \tag{4.2}$$

Now, if x_i are independent observations, then the average of these observations is given by:

$$x_{average} = \frac{1}{N} \sum_{i=0}^{N-1} x_i \tag{4.3}$$

with variance,

$$\sigma_{average}^2 = \frac{1}{N} \sum_{i=0}^{N-1} \sigma_i^2 \tag{4.4}$$

or,

$$\sigma_{average} = \frac{\sigma_i}{\sqrt{N}} \tag{4.5}$$

Thus, from eq. (4.5), it can be seen that the averaged-standard deviation, $\sigma_{average}$, of observations with standard deviation, σ_i, reduces by a factor of square of samples, $\sqrt{N}$. Now it is important to know that noise signal of X-band spectrum is significantly less than the signals due to orbit perturbations [4]. As a result, the choice of sampling time of 10 seconds was found to be optimum for scientific orbit determination and required less computational effort. This is also in agreement with the sampling time chosen by Konopliv et al., [1999] [4].

Radio signals traveling through Earth's atmosphere are subjected to atmospheric refraction that cause the signal to bend; this is especially true when the signal path is not parallel to the density gradient of the atmosphere [52]. Such bending of the signal path, that causes a propagation delay in the signal, is mainly observed in lower atmosphere, troposphere to be specific, and increases for elevation angles that are less than 10 degrees. As a result, modeling techniques to account for the atmospheric delay must be incorporated in orbit determination software. The tropospheric calibrations are based on a seasonal model developed by Chao, [1974] that accounts for dry and wet zenith delays that are represented as polynomial fits of the delay values estimated from the monthly averages of surface meteorological measurements. The errors in Chao's seasonal model can be as large as 0.003 Hz (or 0.1 mm/s) for data for elevations less than 10 degrees [6][5]. As a result, extensive investigation in the

---

[4] `SPKEZ`- This function of the SPICE toolkit was used to obtain Magellan's position at a given epoch directly from the SPICE kernels. A detailed information on the function and instructions for implementation can be found at: `ftp://naif.jpl.nasa.gov/pub/naif/toolkit_docs/FORTRAN/spicelib/spkez.html`.

[5] To convert error (ϵ) in Hz to m/s, a simple rule of thumb is used: $\epsilon_{m/s} = \epsilon_{Hz} c / F_{ref}$, where $F_{ref} \approx 8 \times 10^9$ Hz for X-band link and c is the speed of light in m/s.

tropospheric calibrations for low elevations has not been pursued and the data below 10 degrees elevation have been removed. However, one can further read a comparative survey for media calibrations compiled by Estefan et al., [1994] for developing strategies to use low elevation data (for example: de-weighting tracking data less than 10 degrees elevation) [52].

4.3. Geometric Models

The planetary ephemeris is given by the state-of-the-art DE430 model developed by Jet Propulsion Laboratory, California (JPL). The coordinate system, in which the planetary states are specified, is defined by an axis system that coincides with International Celestial Reference System (ICRS), with X-Y plane closely aligned to the mean equator of J2000 epoch and the origin located at the solar system barycenter [53]. It is important to highlight that the documentation of DE430 specifies that the state vectors of Venus have been improved, compared to its predecessor DE421, by using Very Long Baseline Interferometry (VLBI). However, it can be seen in Figure A.1 of Appendix that switching to DE430 from DE421 has no significant effect on the estimated orbits and consequently on the Doppler residuals. Thus, in case DE430 is not available, one can comfortably use DE421 while sacrificing few centimeters of accuracy[6].

Magellan was tracked by DSN stations 12, 14, 15, 42, 43, 45, 61, 63 and 65 [6]. The geocentric Cartesian station coordinates are given as per ITRF93 reference frame at epoch 1993.0 (see Table 4.1). To transform the station coordinates to another epoch (for instance, to May 1994), the site velocities must be used (see Table 4.2). The formal uncertainties in station coordinates is about 2-3 cm, which can be safely neglected as the effect on Doppler residuals is around 0.0003 Hz (or 0.01 mm/s) [6].

Antenna	X-axis [m]	Y-axis [m]	Z-axis [m]
DSS 12	−2350443.812	−4651980.837	3665630.988
DSS 14	−2353621.251	−4641341.542	3677052.370
DSS 15	−2353538.790	−4641649.507	3676670.043
DSS 42	−4460981.016	2682413.525	−3674582.072
DSS 43	−4460894.585	2682361.554	−3674748.580
DSS 45	−4460935.250	2682765.710	−3674381.402
DSS 61	4849245.211	−360278.166	4114884.445
DSS 63	4849092.647	−360180.569	4115109.113
DSS 65	4849336.730	−360488.859	4114748.775

Table 4.1: Cartesian coordinates of DSN antennas in the ITRF93 reference frame at epoch 1993.0 [3].

Station	X-axis [m/yr]	Y-axis [m/yr]	Z-axis [m/yr]
Goldstone (1X)	−0.0191	0.0061	−0.0047
Canberra (4X)	−0.0354	−0.0017	0.0412
Madrid (6X)	−0.0141	0.0222	0.0201

Table 4.2: DSN site velocities in the ITRF93 reference frame. The “X” in the bracket indicates a digit in unit place [3].

The body-fixed coordinate system for Venus is specified by the Pole Right Ascension and Declination, given in Earth-Mean-Equator of J2000, and Rotation Rate estimated by Konopliv et al., [1999] for 180 D/O gravity field [4]. It is important to highlight that the planetary body-fixed coordinate system and the rotational elements are also available by IAU/IAG Working Group, that provides standardized system of coordinates for astronomical bodies. A comparison of the relevant values are presented n Table 4.3.

---

[6] For more information, the reader can follow “The Planetary and Lunar Ephemerides DE430 and DE431” [53].

Parameter	*Konopliv et al., [1999]*	*Davies et al., [2006]*
Pole Right Ascension $[deg]$	272.743 ± 0.002	272.76 ± 0.02
Pole Declination $[deg]$	67.156 ± 0.001	67.16 ± 0.01
Rotation Rate $[days]$	243.0200 ± 0.0002	243.0185 ± 0.0001

Table 4.3: Cartographic coordinates and rotational elements along with their formal errors for *Konopliv et al., [1999]* and *Davies et al., [2006]* [4], [5]

From Table 4.3, one can easily compute that the Rotation Rate will have a measurable impact, over short time-frames, on the estimated orbits for a given location of Prime Meridian. Assuming that the radius of Venus is 6051 km with Prime Meridian located at 160.20 degrees, then the difference between location of Prime Meridian after one full Venusian rotation, for Konopliv et al., [1999] and Davies et al., [2006], will be 9.3×10^{-6} degrees (or approximately 56 m on the surface). Given the ambiguity in orbit determination, to choose the best set of rotational elements, a sensitivity test is shown in Figure A.2 of Appendix to highlight the impact on estimated orbits for both choices.

4.4. Spacecraft Modeling

4.4.1. Cannon-ball Model

The simplest form of spacecraft modeling, to estimate surface forces, is the cannon-ball model. In this case, the spacecraft is assumed to be non-rotating sphere with uniform optical properties and a fixed drag coefficient, that are eventually corrected by estimated scaling factors for the surface forces. The methodology to model the surface forces using cannon-ball is exactly the same as discussed in Chapter 3.

4.4.2. Macro-model

A macro-model, with moving solar panels and varying exposed area of the spacecraft with respect to each surface force, assumes major parts of the spacecraft body to be made of flat panels and allows for more intricate modeling of the surface forces, while keeping low computational time.

A 3D CAD model of Magellan, shown in Figure 4.3, was developed by using commercially available software, Autodesk 360. The dimensions of major components are explicitly given in "The Magellan Venus Explorer's Guide", compiled by Young [1990] [54]. A 16-plate macro-model ASCII file, similar to the one shown in Figure 1.4, tabulated in Table A.1 of Appendix was created that specifies the plate-area of each component and its orientation with respect to spacecraft axis system defined as per the documentation of solar vacuum test of Magellan spacecraft, compiled by Neuman [1991], (see Figure 4.4) [10].

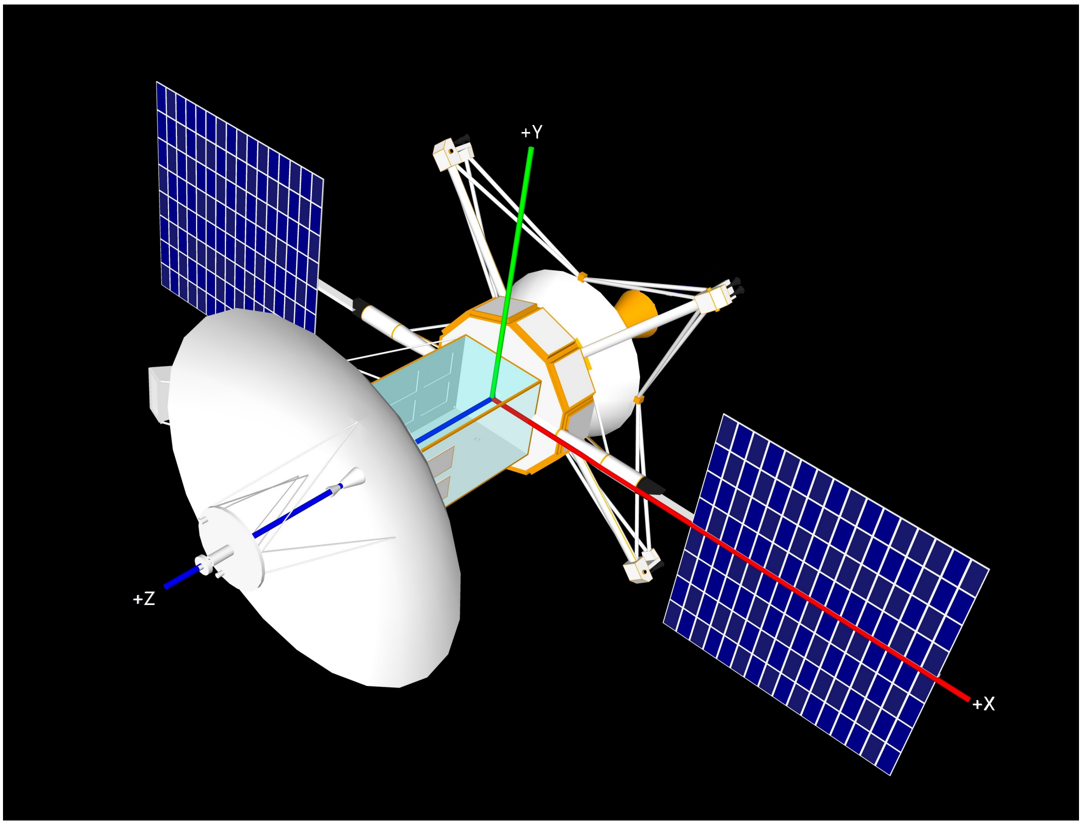

Figure 4.3: 3D CAD model with positive Z-axis pointing towards the direction of HGA, positive X-axis passing through the solar panel axis boom, and Y-axis completing the right-hand coordinate system.

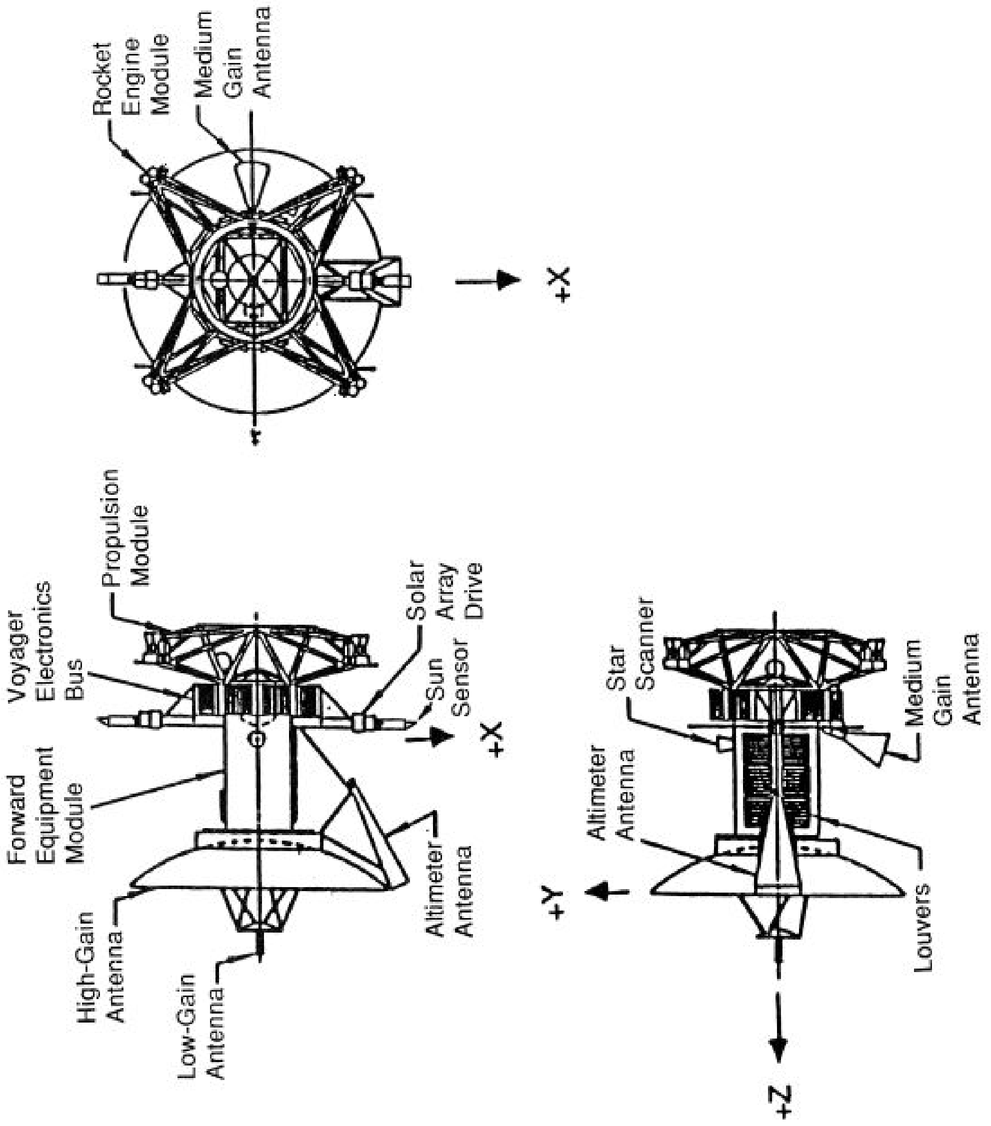

Figure 4.4: A sketch of Magellan spacecraft that shows the spacecraft axis system along with the labels of each component [10].

To fully implement a macro-model, it is important to know the optical properties of each panel and the spacecraft's attitude with respect to a reference frame in which the equations of motion are integrated. The accurate values for optical properties and attitude data (in form of quaternions) are not available in the literature. While choosing the right combination of optical properties is tedious and time-consuming process, it is possible to implement an attitude configuration, in form of rotation matrix that relates a given reference frame to the spacecraft frame, by establishing fundamental assumptions. However, an assumed attitude will never be able to represent the real scenario and may require series of fine tuning to incorporate hide maneuvers and star track calibration that are briefly discussed in Section 1.5 of Chapter 1. This project will establish a starting point for the attitude assumption of Magellan mission during gravity phases that may support future work on Venusian gravity recovery.

For this project, based on the discussion in Section 1.5 of Chapter 1, it was decided to implement two different attitude configurations. The resulting orbits, Doppler residuals, empirical and pseudo-stochastic parameters can be used to infer the impact of using different attitude configurations. To implement two attitude configurations, following are the assumptions taken into consideration:

1. The HGA (+Z) will be looking towards Earth during DSN tracking. However, in this project, +Z axis will be aways looking towards Earth.
2. The solar panels (±X) will be aligned with the velocity vector for minimum drag configuration.
3. The solar panel will be looking towards Sun for maximum power throughput. In other words, the angle between the solar panel axis and spacecraft-Sun unit vector will be 90 degrees.

Points 1 and 2 form the basis for the first attitude configuration (ATT_1),while points 1 and 3 will form the basis for the second attitude configuration (ATT_2). A mathematical derivation of ATT_1 is also provided in Section A.1.

For ATT_1, the derived rotation matrix that relates spacecraft reference frame to the inertial frame, J2000, can be given as

$$\begin{bmatrix} \hat{\mathbf{e_x}} \\ \hat{\mathbf{e_y}} \\ \hat{\mathbf{e_z}} \end{bmatrix} = \begin{bmatrix} \frac{\mathbf{V} - (\mathbf{V}.\hat{\mathbf{e_z}})\hat{\mathbf{e_z}}}{\sqrt{|\mathbf{V}|^2 - (\mathbf{V}.\hat{\mathbf{e_z}})^2}} \\ \hat{\mathbf{e_x}} \times \hat{\mathbf{e_z}} \\ \hat{\mathbf{r}}_{Earth} \end{bmatrix}, \tag{4.6}$$

where
$\mathbf{V}$ → spacecraft's velocity vector in J2000 reference frame $[m/s]$,
$\hat{\mathbf{r}}_{Earth}$ → spacecraft-Earth unit vector in J2000 frame.

The rotation matrix for ATT_2 can derived to as

$$\begin{bmatrix} \hat{\mathbf{e_x}} \\ \hat{\mathbf{e_y}} \\ \hat{\mathbf{e_z}} \end{bmatrix} = \begin{bmatrix} \frac{\hat{\mathbf{e}}_{\odot} \times \hat{\mathbf{e_z}}}{|\hat{\mathbf{e}}_{\odot} \times \hat{\mathbf{e_z}}|} \\ \hat{\mathbf{e_x}} \times \hat{\mathbf{e_z}} \\ \hat{\mathbf{r}}_{Earth} \end{bmatrix}, \tag{4.7}$$

where
$\hat{\mathbf{e}}_{\odot}$ → spacecraft-Sun unit vector in J2000 frame.

Thus the rotation matrix given by eqs (4.6) and (4.7) respectively provides the orientation information for each spacecraft reference frame axis in a direction specified by the RHS matrix with respect to the J2000 frame. A word of caution to be mentioned regarding the first element of RHS matrix in eq. (4.7) is that the cross product, $\hat{\mathbf{e}}_{\odot} \times \hat{\mathbf{e_z}}$, may create a singularity in the rotation matrix, leading to a degeneration of three-degree of freedom to two-degree of freedom. However, this can occur only for Superior and Inferior Conjunctions, during which the cross product of spacecraft-Sun unit vector and spacecraft-Earth unit vector will be equal to (or close to) zero. Since, the tracking data during Superior Conjunction (between 8-January-1994 to 28-January-1994 for Magellan mission) are usually removed due to strong charged particle corruption, this singularity shouldn't be a concern[7].

The modeling of surfaces forces for macro-model approach is fundamentally the same as that for cannon-ball. However, the accelerations are estimated for each panel and are eventually summed up. Thus, for a macro-model with N plates, the acceleration due to drag forces can be given as per [46]

$$\ddot{\mathbf{r}}_{Drag} = C_D \sum_{j=1}^{N} \frac{1}{2} \frac{A_j}{m} \rho_{\infty} V_{atm}^2 (\hat{\mathbf{u}}.\hat{\mathbf{n}}_j), \tag{4.8}$$

where
$\hat{\mathbf{n}}_j$ → the unit vector normal to the panel j,

---

[7] Also, Magellan mission was terminated a month before Inferior Conjunction (from 27-October-1994 to 7-November-1994)

C_D → drag coefficient,
A_j → plate area of panel j,
ρ_∞ → free-stream density,
V_{atm} → spacecraft's velocity with respect to the rotating atmosphere.

To model solar radiation pressure acceleration, the radiation coefficient, C_R can be analytically expressed as a vector of the contributions from absorbed, diffusely reflected and specularly reflected photon particles for each panel. This can be expressed for a panel j as

$$\mathbf{C}_{R,j} = (1 - \epsilon_{s,j} - \epsilon_{d,j})\hat{\mathbf{r}}_\odot + 2\epsilon_{s,j}(\hat{\mathbf{r}}_\odot . \hat{\mathbf{n}}_j)\hat{\mathbf{n}}_j + \epsilon_{d,j}\left(\hat{\mathbf{r}}_\odot - \frac{2}{3}\hat{\mathbf{n}}_j\right), \tag{4.9}$$

where
$\epsilon_{d,j}$ → coefficient of diffuse reflection for panel j $[-]$,
$\epsilon_{s,j}$ → coefficient of specular reflection for panel j $[-]$.

The net acceleration due to solar radiation pressure can be obtained by summing accelerations over each panel $j$and is given as

$$\ddot{\mathbf{r}}_{SRP} = \sum_{j=1}^{N} \mathbf{C}_{R,j} \frac{A_j}{m} P_\odot f(\hat{\mathbf{r}}_\odot . \hat{\mathbf{n}}_j), \tag{4.10}$$

A similar radiation coefficient, as eq. (4.9), can be obtained for each surface element i of planet to model planetary radiation pressure and is given as

$$\mathbf{C}_{R,ij} = (1 - \epsilon_{s,j} - \epsilon_{d,j})\hat{\mathbf{r}}_{ELE,i} + 2\epsilon_{s,j}(\hat{\mathbf{r}}_{ELE,i} . \hat{\mathbf{n}}_j)\hat{\mathbf{n}}_j + \epsilon_{d,j}\left(\hat{\mathbf{r}}_{ELE,i} - \frac{2}{3}\hat{\mathbf{n}}_j\right), \tag{4.11}$$

Finally, the net acceleration due to planetary radiation pressure is given as

$$\ddot{\mathbf{r}}_{PRP} = \sum_{i=1}^{M}\sum_{j=1}^{N} \mathbf{C}_{R,ij} \frac{A_j}{m} P_{PRP,i}(\hat{\mathbf{r}}_{ELE,i} . \hat{\mathbf{n}}_j), \tag{4.12}$$

The direct solar radiation pressure, $P_\odot$, and combined pressure due to planetary albedo and infrared radiation, $P_{PRP,i}$, are estimated as per the mathematical formulation in Chapter 3.

4.4.3. Scaling Factors

The chosen aprioiri values of non-gravitational force parameters are not accurate[8]. As a result, the surface accelerations are required to be scaled so that they can closely represent the realistic magnitudes for which the tracking residuals are minimal. For this purpose, each surface acceleration is multiplied by a scaling parameter. Thus, aerodynamic acceleration can be written as

$$\ddot{\mathbf{r}}_{Drag} = M_{SC,D} C_D \sum_{j=1}^{N} \frac{1}{2}\frac{A_j}{m} \rho_\infty V_{atm}^2 (\hat{\mathbf{u}} . \hat{\mathbf{n}}_j), \tag{4.13}$$

where
$M_{SC,D}$ → the drag scaling parameter.

The accelerations due to solar and planetary radiation pressures with the introduced scaling parameters, $M_{SC,SRP}$ and $M_{SC,PRP}$, are given as:

$$\ddot{\mathbf{r}}_{SRP} = M_{SC,SRP} \sum_{j=1}^{N} \mathbf{C}_{R,j} \frac{A_j}{m} P_\odot f(\hat{\mathbf{r}}_\odot . \hat{\mathbf{n}}_j), \tag{4.14}$$

---

[8] For example, parameters like drag coefficient (C_D), optical properties, spacecraft mass and area.

and

$$\ddot{\mathbf{r}}_{PRP} = M_{SC,PRP} \sum_{i=1}^{M} \sum_{j=1}^{N} \mathbf{C}_{R,ij} \frac{A_j}{m} P_{PRP,i} (\hat{\mathbf{r}}_{ELE,i} . \hat{\mathbf{n}}_j), \tag{4.15}$$

The values of $M_{SC,D}$, $M_{SC,SRP}$ and $M_{SC,PRP}$ are estimated along with initial conditions during LSQ-adjustment. The values of the estimated scaling factors are strong indicators of the quality of implemented surface forces. In other words, for a perfect modeling of surfaces forces, the scaling factor for each force will be equal to 1. Any deviation from unity indicates imperfect modeling[9]. The intention of using scaling factors is to improve our apriori assumptions about spacecraft mass, area, attitude and the optical properties, and the density model itself.

---

[9] For example, a scaling factor of 0.5 for air-drag suggests that the modeled acceleration is twice the magnitude of the expected value, hence the acceleration is scaled down by a factor of 2. On the other hand a scaling factor of 2 indicates that the modeled acceleration is half the magnitude of the expected value, hence it is scaled up by a factor of 2.

5

Verification & Validation

This chapter presents Verification and Validation results to demonstrate the robustness and correctness of the implemented models for non-gravitational accelerations. First, Verification of the implementation is presented in Section 5.2 to show that the implemented models exhibit correct physical behavior. Subsequently, Validation in form of "back of the envelope", and their comparison with modeled values (or magnitudes), is discussed in Section 5.3 to demonstrate the absolute correctness of the models. Furthermore, validation by manual calculations is further reinforced with assessing the impact on orbits and empirical and pseudo-stochastic parameters in Sections 5.3.4 and 5.3.5 respectively.

5.1. Test Setup

The orbit parametrization is kept simple for all the cases of Verification and Validation. This means that no empirical or pseudo-stochastic parameters are used and the setup is restricted to orbit propagation from initial conditions that are taken from SPICE orbits. Based on initial tests, the coefficients of surface forces, namely C_D and C_R are fixed with assumed values. The spacecraft's mass is assumed to be 2,500 kg, while the effective radius for cannonball model is obtained by summing the area of all flat plates in the macro-model and equating it to the surface area of sphere (see Table A.1 of Appendix to know the plate areas). Table 5.1 summarizes the orbit setup.

Option	Value	Comments (if any)
Gravity Field	SHGJ180U	Extended to 180 D/O
Integration Step Size	10 s	Fixed
Solid Tides	$K_2 = 0.295$	Source: [6]
JPL Ephemeris	DE430	-
Drag	Venus-GRAM Density Package	Fixed $C_D = 1.25$
SRP	-	Fixed $C_R = 1.4$
PRP	Numerical Grid Model	R-PRP and E-PRP active
Spacecraft Model	Cannon-ball	Radius =1.83 m

Table 5.1: Orbit determination setup for Verification and Validation (V & V) in *Bernese GNSS Software*. The values of C_D and C_R are assumed as per the orbit parametrization kindly provided by GSFC, NASA.

5.2. Verification

Verification results are presented to demonstrate that the necessary framework for non-gravitational force modeling has been correctly implemented in Bernese GNSS Software and the true physical behavior of forces are present in the orbit model. For this purpose, Day 131 of 1994 is chosen for which the angle between orbital plane and Sun (also known as β-angle) is close to zero, particularly to verify the implementation of radiation pressures.

5.2.1. Drag

The implementation of aerodynamic drag can be verified by observing the angle between drag acceleration vector and spacecraft's velocity vector relative to the atmosphere. Ideally, for cannonball model, this angle should be equal to 180 degrees because aerodynamic drag is a resistive force that will act against the direction of motion.

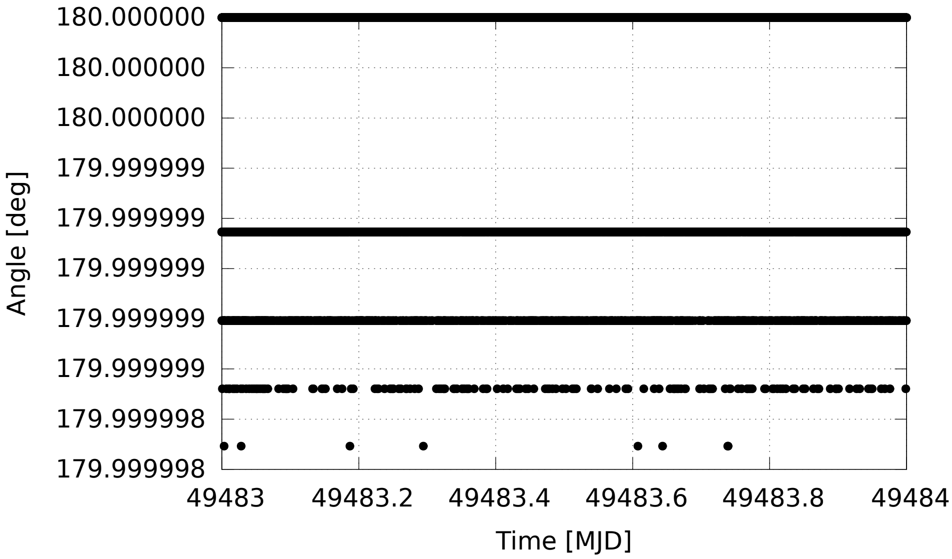

Figure 5.1: Verification of drag force by computing the angle between drag acceleration and the spacecraft velocity vector with respect to the atmosphere. As expected, this angle is equal to 180 degrees with negligible numerical errors.

5.2.2. Solar Radiation Pressure (SRP)

A simple strategy to validate SRP force is to observe the angle between spacecraft-Sun unit vector and the SRP acceleration vector. For a correct implementation, this angle should be equal to 180 degrees.

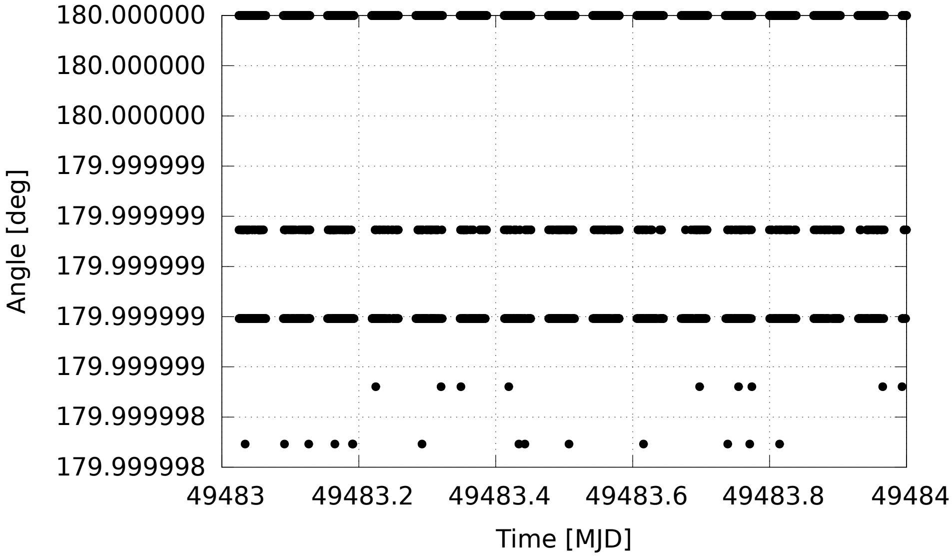

Figure 5.2: Verification of SRP force by computing the angle between SRP acceleration and the spacecraft-Sun unit vector. This angle is equal to 180 degrees with negligible numerical errors.

5.2.3. Reflected Planetary Radiation Pressure (R-PRP)

Verification of R-PRP force requires a specific day for which the β-angle is zero. For this purpose, the evolution of β-angle throughout the year 1994 was obtained and is shown in Figure 5.4. From this figure, one can see that the β-angle is virtually zero for four specific days. Out of these days, Day 131 was chosen. For the day with β-angle equal to zero, the angle between SRP acceleration vector and R-PRP acceleration vector must be equal to 180 degrees when the spacecraft is exactly between Sun and Venus at one instance in the orbit.

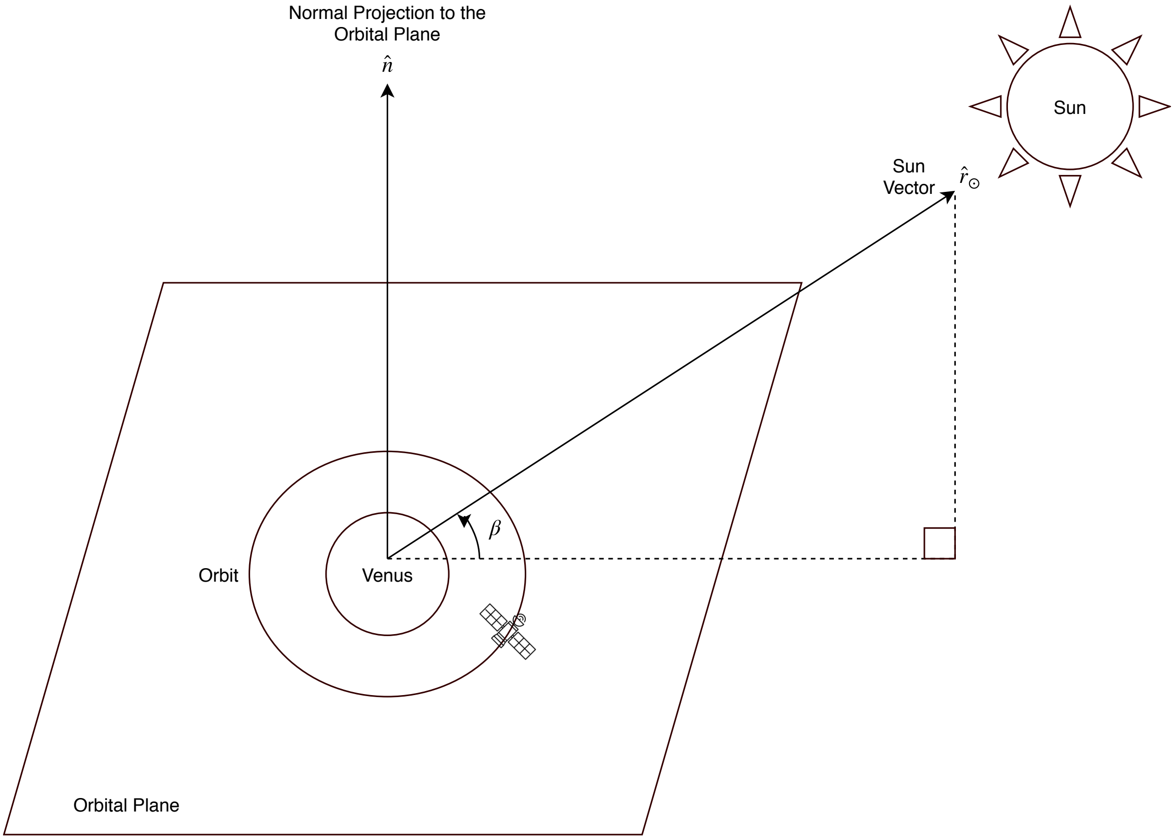

Figure 5.3: Schematic illustration of β-angle. It is defined as the angle between orbital plane and the unit vector, $\hat{\mathbf{r}}_\odot$, to Sun.

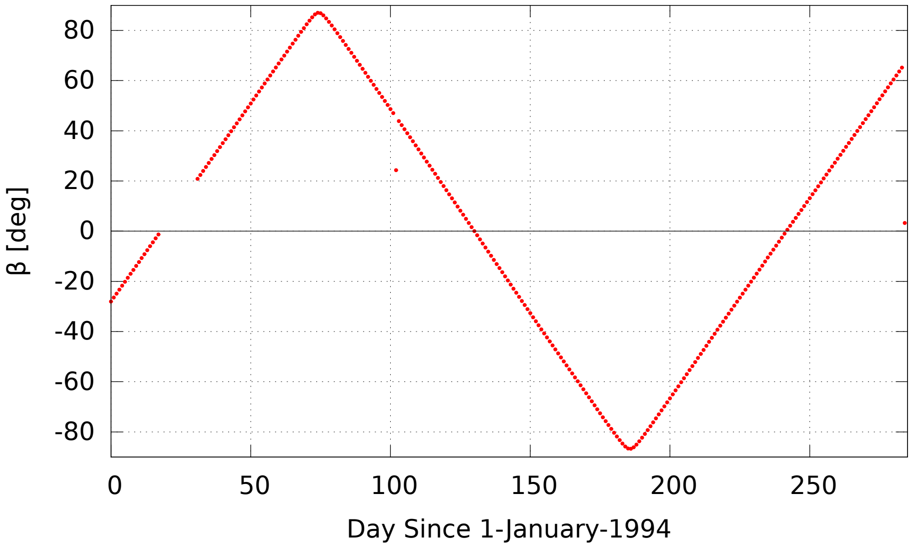

Figure 5.4: Daily values of β-angle starting from 1-January-1994 to 13-October-1994 (end of mission). The gap/discontinuity observed between Day 0 and Day 50 pertains to the days with Superior Conjunction during which the tracking data were corrupted due to solar interference. As a result, the tracking data were excluded from processing [4]. Furthermore some outliers in the plot correspond to days with poor orbit estimation present in SPICE orbits.

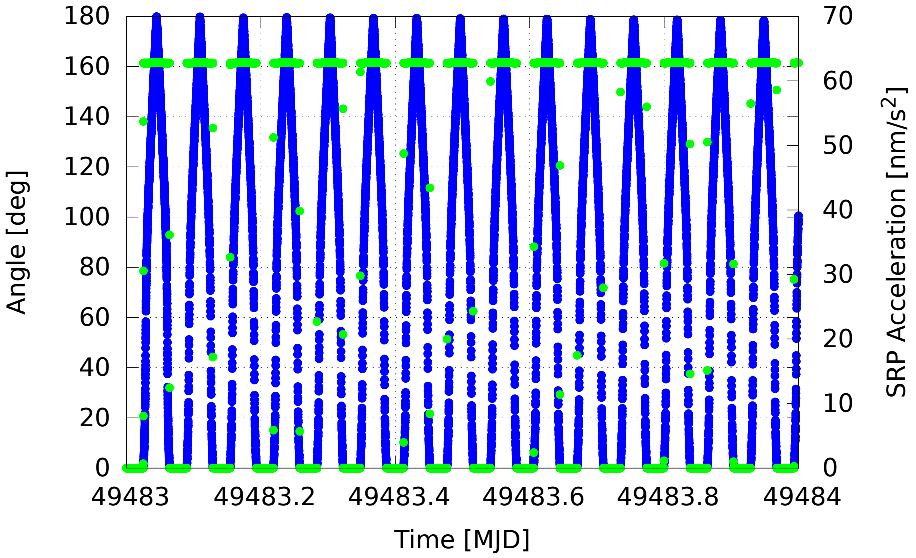

Figure 5.5: Verification of R-PRP force by computing the angle (shown in blue) between R-PRP an SRP acceleration vectors for a day when β-angle is close to zero (Day 131). The SRP acceleration (shown in green) is imposed on the angle plot. It can be seen that the angle between R-PRP and SRP acceleration vectors becomes 180 degrees when Magellan is exactly between Venus and Sun, in this case the direction of SRP and R-PRP is exactly the opposite and can be observed approximately at the middle of sunlight condition.

5.2.4. Emitted Planetary Radiation Pressure (E-PRP)

To verify E-PRP force, one can observe the angle between spacecraft position vector and E-PRP acceleration vector, both expressed in same reference system. The E-PRP acceleration vector will be directed radially away from the surface towards spacecraft. As a result, the position vector and the E-PRP acceleration will be more or less aligned in the same direction, leading to an angle value of zero. However, from Figure 5.6, the values of this angle are not exactly zero but rather oscillate between 0 and 0.07, exhibiting periodic variations. This is because of the fact that the entire Venusian surface is divided into small elements to model the E-PRP acceleration. Furthermore, Magellan's orbit is near-polar with an inclination of 85^o. As a result, depending on its location over the planetary surface, the spacecraft sees different number of grids cells that contribute with different magnitudes, due to which the the E-PRP acceleration vector is inclined with respect to the spacecraft's position from the central body.

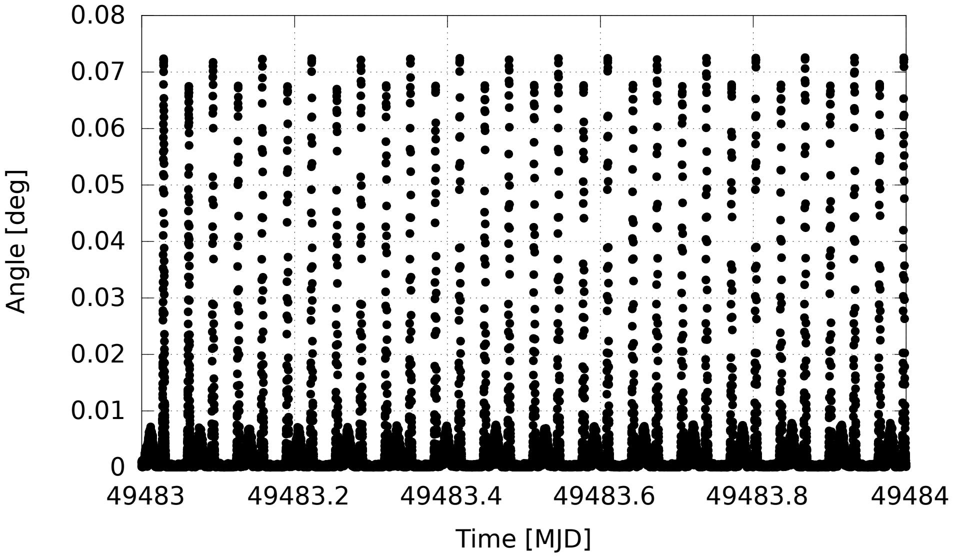

Figure 5.6: Verification of E-PRP force by computing the angle between E-PRP acceleration vector and the spacecraft position vector. Ideally this angle should be exactly equal to zero. However, the small non-zero values are mainly due to contributions from multiple planetary surface elements, depending on spacecraft's location, due to which the direction of force is slightly inclined with respect to the spacecraft position vector.

5.3. Validation

While the implementation is verified to be correct, it is important to validate the implemented non-gravitational force models to make sure that the expected magnitudes of accelerations are produced. There are various strategies to perform the validation. One easy and convincing way is to compare the shapes of acceleration curves with that from another independent software (for e.g. GEODYN from GSFC). However, it was not possible to procure the relevant data required for comparison on time. Instead, "back of the envelope" calculations are presented by using a simple cannonball model. Furthermore, the validation is reinforced by orbit determination and parameter estimation, with SPICE state vectors as observations to highlight the relative improvement in estimated orbits and reduction of empirical accelerations.

Numerous sources are available for choosing the required model for non-gravitational forces. However, the fundamental models for cannonball spacecraft are similar throughout the various sources encountered during literature study. The implemented mathematical models in Bernese GNSS Software v5.3, when compared with independent sources such as that documented by Tapley et al., [2004] and Wakker., [2015] are consistent with external sources[1]. As a result, validation is done in form of manual calculation, followed by orbit determination by using SPICE positions as observations. It is important to note that $C_R = 1.4$ ($\delta = 0.87$, see Section 3.2 of Chapter 3) and $C_D = 1.25$ are assumed as per the orbit tests and setups provided by GSFC, NASA. Furthermore, the spacecraft mass of 2,500 kg is an assumed value, considering that the dry mass is $1,135$ kg and the fuel tank holds roughly $1,000$ kg of propellant. Lastly, the area of cannonball model, $A = 10.52$ m^2 is consistent with that given in Venus Gravity Handbook [6].

---

[1] See Chapter 20 of [55] and Chapter 2 of [26]

5.3.1. Validation Of SRP

For a spherical spacecraft geometry, the equation for direct radiation pressure acceleration is given as (see Section 3.2 of Chapter 3)

$$\ddot{\mathbf{r}}_{SRP} = C_R \frac{A}{m} P_\odot \hat{\mathbf{r}}_\odot, \tag{5.1}$$

where
C_R → radiation coefficient [-],
A → area of the spacecraft illuminated by Sun $[m^2]$,
m → spacecraft mass $[kg]$,
$P_\odot$ → mean solar radiation pressure at spacecraft's position $[N/m^2]$,
$\hat{\mathbf{r}}_\odot$ → Sun-to-spacecraft unit vector.

The mean solar radiation pressure at 1 AU is given as,

$$P_{\odot 1AU} = \frac{\Phi_{\odot 1AU}}{c} \tag{5.2}$$

where,
$\Phi_{\odot 1AU}$ → the mean solar flux which is approximately equal to 1370 W/m^2 [56],
c → speed of light approximated as 3×10^8 m/s.

Now for the back of the envelope calculations, it is assumed that $\beta = 90^o$, i.e. the spacecraft is in constant sunlight. Furthermore, the value of variables used for manual calculations are tabulated in Table 5.2:

Variable	Value	Dimension
C_R	1.4	[-]
A	10.52	$[m^2]$
c	3.0E8	$[m/s]$
M	2,500	$[kg]$
$r_\odot$	0.72	$[AU]$
$\Phi_{\odot 1AU}$	1,370	$[W/m^2]$

Table 5.2: Assumed values of variables. Here A is the circular cross-section area with radius 1.83 m

The radiation pressure at spacecraft distance is given as

$$P_\odot = \left(\frac{1\ AU}{r_\odot}\right)^2 P_{\odot 1AU}. \tag{5.3}$$

Now, the mean solar radiation pressure at 1 AU is:

$$P_{\odot 1AU} = \frac{1370}{3 \times 10^8} = 4.56 \times 10^{-6}\ N/m^2$$

The radiation pressure at spacecraft distance is:

$$P_\odot = 4.56 \times 10^{-6} \left(\frac{1AU}{0.72\ AU}\right)^2 = 8.79 \times 10^{-6}\ N/m^2$$

Finally, the magnitude of acceleration due to direct radiation pressure is:

$$\ddot{r}_{SRP} = 1.4 \times \frac{10.52}{2500} \times 8.79 \times 10^{-6} = 5.2 \times 10^{-8}\ m/s^2$$

Thus, in full sunlight, the expected magnitude of acceleration due to direct radiation pressure must be close to the magnitude 5.2×10^{-8} m/s^2. The time series of SRP acceleration magnitude is shown for Day 76 of 1994 with $\beta = 86^o$

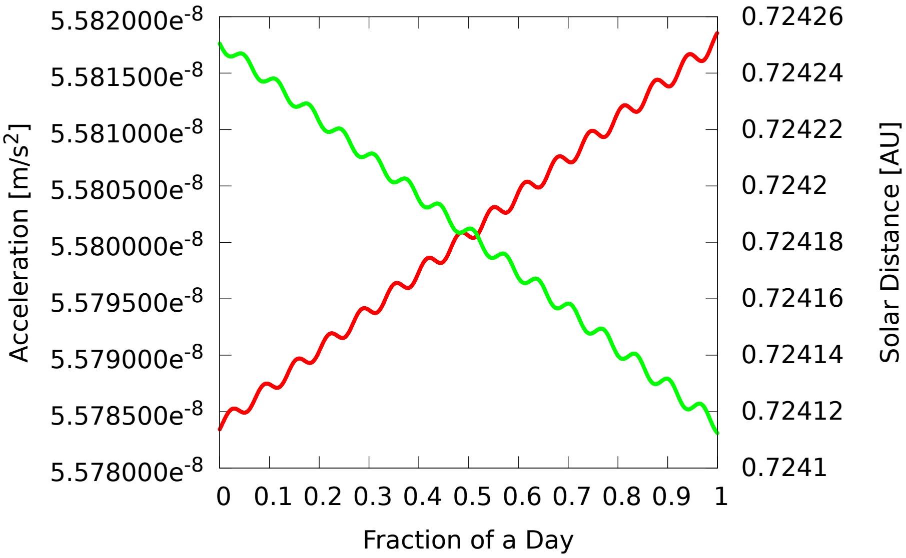

Figure 5.7: SRP acceleration magnitude observed on Day 76 of 1994 (shown in red). The Solar distance is shown in green.

From Figure 5.7, it can be seen that Magellan experiences no eclipse and is under constant sunlight, as expected for a day with $\beta = 90^o$. As a result, the spacecraft will experience near-constant SRP acceleration that will show insignificant periodic variation due to the orbital characteristics (eccentricity and distance from planet and Sun). Nevertheless, it can be seen that the modeled SRP acceleration magnitude is close to the back of the envelope value (roughly 7% more than the back of the envelope value). It is also worthwhile to see the behavior of acceleration magnitude between the periods of extreme β-angles.

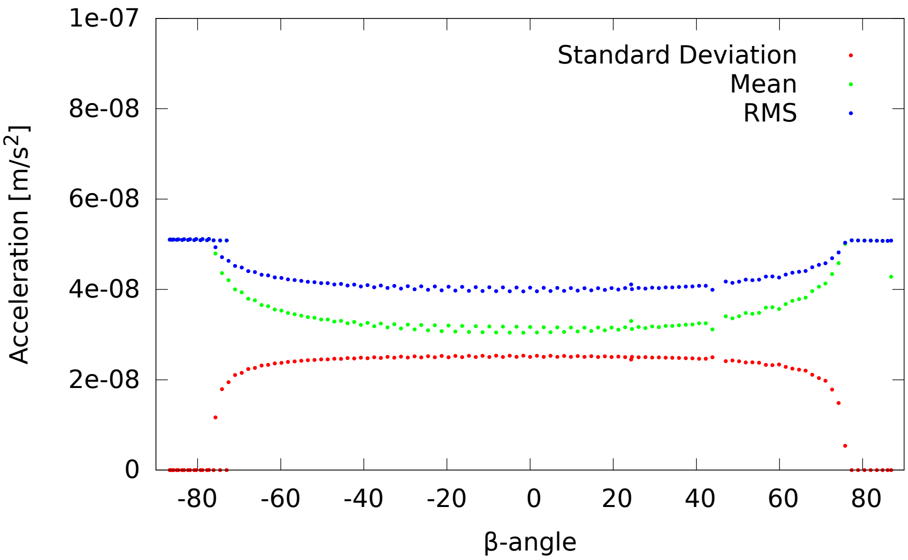

Figure 5.8: Daily statistical properties of modeled SRP acceleration between two extreme β-angles. The results are obtained between days 76-197 of 1994. The small periodic variations in each statistical properties, particularly observed between extreme β-angles, are due to the contributions of zero acceleration magnitudes, observed at different instant of time for each day, to the computed statistics. Furthermore, a steady increment in RMS and Mean values towards extreme β-angles indicate that the eclipse events are reducing.

The SRP acceleration magnitudes of the implemented model are computed between two extreme ranges of β-angles (see Figure 5.4) for year 1994 with the mass, area and radiation coefficient given in Table 5.2. It is expected that for $\beta = \pm 90^o$, Magellan will be in full sunlight throughout the orbit. As a result the variation in acceleration will only be a function of negligible change in the spacecraft-Sun distance. This means that the standard deviation in the acceleration will be less for $\beta = \pm 90^o$ and will increase as β-angle decreases with subsequent days. This is exactly what is seen in Figure 5.8. Furthermore, it can be observed that the mean value varies slowly over the entire period with a variation of 20% as β-angle changes from -90^o to $+90^o$. The near constant RMS values for extreme β-angles indicate that the spacecraft is always in the sunlight, due to which there is no obvious change in direct radiation acceleration magnitude. Finally, the standard deviation is the lowest at extreme β-angles, there by affirming a presence of constant sunlight during those days for which Sun is perpendicular to the orbital plane (see Figure 5.3 for visualizing). Furthermore, if observed carefully, one can see systematic variations in Mean and RMS of daily SRP acceleration magnitudes for low β-angles. This can be easily explained by the fact that the eclipses also contribute to the statistics and that Magellan experiences eclipse at same instance every second day, thereby leading to statistical variation that repeats after every second day for days with low β-angle. Thus, comparing back of the envelope calculation of expected acceleration magnitudes with that to the statistics given in Figure 5.8, it can be affirmed that implementation of SRP is correct and has been validated satisfactorily.

5.3.2. Validation Of PRP

R-PRP Validation

To validate Reflected Planetary Radiation Pressure (R-PRP), again a simple cannonball model is taken into consideration and back of the envelope calculations are done by assuming $\beta = 0^o$. Furthermore, it is assumed that Magellan is exactly between Sun and Venus (i.e. in sunlight). The acceleration due to R-PRP in this case can be modeled as (see Section 3.3 of Chapter 3):

$$\ddot{\mathbf{r}}_{R-PRP} = C_R \frac{A}{m} P_{R-PRP} \hat{\mathbf{r}}_{\oplus} \tag{5.4}$$

where,
C_R → radiation coefficient [-],
A → exposed area of the spacecraft $[m^2]$,
m → satellite mass $[kg]$,
P_{R-PRP} → reflected radiation pressure from the source $[N/m^2]$,
$\hat{\mathbf{r}}_{\oplus}$ →unit vector of spacecraft's CoM distance from the source $[-]$.

The reflected radiation pressure, (P_{R-PRP}), experienced by the spacecraft due to a planetary surface under constant sunlight is given as:

$$P_{R-PRP} = \frac{1\ AU}{|D_{\odot} - R_{\oplus}|^2} P_{\odot 1AU} \frac{A_{\oplus}\alpha}{\pi|\mathbf{r}|^2} \tag{5.5}$$

where,
$D_{\odot}$ → planetary distance from Sun $(\approx D_{\odot} = 0.72\ AU)$ $[m]$,
$\mathbf{r}$ → spacecraft's position from center of the planet expressed in inertial reference frame $[m]$,
α → planetary albedo,
$A_{\oplus}$ → illuminated planetary area $[m^2]$.

The table below summarizes all the values of variables used for validation:

Variable	Value	Dimension
C_R	1.4	[-]
A	10.52	$[m^2]$
$R_\oplus$	6,051	$[km]$
α	0.76	[-]
$P_{\odot 1AU}$	4.56×10^{-6}	$[N/m^2]$
$\lvert\mathbf{r}\rvert$	6,351	$[km]$

Table 5.3: Assumed values of variables. Here A is the circular cross-section area with radius 1.83 m and the orbital altitude of the spacecraft is assumed to be 300 km.

Now, using the values of above table in eqs. 5.4 and 5.5:

The R-PRP pressure at spacecraft distance is:

$$P_{R-PRP} = 4.56 \times 10^{-6} \left(\frac{1AU}{0.72\ AU} \right)^2 \times \frac{\pi \times 6051000^2 \times 0.71}{\pi \times 6351000^2} = 5.7 \times 10^{-6}\ N/m^2$$

Finally, the R-PRP acceleration is estimated as:

$$\ddot{\mathbf{r}}_{R-PRP} = 1.4 \times \frac{10.52}{2500} \times 5.7 \times 10^{-6} = 3.4 \times 10^{-8}\ m/s^2$$

Thus, it is expected that the magnitude of R-PRP acceleration will be approximately equal to the above calculated value, when Magellan is exactly between Sun and Venus. Furthermore, Magellan's orientation with respect to Sun and Venus at a given instant can be known by computing the dot product of spacecraft-Sun and Venus-spacecraft unit vectors.

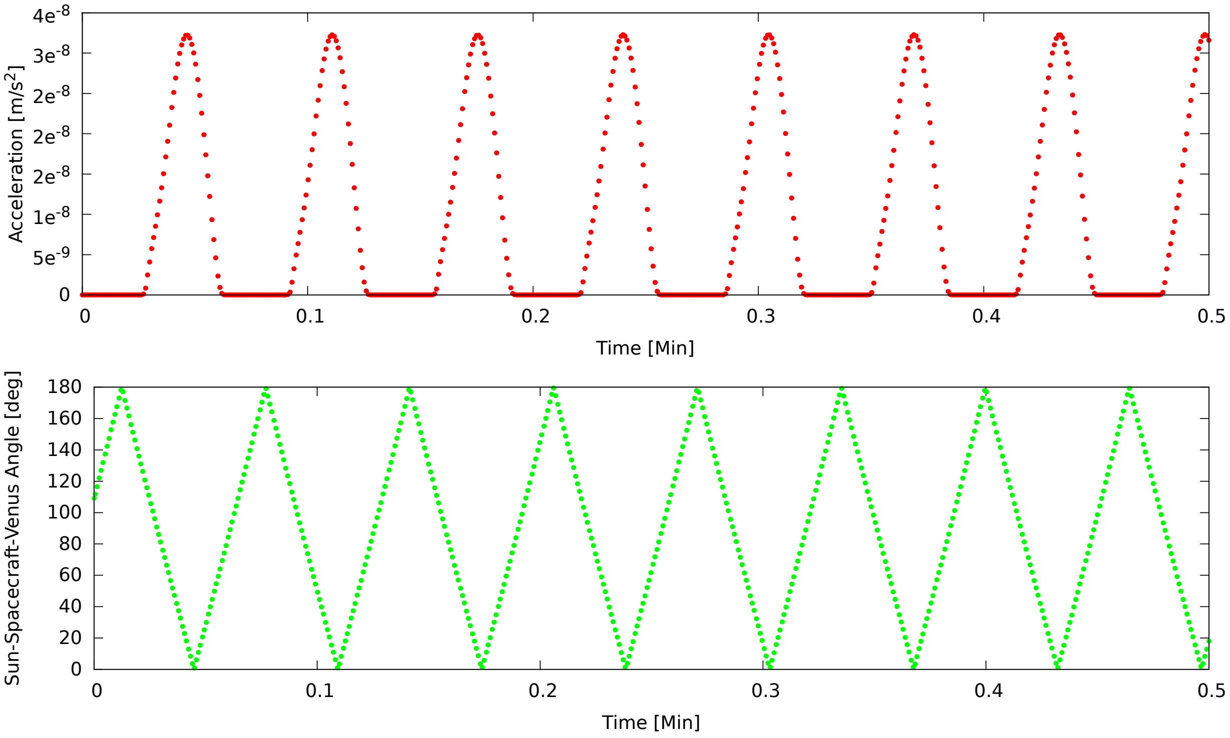

Figure 5.9: Top: R-PRP acceleration magnitude. **Bottom:** Angle between spacecraft-Sun and Venus-spacecraft unit vectors. The plot is sampled for every 100 data points.

From Figure 5.9, it is intuitively understood that Magellan is in full sunlight when it is exactly in between Sun and Venus (angle is zero), due to which the R-PRP acceleration magnitude is highest. At this instant, the magnitude of R-PRP acceleration is roughly $3.5 \times 10^{-8}\ m/s^2$, which is close to the back of the envelope calculation value.

Similar to that of SRP, it is expected that R-PRP acceleration magnitudes will be function of β-angle. However, the acceleration magnitude should reduce with β-angle because for extreme β-angles, Magellan will see half of the planet illuminated by the Sun, resulting into low R-PRP acceleration magnitude.

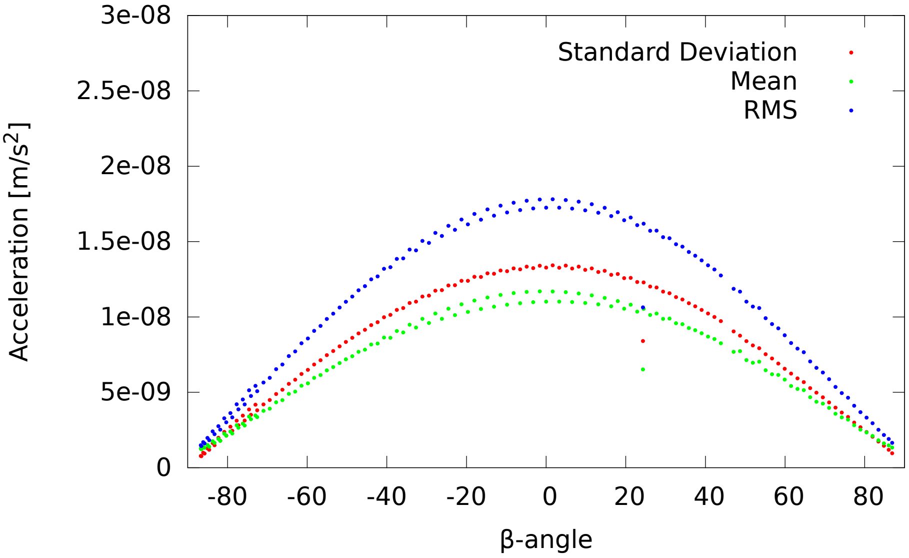

Figure 5.10: R-PRP acceleration magnitude statistics observed over $\beta = \pm 90^o$. The outliers near $\beta = 20^o$ correspond to day with poor orbit estimation, present in SPICE orbit. Furthermore, the periodic variations in statistical properties for lower β-angle values are due to the contributions of zero magnitudes pertaining to eclipse condition.

From Figure 5.10, the influence of β-angle can be observed on the modeled acceleration due to R-PRP. A high value of standard deviation of the acceleration magnitude for the days with $\beta = 0^o$ shows that the spacecraft experiences eclipses due to which the difference between maximum and minimum amplitudes of the acceleration is highest. Furthermore, the maximum mean value for day with $\beta = 0^o$ confirms that Magellan sees a fully illuminated Venus surface that contributes to acceleration due to R-PRP lies in the orbital plane of the spacecraft. Lastly, just as SRP, the periodic variations in daily statistical values of acceleration magnitudes, for low β-angles, pertain to eclipse conditions.

E-PRP Validation

The acceleration on a spacecraft due to E-PRP is given as (see Section 3.3 of Chapter 3):

$$\ddot{\mathbf{r}}_{E-PRP} = C_R \frac{A}{m} P_{R-ERP} \hat{\mathbf{r}}_{\oplus} \tag{5.6}$$

where,
P_{E-PRP} → emitted radiation pressure from the source $[N/m^2]$.

Similar to R-PRP, the emitted planetary radiation pressure at spacecraft location can be given as:

$$P_{E-PRP} = \frac{1\ AU}{|D_{\odot} - R_{\oplus}|^2} P_{\odot 1AU} \frac{A_{\oplus}\epsilon}{4\pi|\mathbf{r}|^2} \tag{5.7}$$

where,
$\epsilon = 1 - \alpha$ → planetary emissivity.

Again, using the values from Table 5.3, the radiation due to planetary emissivity is estimated as:

$$P_{E-PRP} = 4.56 \times 10^{-6} \left(\frac{1AU}{0.72\ AU}\right)^2 \times \frac{\pi \times 6051000^2 \times (1-0.76)}{4\pi \times 6351000^2} = 4.94 \times 10^{-7}\ N/m^2$$

and hence, the R-PRP acceleration is estimated as:

$$\ddot{\mathbf{r}}_{E-PRP} = 1.4 \times \frac{10.52}{2500} \times 4.94 \times 10^{-7} = 2.9 \times 10^{-9}\ m/s^2$$

Assuming that the Venusian surface radiates isotropically in infrared wavelengths, it is expected that the contribution of E-PRP will always have a near-constant magnitude, irrespective of spacecraft eclipse conditions and β-angle.

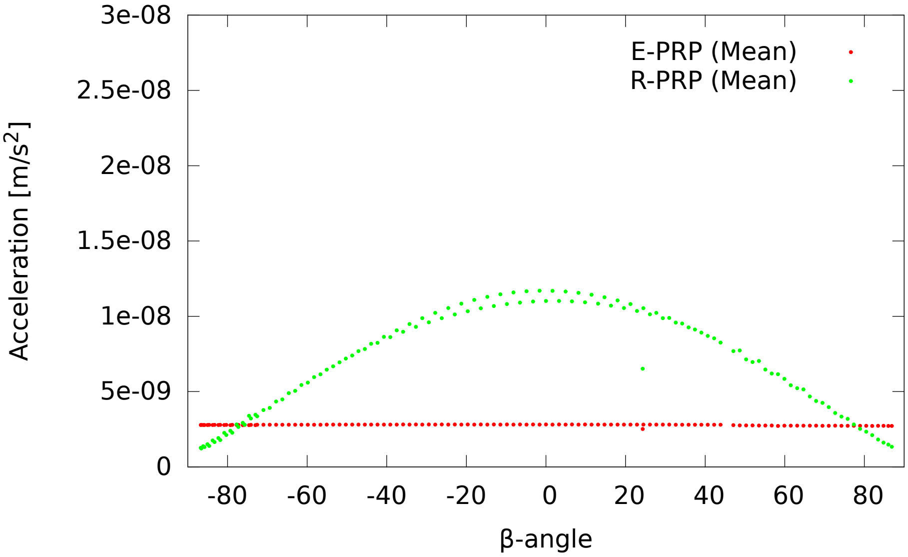

Figure 5.11: E-PRP and R-PRP acceleration magnitude compared as functions of β-angle. Note that the outlying data points correspond to days with poor SPICE orbits.

From Figure 5.11, it can be seen that the contribution of acceleration due to E-PRP is independent of β-angle and rather stays constant throughout, whereas for days when β-angle is close to zero, acceleration due to R-PRP dominates the net planetary radiation pressure acceleration, which can be almost 6 times than that of E-PRP. Furthermore, from Figure 5.12, a standard deviation, that is an order of magnitude less than the RMS of acceleration magnitude, confirms that E-PRP acceleration will not change with solar distance. Only the orbit characteristics of Magellan (i.e. its location with respect to the orbital plane and the eccentricity of the orbit) during gravity phase contributes to a change in E-PRP that is 10 times less than that of the acceleration magnitude itself. Nevertheless, the modeled E-PRP acceleration magnitude is close the back of the envelope calculation.

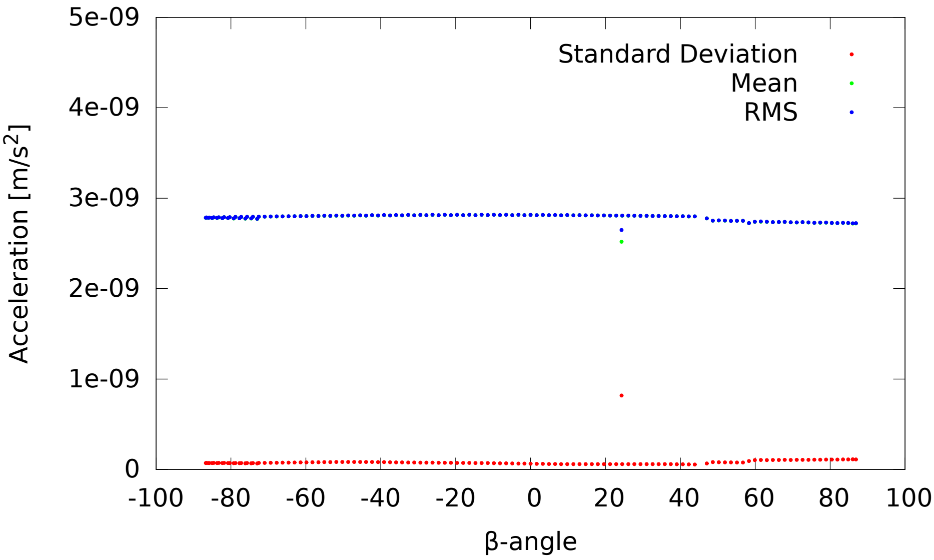

Figure 5.12: E-PRP acceleration magnitude statistics observed over $\beta = \pm 90^o$. The small variation towards the end of positive β values is due to the change in orbit characteristics, possibly due to maneuvers.

5.3.3. Validation Of Drag

The acceleration due to drag force, with a cannonball model can be modeled as:

$$\ddot{\mathbf{r}}_{Drag} = \frac{1}{2}\frac{A}{m}\rho_\infty V_{atm}^2 C_D \hat{\mathbf{u}} \tag{5.8}$$

where,
C_D → spacecraft drag coefficient [-],
A → spacecraft area $[m^2]$,
m → spacecraft mass $[kg]$,
ρ_∞ → free stream atmospheric density $[kg/m^3]$,
V_{atm} → Spacecraft velocity with respect to the atmosphere $[m/s]$,
$\hat{\mathbf{u}}$ → unit vector of incoming particles.

It is important to know that, beyond 150 km, the free-stream densities are function of altitudes and local solar time (see Section 3.1 of Chapter 3). Since Magellan's altitude varies between 400-170 km during gravity phase [6], the expected drag acceleration magnitudes shall be calculated for two extreme altitudes for one chosen Day 122 of 1994. In order to do this, density estimates and SZA at required altitudes and local solar time are obtained from VIRA while assuming a fixed $C_D = 1.25$. The input values are tabulated as in Table 5.4:

Variable	Value	Dimension
C_D	1.25	[-]
A	10.52	$[m^2]$
V_{atm}	7.26	$[km/s]$
$\rho_{203\ km}$	0.86×10^{-13}	$[kg/m^3]$
$\rho_{400\ km}$	0.13×10^{-14}	$[kg/m^3]$
M	2,500	$[kg]$
$SZA_{203\ km}$	158	$[deg]$
$SZA_{390\ km}$	15.53	$[deg]$

Table 5.4: Assumed values of variables. Here A is the circular cross-section area with radius 1.83 m and the average spacecraft velocity is assumed to be 7.26 km/s, based on the values observed during tests.

At 203 km the magnitude of acceleration due to drag is:

$$\ddot{\mathbf{r}}_{Drag} = \frac{1}{2} \times \frac{10.52}{2500} \times 0.86 \times 10^{-12} \times 7260^2 \times 1.25 = 1.2 \times 10^{-8}\ m/s^2$$

At 390 km the magnitude of acceleration due to drag is:

$$\ddot{\mathbf{r}}_{Drag} = \frac{1}{2} \times \frac{10.52}{2500} \times 0.13 \times 10^{-14} \times 7260^2 \times 1.25 = 1.6 \times 10^{-10}\ m/s^2$$

Thus, at highest altitude, the expected drag acceleration should be of the order $10^{-10}\ m/s^2$ or less, whereas at the lowest altitude the magnitude should be of the order $10^{-8}\ m/s^2$ or more (see Figure 5.13)

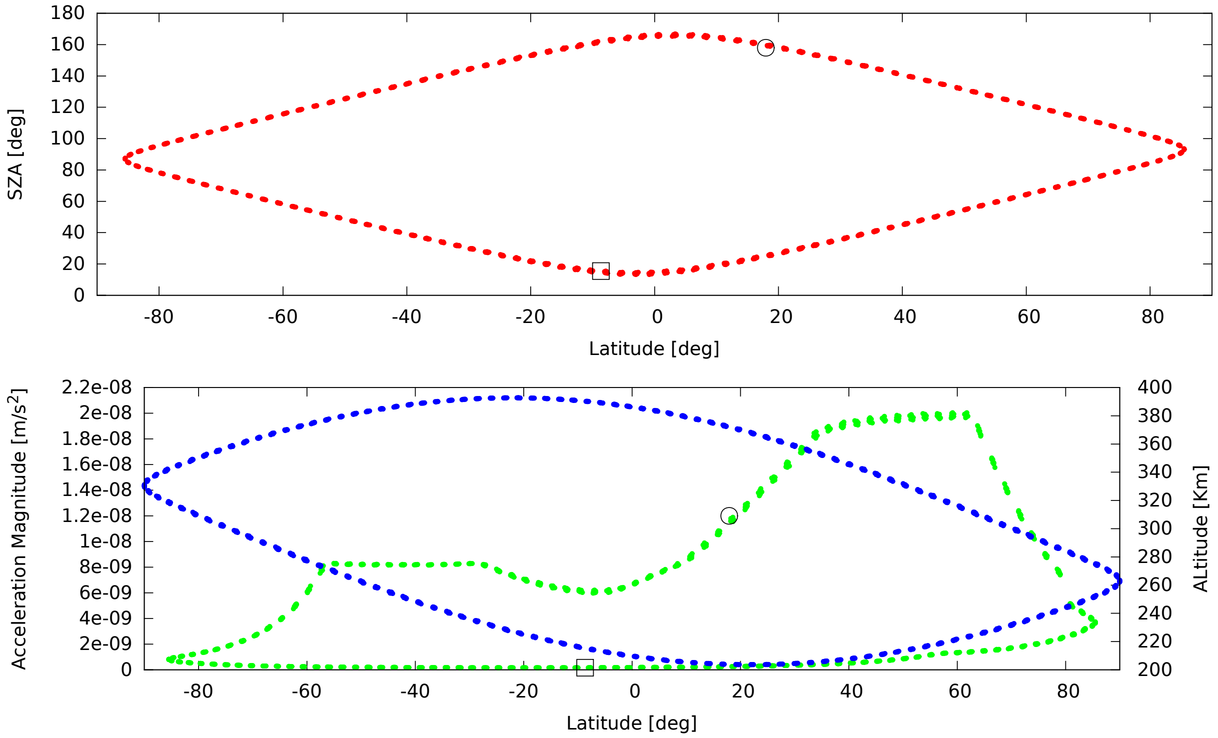

Figure 5.13: Top: Solar Zenith Angle (SZA) plotted against the latitudinal position of Magellan with respect to Venus. Bottom: Modeled drag acceleration magnitude (green) and altitude (blue) expressed as functions of latitude, observed on Day 122 of 1994. **Square:** Back of the envelope drag acceleration magnitude at 390 km altitude. **Circle:** Back of the envelope drag acceleration magnitude at 203 km altitude. The corresponding SZA values are marked in the top plot. Note that the plot is sampled for 100 data points.

From the above figure, it can be seen that drag acceleration is highest when Magellan is approximately at 220 km altitude and is lowest at 390 Km approximately. At first instance, one can expect that the drag acceleration should be highest at the lowest altitude, of approximately 200 km. However, it is important to recall that the density model for upper VIRA (150-250 km) is also a function of SZA and the densities given by VIRA decrease with increase in SZA (see Section 3.1 of Chapter 3). From the top figure of Figure 5.13, it can be seen that the SZA angle decreases as Magellan moves towards positive latitudes, due to which there is a small increase in the drag acceleration. However, the exponential decay of the drag acceleration magnitude, between $60^o - 80^o$ latitude is due to increase in altitude, as Magellan approaches towards apoapsis located at approximately -20^o latitude. Nevertheless, the modeled drag acceleration magnitudes are in good agreement with those of the back of the envelope calculation at two chosen altitudes.

5.3.4. Validation By Orbit Determination

In order to further support validation, an orbit determination test is performed for two days that have different orbit characteristics. Day 220 of 1993, which is at the start, and Day 122 of 1994, which is at the later stage, of the gravity phase are chosen. Furthermore, dynamic orbit model is assessed by setting up orbit parameterization with dynamics only, and no empirical or pseudo-stochastic parameters are estimated other than the six initial conditions. Impact of each surface force is observed by adding one force at a time and estimating initial conditions through LSQ-adjustment, and subsequently the orbits. The goal of this test is to observe a direct impact of dynamic models on the orbit determination which may give an insight of how effective are the modeled surface forces. For this purpose, SPICE orbits are used as observations, and for external orbit comparison. The orbit setups are same as Table 5.1. However, before proceeding with the results, let us get acquainted with the orbit profiles for Day 220 of 1993 and Day 122 of 1994.

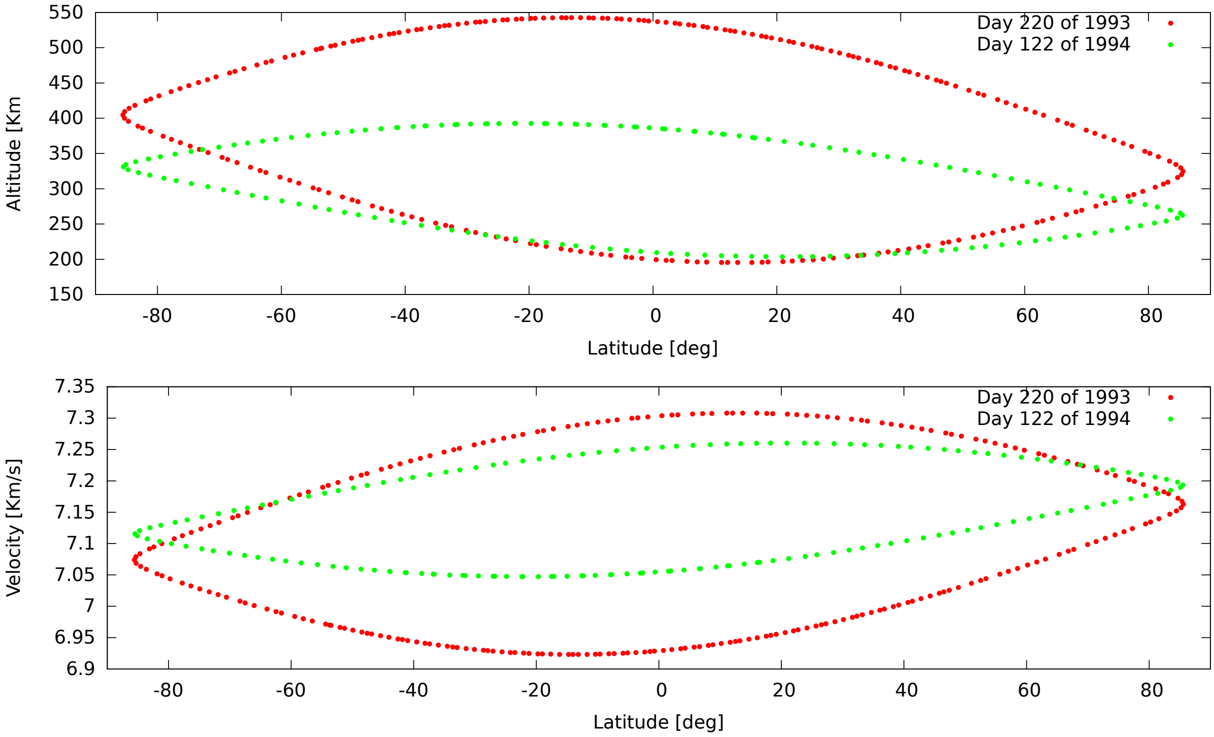

Figure 5.14: Orbit profile comparison between Day 220 of 1993 and Day 122 of 1994. The plot is sampled for every 100 data points.

From Figure 5.14, it can be clearly understood that the orbit corresponding to Day 122 of 1994 is more circular, with altitude at apoapsis lower than that for Day 220 of 1993. From orbit determination test, it was known that the eccentricity of the orbit was 0.027 for Day 220 of 1993, which is almost twice than that on Day 122 of 1994 ($e = 0.015$). Furthermore, by the principle of conservation of angular momentum, a low velocity at apoapsis will be complemented by high velocity at periapsis. In case of Day 220 of 1993, the velocity is roughly 3% more at periapsis than that observed on Day 122 of 1994, which suggests that the drag force will be higher for Day 220 of 1993 at periapsis. As a consequence, it is expected that the orbit solution will be more sensitive to drag acceleration on Day 220 of 1993 as compared to that on Day 122 of 1994. Now, with the orbit profile in mind, let us observe the impact of surface forces through orbit determination test.

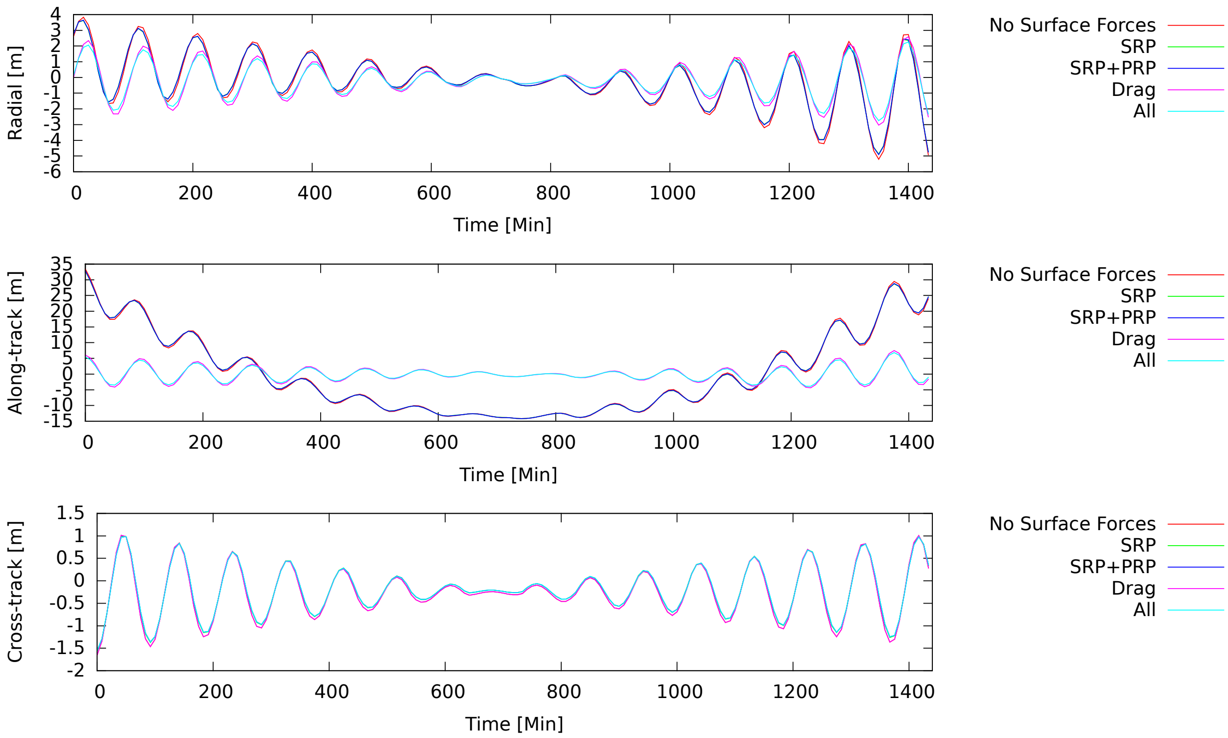

Figure 5.15: From top: Radial, along-track and cross-track position residuals with respect to SPICE orbit for Day 220 of 1993.

From Figure 5.15, it can be seen that the orbit comes close to SPICE (or improves), especially in the along-track direction, when surface forces are introduced into the dynamic orbit modeling. However, it is astonishing to see that the resulting improvements in the estimated orbit are not too significant for acceleration due to radiation forces. A comparison of acceleration magnitudes for each non-gravitational force, given in Figure 5.17, shows that the drag acceleration is almost an order of magnitude greater than SRP and PRP acceleration. As a consequence, it is expected that introduction of drag force model will have larger impact on the orbit for Day 220 of 1993. The statistics are shown for radial, along-track and cross-track direction in the tables below.

Statistical Properties	**No Surface Forces** $[m]$	**SRP** $[m]$	**SRP+PRP** $[m]$	**Drag** $[m]$	**All** $[m]$
Mean	-0.17	-0.17	-0.17	-0.17	-0.17
Standard Deviation	1.67	1.57	1.58	1.13	1.01
RMS	1.68	1.58	1.59	1.15	1.02
Maximum Value	3.84	3.67	3.69	2.63	2.31
Minimum Value	-5.90	-5.58	-5.61	-3.28	-2.99

Table 5.5: Statistics position residuals in radial direction, compared with SPICE orbit for Day 220 of 1993.

Statistical Properties	**No Surface Forces** $[m]$	**SRP** $[m]$	**SRP+PRP** $[m]$	**Drag** $[m]$	**All** $[m]$
Mean	0.00	0.00	0.00	0.00	0.00
Standard Deviation	12.62	12.57	12.59	2.33	2.08
RMS	12.62	12.57	12.59	2.33	2.08
Maximum Value	33.45	32.81	32.9	7.48	6.84
Minimum Value	-14.17	-14.17	-14.18	-4.43	-3.99

Table 5.6: Statistics position residuals in along-track direction, compared with SPICE orbit for Day 220 of 1993.

Statistical Properties	No Surface Forces $[m]$	SRP $[m]$	SRP+PRP $[m]$	Drag $[m]$	All $[m]$
Mean	-0.23	-0.19	-0.19	-0.23	-0.19
Standard Deviation	0.54	0.52	0.51	0.54	0.51
RMS	0.59	0.55	0.55	0.59	0.55
Maximum Value	1.05	1.03	1.02	1.05	1.02
Minimum Value	-1.65	-1.56	-1.55	-1.65	-1.55

Table 5.7: Statistics position residuals in cross-track direction, compared with SPICE orbit for Day 220 of 1993.

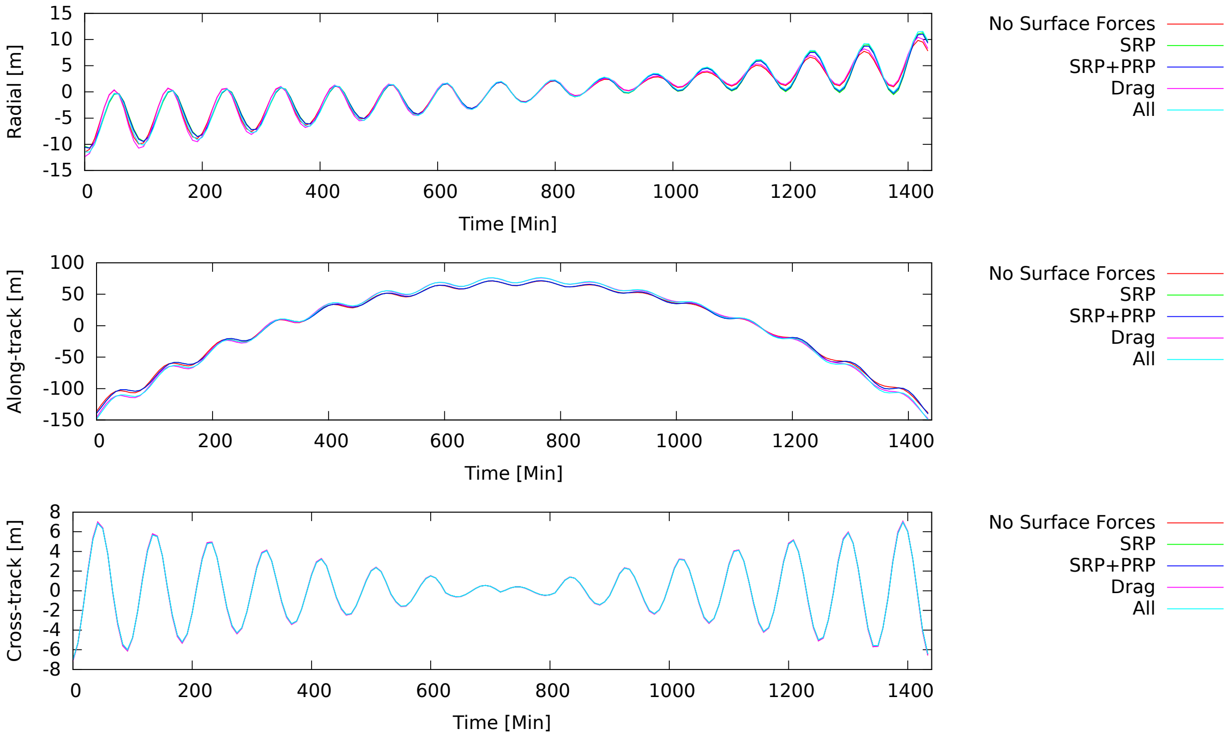

Figure 5.16: From top: Radial, along-track and cross-track position residuals with respect to SPICE orbit for Day 122 of 1994.

From Figure 5.16, it can be seen that there is no significant impact on the orbit when surface forces are introduced. However, the statistics shown in Tables 5.8, 5.9 and 5.10 show that orbits are slightly degrading with major degradation observed in along track direction of about 13 m in presence of all the surface forces. Now, comparing the magnitudes of surface accelerations for both the days, as seen in Figures 5.17 and 5.18 respectively, shows that the peak of drag acceleration is almost 6 times larger on Day 220 of 1993, than that observed on Day 122 of 1994. This observation can be further supported by the comparison of orbital profiles shown in Figure 5.14 and by comparing the atmospheric density profiles, given in Figure 5.19 experienced by Magellan for the chosen two days. A smaller periapsis altitude Day 220 of 1993 is a good explanation to why orbit is more sensitive to the presence of drag model on this day, compared to that on Day 122 of 1994. The SRP acceleration magnitude remains almost the same for both the days, with eclipses observed on Day 122 of 1994. Nevertheless, the observed statistics for Day 122 of 1994 show that there is no significant impact on the orbit when SRP and PRP accelerations are introduced.

Statistical Properties	No Surface Forces $[m]$	SRP $[m]$	SRP+PRP $[m]$	Drag $[m]$	All $[m]$
Mean	-0.10	-0.10	-0.10	-0.10	-0.10
Standard Deviation	4.07	4.22	4.19	4.35	4.46
RMS	4.07	4.22	4.19	4.35	4.46
Maximum Value	9.89	11.43	11.18	10.48	11.76
Minimum Value	-11.53	-10.75	-10.85	-12.40	-11.67

Table 5.8: Statistics position residuals in radial direction, compared with SPICE orbit for Day 122 of 1994.

Statistical Properties	No Surface Forces $[m]$	SRP $[m]$	SRP+PRP $[m]$	Drag $[m]$	All $[m]$
Mean	0.00	0.00	0.00	0.00	0.00
Standard Deviation	60.00	60.22	60.26	64.26	64.52
RMS	60.00	60.22	60.26	64.26	64.52
Maximum Value	71.17	71.55	71.58	76.20	76.54
Minimum Value	-142.66	-145.86	-145.51	-152.48	-155.34

Table 5.9: Statistics position residuals in along-track direction, compared with SPICE orbit for Day 122 of 1994.

Statistical Properties	No Surface Forces $[m]$	SRP $[m]$	SRP+PRP $[m]$	Drag $[m]$	All $[m]$
Mean	0.12	0.12	0.12	0.12	0.12
Standard Deviation	2.98	2.93	2.93	2.98	2.93
RMS	2.98	2.93	2.93	2.98	2.93
Maximum Value	7.07	6.97	6.97	7.07	6.97
Minimum Value	-7.15	-7.04	-7.04	-7.15	-7.04

Table 5.10: Statistics position residuals in cross-track direction, compared with SPICE orbit for Day 122 of 1994.

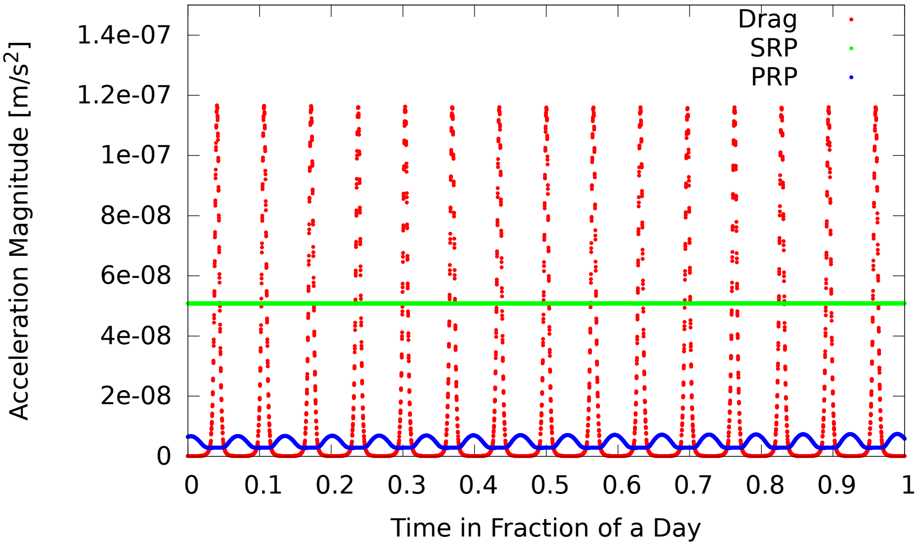

Figure 5.17: Non-gravitational acceleration profiles for each force, observed on Day 220 of 1993 (for which $\beta = 83^o$). The plot is sampled for every 100 data points obtained in RSW frame.

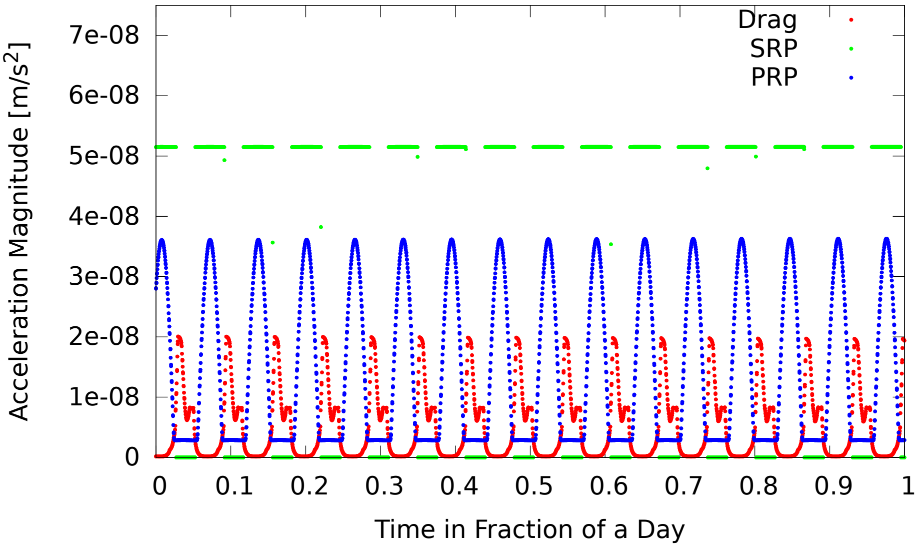

Figure 5.18: Non-gravitational acceleration profiles for each force, observed on Day 122 of 1994 (for which $\beta = 14^o$). The plot is sampled for every 100 data points obtained in RSW frame.

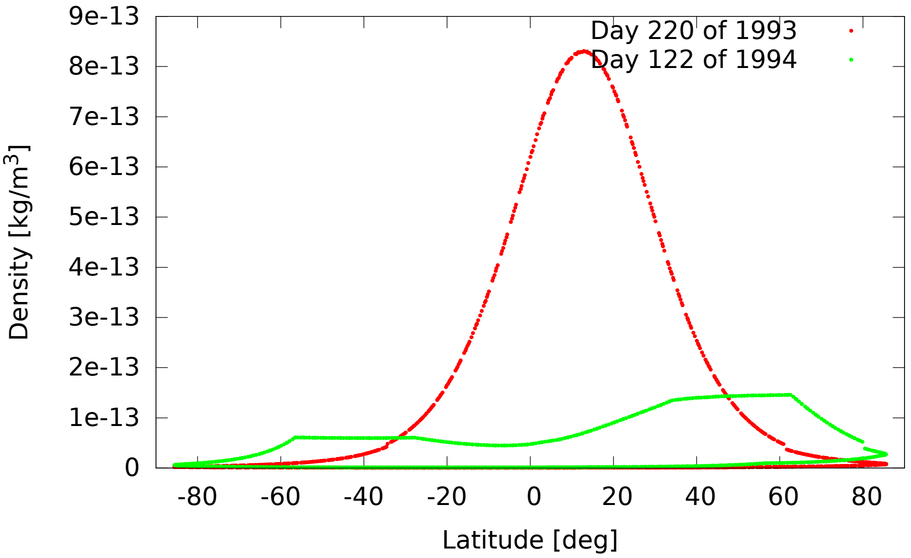

Figure 5.19: Density profile comparison between Day 220 of 1993 and Day 122 of 1994. The plot is sampled for every 50 data points.

Validation by orbit determination reveals conflicting results on impact of surface models for two days with different orbit profiles, wherein surface forces show either positive or negative impact on the orbit. Furthermore, it is also interesting to observe that the orbit determination with just gravity field results in a total RMS value of approximately 12.74 m for Day 220 of 1993, but results in an RMS value of 67 m for Day 122 of 1994. As a result, a question arises on the consistency of SPICE orbits. It is clear that for Day 122 of 1994, the SPICE orbit is dominated by aggressive empirical parameterization that was mainly done to either scale the weak surface forces or to deal with undocumented maneuvers. This implies that the orbit for this day could be highly reduced-dynamic. One thing that can be done in addition to this test is to artificially amplify all the surface forces and observe the impact on orbit for Day 122 of 1994. Despite of increasing the amplitude of the surface forces, if the orbit is still not sensitive, then it is a clear indication of aggressive parametrization in SPICE orbits. On the other hand, the surface force coefficients, namely C_D and C_R, could be significantly different for both the days, which my require estimation of scaling factors to tune the modeled acceleration. Nevertheless, the extent to which the SPICE orbits were aggressively parametrized is further discussed, with the orbit determination using additional parameters, in the next section.

5.3.5. Validation By Empirical & Pseudo-stochastic Parametrization

It has been discussed in Section 2.3 of Chapter 2 that a purely dynamic orbit model is not capable of providing best orbits, particularly due to imperfection in non-gravitational force models. To compensate for the defects arising due to non-gravitational force models, additional parameters are set up, that are estimated together with the initial conditions during LSQ-adjustment, to absorb the errors in orbit estimation. This process of setting up additional parameters, in parallel with the dynamic models, is known as Reduced-dynamic orbit modeling. Bernese GNSS v5.3 allows estimation of empirical parameters such as constant acceleration bias, 1-CPR, and scaling factors, and pseudo-stochastic parameters such as PCAs and pulses. In Section 2.3, it has been discussed that PCAs allow efficient modeling of non-gravitational forces and can closely mimic non-gravitational accelerations. However, parameters other than that pertaining to dynamic models, can also be used to asses the quality of implemented models for non-gravitational forces. In other words, when non-gravitational forces are represented by good dynamic models, the magnitude of additional acceleration parameters should reduce, which is a clear indication of improvement in the dynamic modeling of the orbit. To test this hypothesis, two days in the gravity phase of the mission are selected such that they represent different orbit characteristics. For this purpose, Day 220 of 1993, which is at the start of gravity phase, and Day 122 of 1994, which is in the middle of gravity phase, are selected. Furthermore, two types of orbit parametrization are done: 1) PCAs, acceleration bias, each in radial, along-track and cross-track direction, without surface forces; and 2) PCAs, acceleration bias, each in radial along-track and cross-track direction, with surface forces. Setup 1 is used as the reference base with a priori constraint of $10^{-5}\ mm/s^2$ (which is close to the expected magnitude of non-gravitational accelerations). For Setup 2, all the surface forces are switched on, while PCAs and biases still being active with identical constraints. The estimation of PCAs is done every 15 minutes for both the setups. The intent is to compare magnitudes of PCAs with and without surface forces. Note that acceleration biases are used to absorb the constant part (or mean) of the non-gravitational forces, while allowing PCAs to absorb time-varying parts (or standard deviation).

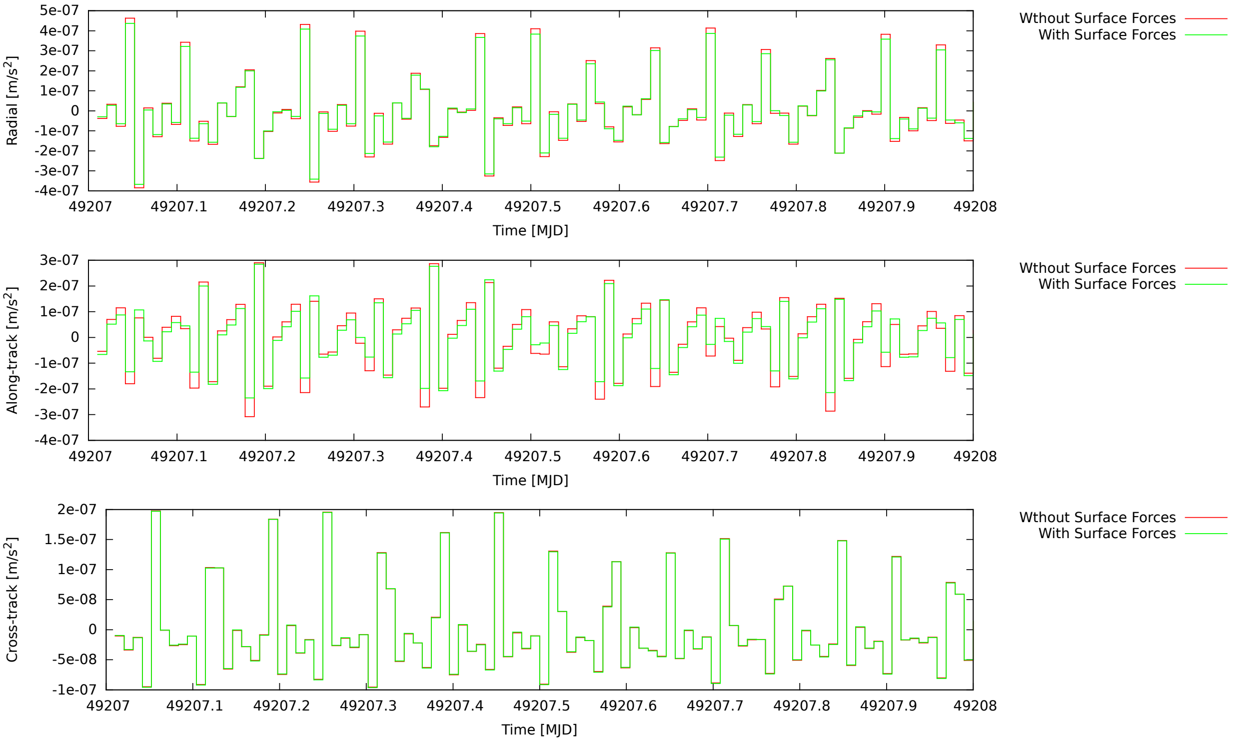

Figure 5.20: Comparison of PCAs without and with surface forces for Day 220 of 1993. Note that PCAs are estimated every 15 minutes (thus 96 PCAs for one day., i.e. 24 hours). Furthermore, the apriori constraints are $10^{-5}\ mm/s^2$

From Figure 5.20, it can be seen that a visible reduction in the amplitudes of PCAs is observed in along-track direction. This result is consistent with the improvements observed in the along-track direction as per the statistics shown in Table 5.6. This again confirms that presence of drag force in the orbit model has large impact on Day 220 of 1993, which in this case improves the orbit when compared with that of SPICE. Now, let us further quantify the above plot with statistics presented below for radial, along-track and cross-track direction.

Statistics	Without Surface Forces	With Surface Forces
Mean	-2.76E-14	1.22E-14
Standard Deviation	1.75E-07	1.66E-07
RMS	1.74E-07	1.65E-07
Maximum Value	0.46E-06	0.43E-06

Table 5.11: Statistics of estimated PCAs in radial direction for Day 220 of 1993.

Statistics	Without Surface Forces	With Surface Forces
Mean	-2.53E-14	9.98E-15
Standard Deviation	1.30E-07	1.14E-07
RMS	1.29E-07	1.14E-07
Maximum Value	0.29E-06	0.28E-06

Table 5.12: Statistics of estimated PCAs in along-track direction for Day 220 of 1993.

Statistics	Without Surface Forces	With Surface Forces
Mean	2.68E-14	1.76E-14
Standard Deviation	7.15E-08	7.14E-08
RMS	7.12E-08	7.10E-08
Maximum Value	0.19E-06	0.19E-06

Table 5.13: Statistics of estimated PCAs in cross-track direction for Day 220 of 1993.

Direction	Without Surface Forces	With Surface Forces
Radial $[m/s^2]$	0.725807E-06 ± 0.626724E-08	0.722188E-06 ± 0.599924E-08
Along-track $[m/s^2]$	-0.150219E-07 ± 0.626437E-08	-0.116189E-08 ± 0.599905E-08
Cross-track $[m/s^2]$	-0.312960E-06 ± 0.626494E-08	-0.261622E-06 ± 0.599705E-08

Table 5.14: Estimated values of acceleration biases and their formal errors for Day 122 of 1994.

The statistics presented in Tables 5.11, 5.12 and 5.13 show that the magnitude of estimated PCAs reduce in all directions, with largest reduction in along-track, when surface forces are present. Furthermore, the estimated biases and their formal errors also reduce in their magnitudes with surface forces active and this can be seen in Table 5.14. However, a question arises regarding the validity of this test. Of course, the empirical acceleration biases and pseudo-stochastic PCAs reduce in magnitude when surface forces are present for Day 220 of 1993. But the fact that there are no drastic reduction in additional parameters indicate that the parametrization done for this day is still absorbing some modeling defects. It is important to recall that the SPICE orbit is being used as observation data for this test. This means that the additional parameters are further absorbing missing parametrization that was done by Konopliv et al., [1999] and was not done for this test. This reveals the fact that the SPICE orbits contain additional empirical parameters that assist Konopliv et al., [1999] to obtain best orbits that give minimum Doppler residual. It is expected that the parametrization shall be different for different data arcs, which mainly depends on the behavior of Magellan's orbit for different days. Nevertheless, with this test, we can acknowledge that by using SPICE orbits as observations, we are only attempting to come closer to the orbits estimated by Konopliv et al., [1999], rather than seeking an absolute orbit improvement. To further reinforce the presence of empirical parametrization in SPICE orbits, a similar test is done for Day 122 of 1994.

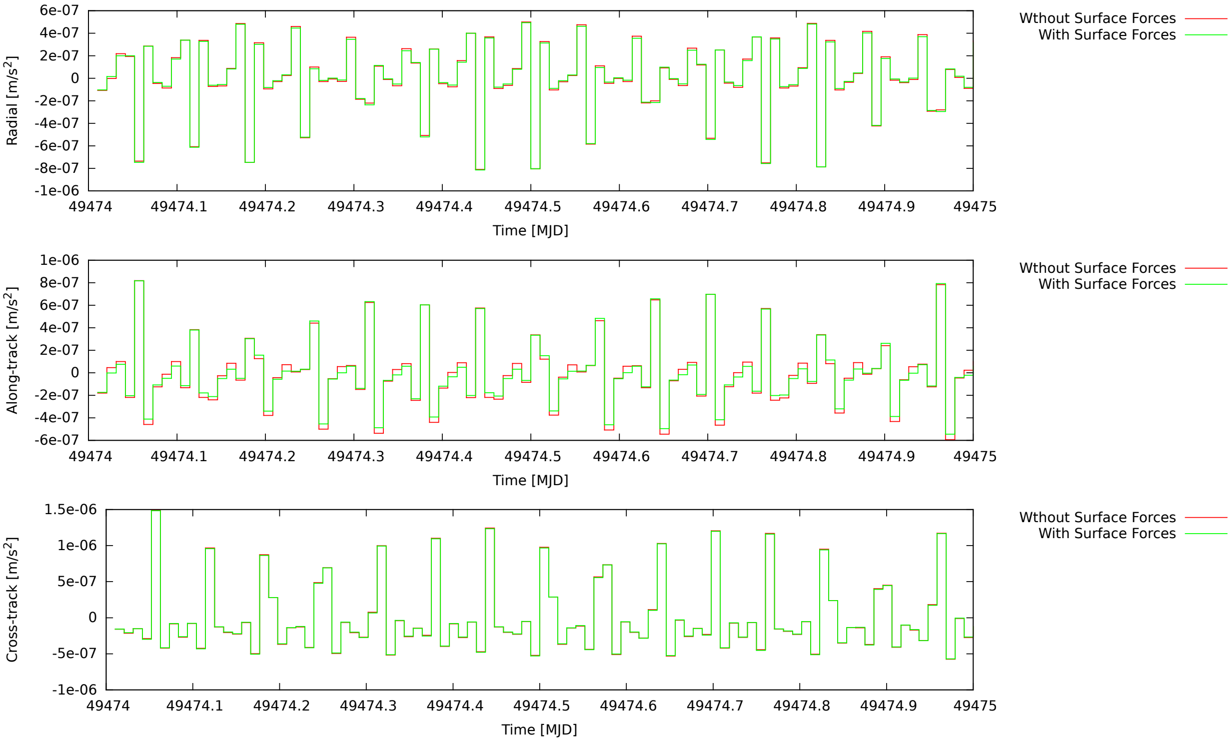

Figure 5.21: Comparison of PCAs without and with surface forces for Day 122 of 1994. Note that PCAs are estimated every 15 minutes (thus 96 PCAs for one day., i.e. 24 hours). Furthermore, the apriori constraints are $10^{-5}\ mm/s^2$

From Figure 5.21, it can be seen that amplitudes of PCAs are showing minute reduction, if not a significant one, in all directions. The plot is also supported by the statistics given in Tables 5.15, 5.16, 5.17. The large amplitudes of PCAs, despite the presence of surface forces, indicate a different orbit parametrization for Day 122 of 1994, when compared with that of Day 220 of 1993. This is expected because Day 122 corresponds to later stage of gravity phase that has more circularized orbit and a different value of β-angle than that of Day 220 of 1993 ($\beta = 14^o$ for Day 122 of 1994 and $\beta = 84^o$). As a result, the surface forces will exhibit different characteristics, that require different empirical parametrization to absorb mis-modeling errors. Lastly, from Table 5.18, note that the empirical acceleration biases slightly increase in their magnitude, indicating that the surface forces would degrade the orbit on Day 122 of 1994 if only dynamic orbit model was used (this has been observed in Section 5.3.4). This also supports the fact that SPICE orbit corresponding to Day 122 of 1994 could be heavily parametrized by Konopliv et al., [1999], that are reflected on the initial conditions too.

The purpose of validation with empirical and pseudo-stochastic parametrization was to asses the quality of surface force models by observing the amplitude/magnitude of empirical and pseudo-stochastic parameters. However, from Figures 5.20 and 5.21, it can be seen that the PCAs have amplitudes that are comparable to the expected magnitudes of surface forces even when the surface forces are active. Furthermore, the orbit is more sensitive to surface forces on Day 220 of 1994 than that on Day 122 of 1994 and this can be inferred by comparing the change in the amplitudes of PCAs when surface forces are introduced. This leads to two possible conclusions: 1) The implemented surface forces have modeling defects; 2) SPICE orbits are aggressively parametrized for some days. The first conclusion seems to be more plausible because the the spacecraft-specific physical properties namely mass, area, C_D, and C_R are assumed values and are kept fixed for both the days. This could be a source of inconsistency of the orbit solutions with that of SPICE and can be improved by estimation of scaling factors. Assuming that the second conclusion is true, if parameterization of SPICE orbits were used to co-estimate the state-of-the-art gravity field, then it is possible that the harmonic coefficients will contain artifacts due to aggressive parameterization and may always require similar empirical parametrization as that of SPICE, to deal with the artifacts.

Statistics	Without Surface Forces	With Surface Forces
Mean	3.20E-14	-1.57E-15
Standard Deviation	3.14E-07	3.11E-07
RMS	3.12E-07	3.10E-07
Maximum Value	0.50E-06	0.49E-06

Table 5.15: Statistics of estimated PCAs in radial direction for Day 122 of 1994.

Statistics	Without Surface Forces	With Surface Forces
Mean	-1.45E-15	-3.13E-14
Standard Deviation	2.92E-07	2.81E-07
RMS	2.90E-07	2.79E-07
Maximum Value	0.81E-06	0.81E-06

Table 5.16: Statistics of estimated PCAs in along-track direction for Day 122 of 1994.

Statistics	Without Surface Forces	With Surface Forces
Mean	-8.74E-14	-1.12E-13
Standard Deviation	4.91E-07	4.88E-07
RMS	4.89E-07	4.86E-07
Maximum Value	0.14E-05	0.14E-05

Table 5.17: Statistics of estimated PCAs in cross-track direction for Day 122 of 1994.

Direction	Without Surface Forces	With Surface Forces
Radial $[m/s^2]$	0.489676E-06 $\pm$ 0.193128E-07	0.491469E-06 $\pm$ 0.192211E-07
Along-track $[m/s^2]$	0.721159E-07 $\pm$ 0.193085E-07	0.767295E-07 $\pm$ 0.192127E-07
Cross-track $[m/s^2]$	0.147427E-06 $\pm$ 0.193053E-07	0.155243E-06 $\pm$ 0.192136E-07

Table 5.18: Estimated values of acceleration biases and their formal errors for Day 122 of 1994.

5.4. Conclusion

The goal of Verification was to confirm that the implemented surface forces show correct physical behavior. First, the modeling of drag acceleration was verified by observing the angle between Magellan's velocity vector with respect to atmosphere and the resultant drag acceleration vector, which should be exactly equal to 180^o. From Figure 5.1, it can be confirmed that drag acceleration has been implemented correctly since the required angle stays 180^o with negligible double-precision numerical errors. Second, implementation of SRP model was verified by choosing a Day 131 of 1994 for which β-angle is close to zero and then confirming that the angle between SRP acceleration vector and spacecraft-Sun unit vector is 180^o, again with negligible numerical errors (see Figure 5.2). Third, implementation of R-PRP model was verified to be correct by observing the angle between SRP acceleration vector and R-PRP acceleration vector for a day with β-angle is close to zero. If implemented correctly, the angle between R-PRP and SRP acceleration vectors should be exactly equal to 180^o at that instant for which Magellan is exactly between Sun and Venus (see Figure 5.5). Finally, implementation of E-PRP model was verified by observing the angle between Magellan's position from Venus' center and E-PRP acceleration vector. In ideal case, this angle should be zero because E-PRP is directed radially away from the center of the planet. However, from Figure 5.6, small non-zero values of this angle are observed. This is due to the fact that the entire planetary surface is divided into small grids of 1^o resolution for modeling E-PRP acceleration. As a result, it is possible that Magellan sees grids with different intensities, depending on its location over Venus, that contribute towards the net E-PRP acceleration, thereby resulting into small inclination of E-PRP acceleration with respect to spacecraft's position.

The goal of Validation was to make sure that the implemented models for surface forces give expected magnitudes of accelerations. For this purpose, back of the envelope calculations were done for each surface force and the results were compared with the acceleration magnitudes of the modeled forces. A comparison of back of the envelope calculations to that of the modeled acceleration magnitudes show a close agreement, with possible differences mainly due to approximated calculations in the former.

Back of the envelope validations were further supported by orbit determination. For this purpose, two days, namely Day 220 of 1993 and Day 122 of 1994, were chosen to represent different orbit profile and impact of surface forces on the orbits were analyzed. It was observed that for Day 220 of 1993, the orbit improves, with respect to SPICE, when all the surface forces are present, with drag acceleration producing highest impact on the orbit. On the other hand, activating surface forces tend to slightly degrade the orbit on Day 122 of 1994. The possible explanation would be the different orbit parametrization in SPICE, done by Konopliv et al., [1999], for the chosen days that are also reflected on the initial conditions for both the days. Less sensitivity of orbit, on Day 122 of 1994, to the surface forces is an indicator of initial conditions from SPICE orbits that were aggressively parametrized during their estimation. This was further supported by orbit determination with empirical and pseudo-stochastic parameters estimation. PCAs when estimated with SPICE positions as observations confirm the presence of additional empirical accelerations for both the days (see Figures 5.20 and 5.21), even when surface forces are active. However, this interpretation must be accepted with the fact that the surface forces, while being valid and correctly implemented, are still not perfect due to the errors in spacecraft physical specifications and non-dimensional force coefficients (C_D and C_R). It is expected that the estimation of estimating scaling factors, one for each surface force, should absorb these defects in the implemented models and give a clear picture of the modeling quality.

6

Results

This chapter presents the impact of non-gravitational forces on orbit determination of Magellan. However, before proceeding with obtaining relevant results, it was quickly realized through this project that processing Magellan's DSN data for orbit determination is not an easy task. The challenges faced in dealing with Magellan's tracking data and choosing parametrization for orbit determination are discussed in Section 6.1. Given that maneuver handling was not a part of this project, the rationale for selecting data arc for Doppler-based orbit determination is discussed in Section 6.2. Furthermore, model and attitude performance is discussed in Section 6.3. Finally, a synthesis of the results, central to the research objectives, is presented in Section 6.4

6.1. Challenges In Doppler Processing

In order to evaluate the performance of non-gravitational force modeling, the first step is to select an appropriate data arc that is free from maneuvers. However, tracking data processing for Magellan mission is not a straightforward task and makes the selection of good data arcs rather cumbersome. The present section highlights the challenges in dealing with Magellan Doppler tracking data processing.

6.1.1. Issues With Doppler Data Processing

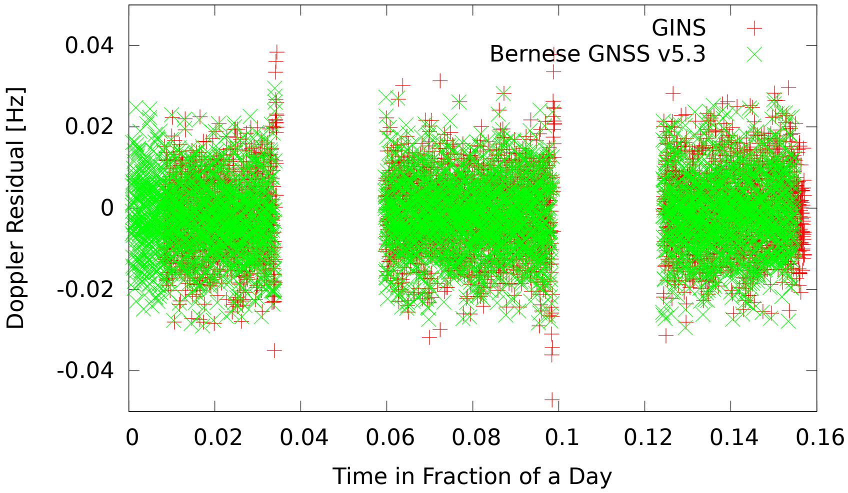

Figure 6.1: Doppler residuals of *Bernese GNSS v5.3* compared with those of *GINS* after fixing the bug, for Day 122 of 1994. The residuals are in excellent agreement with the results from CNES. For both the cases, state vectors of *Konopliv et al., [1999]* were used to compute the observation data.

The most time-consuming part of the project was Doppler processing. This first required fixing a bug in the Doppler routine that was associated with incorrect call of JPL planetary ephemeris leading to an error in estimation of spacecraft reception times (t_2) that introduced a bias in the computed values of Doppler observations. This bug was not visible in the previous uses of code and the process of fixing it was lengthy and required careful proof-reading of the Doppler routine, log-files, and validation tests. The Doppler residuals and one-way light-times were compared to that of CNES' GINS orbit determination software for Day 122 of 1994 (see Figure 6.1) for which SPICE positions were used to compute Doppler observations[1]. However, despite of fixing the bug associated with Doppler modeling, several unforeseeable issues/bottlenecks were encountered that could not be resolved due to limited time for the project. Nevertheless, it is essential to articulate all the open issues that are to be addressed in the future for achieving highest quality of scientific output.

The daily tracking is not uniform throughout the gravity phase of the mission, resulting in days with poor tracking (see Figure 6.2). Furthermore, from August 1993 to November 1993, there were some days with incorrect ramp frequencies rates due to truncation during recording, thereby leading to a discontinuity, of the order of 0.03 Hz (or 1 mm/s), in observations [6]. However, based on tests, ramp-associated discontinuities of even larger magnitudes have been observed for the Year 1994 (see Figure 6.3). While Konopliv et al., [1999] suggest a way-around by increasing or decreasing ramp rates by up to 0.000005 Hz/s for incorrect ramps (based on their empirical tests, [6]), this has not been verified and tested in this project and the data above certain threshold in the residual (up to 0.02 Hz) have been treated as outliers during preprocessing.

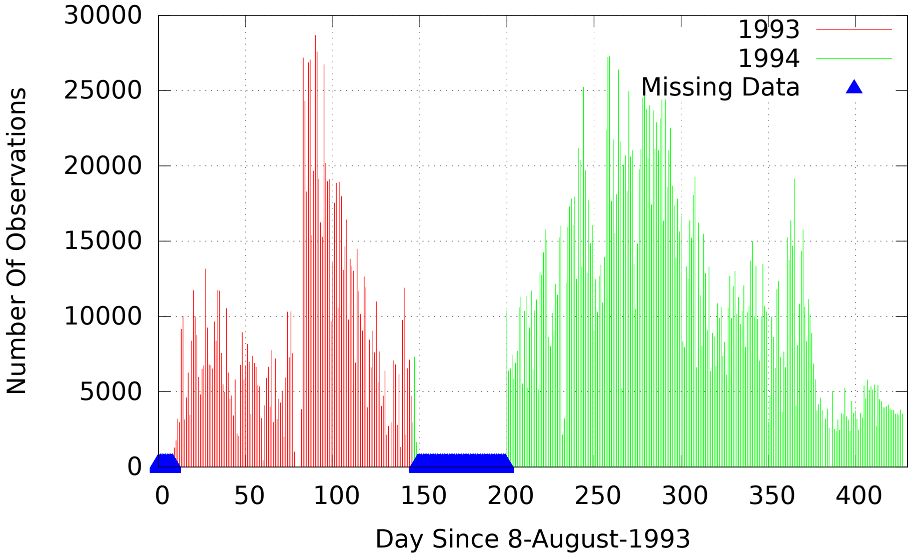

Figure 6.2: Number of observations per day since 8-August-1993 until the end of mission (13-October-1994).

---

[1] GINS-Geodesy by Simultaneous Digital Integration. CNES- Centre National d'études Spatiales.

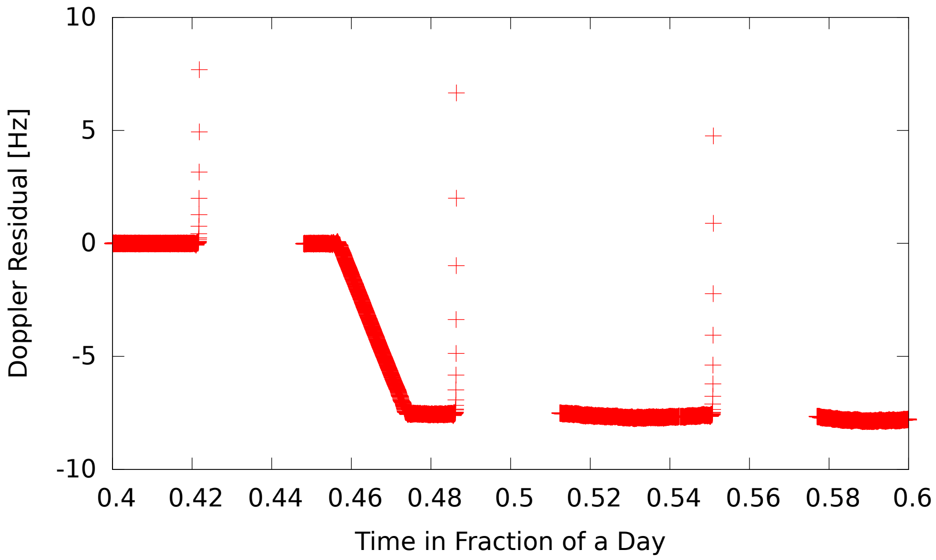

Figure 6.3: Discontinuity in the Doppler residuals due to ramp error, observed on Day 122 of 1994 (5-May-1994.) between 0.46 and 0.48 fraction of the day.

6.1.2. Missing Acceleration

It is important to highlight that the state vectors estimated by Konopliv et al.,[1999], from which the state-of-art gravity field is derived, were parametrized with empirical accelerations (up to the order $10^{-6}\ m/s^2$) to model acceleration due to hide maneuvers, momentum dumps and star calibration [4][2]. As a result, the initial conditions from the state vectors of Konopliv et al., [1999] are parametrized with empirical accelerations that, when left un-modeled, can result in poor orbit fit that is at least a km away from SPICE orbit (based on tests). In order to demonstrate the use of empirical accelerations in the SPICE orbits, an empirical constant acceleration bias, along each axis, is estimated on daily basis along with PCAs. The orbits are processed for an entire gravity phase (Cycle 5 & Cycle 6).

In order to estimate daily constant accelerations (or biases) with SPICE state vectors as observation , it is important to separate the constant part (or mean) of accelerations from the time-varying parts (or standard deviation). PCAs are used to model the temporal part of accelerations, while allowing the acceleration biases to absorb the constant part. The reader must note that the surface forces are not switched on because the models used in this project are definitely not identical to the ones used by Konopliv et al., [1999]. As a result, the biases may absorb the modeling defects from the implemented models that may alter the original magnitudes of biases, that are otherwise the direct values from the orbit parametrization done by Konopliv et al., [1999]. Thus, non-gravitational forces are switched off, while allowing empirical acceleration biases to absorb the constant parts and pseudo-stochastic PCAs to absorb the time-varying parts of accelerations that were modeled by Konopliv et al., [1999] for their orbit setup. Table 6.1 shows the orbit parametrization used with SPICE positions as observations.

---

[2] The history of hides are explicitly given in Venus Gravity Handbook, compiled by *Konopliv et al., [1996]*. Furthermore, AMD events, along with impulses, are available on PDS server (http://pds-geosciences.wustl.edu/mgn/mgn-v-rss-1-tracking-v1/mg_2601/AMD/).

Setup	Value	Comments (if any)
Geopotential Model	SHGJ180U	D/O 180
SPICE Position Samples	5 Seconds	-
Observation Weight	1	Each component is weighted equally.
Solid Tides (k_2)	0.295	File: TID_VEN.TPO
JPL Ephemeris	DE430	-
Third-body Perturbations	Yes	-
General Relativistic Corrections	Yes	Schwarzschild, Lense-Thirring, De Sitter
Surface Forces	None	-
Spacecraft Model	-	-
Atmosphere Model	-	-
Empirical Parameters	Acceleration Biases	Constant along RSW
Active Scaling Factor(s)	None	-
Spacecraft Mass [kg]	2,500	-
Integration Step Size	10 seconds	-
Pseudo-stochastic Parameter(s)	PCA	Estimated along RSW

Table 6.1: Orbit setup for estimating biases, along with PCAs estimated every 15 minutes in RSW direction with constrained apriori standard deviation value of 10^{-5} mm/s^2. No surface forces are active.

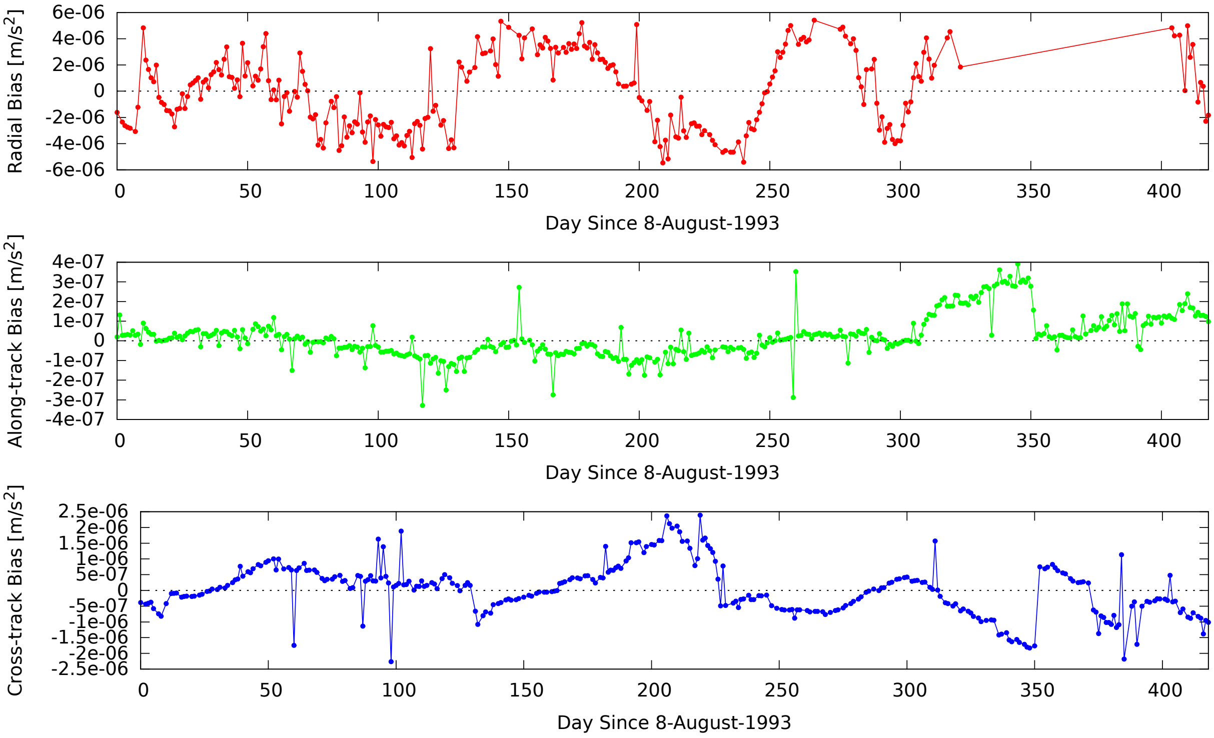

Figure 6.4: Daily estimated acceleration bias in radial (top), along-track (middle) and cross-track (bottom), shown for an entire gravity phase (Cycle 5 and Cycle 6), starting from 8-August-1993 to 13-October-1994. It is to be noted that the outlying data points corresponding to bad orbits or poor parameter estimation have been eliminated. As a result, there is a large gap in the radial bias plot between Day 300 and Day 400. To know the RMS error of the daily orbit fit, the reader can refer to Figure A.3 in Appendix.

Figure 6.4 shows the daily estimates of constant acceleration over an entire gravity phase of Magellan mission. It is interesting to see that the magnitude of constant accelerations in radial and cross-track directions are an order larger than those in the along-track direction and are on par with the magnitudes of non-gravitational accelerations (see Figures 5.17 and 5.18). A striking observation to be made is a periodic-pattern in the radial constant acceleration plot (top, red), with an approximate period equal to that of Venus' revolution around Sun, of 225 days. Further investigation indicates that the radial acceleration bias varies with β-angle, which also has the same period as that of Venus[3]. The evolution of β-angle is shown in Figure 6.5.

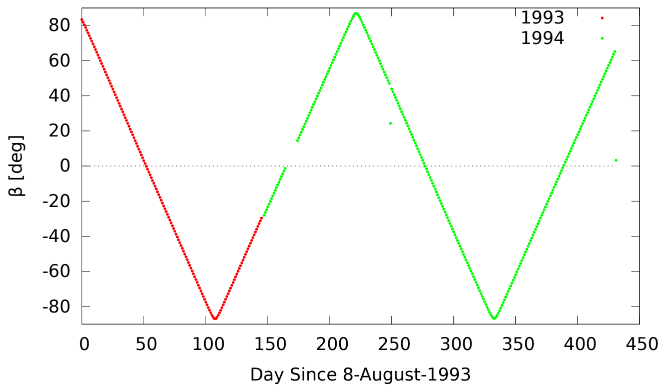

Figure 6.5: Daily value of β-angle over one full gravity phase from 8-August-1993 to 31-December-1993 (red), and from 1-January-1994 to 13-October-1994 (green). Note the outlying data points that corresponds to days with poor estimation of SPICE orbits.

In order to have a clear picture on the dependency of radial bias on β-angle, the daily values of estimated bias are fitted with quadratic Bézier curve for all directions in RSW frame (see [57] for more information on Bézier curve). From Figure 6.6, it can be seen that the fitted curve for radial bias has a maximum value at $\beta = 0^o$ and two minimum values at $\beta = -90^o$ and $\beta = 90^o$ respectively, thereby indicating a correlation with β-angle. On the other hand, there is no obvious dependency of along-track and cross-track biases on β-angle. This suggests that the empirical acceleration in radial direction is absorbing hide-induced change in radiation acceleration, perhaps SRP, in addition to maneuver-induced accelerations. However, intuitively speaking, it is understood that acceleration due to hide maneuver will be mostly along radial direction when $\beta = 0^o$, during which Sun, Venus and Magellan's orbit will be in the same plane, but it is rather unclear to correlate the dependency of radial bias for days when $\beta = \pm 90^o$[4]. It is also possible that the modeling of radiation pressure accelerations, originally done by Konopliv et al., [1999], contain modeling defects that are mostly dominated in the radial direction and were absorbed by the empirical parametrization done for SPICE orbits. On the other hand, a radial bias that is correlated with β-angle indicates that the gravity model itself contains a contribution from SRP mis-modeling for Magellan, that is ultimately being absorbed by the empirical acceleration bias. In their documentation of Venus Gravity Handbook, Konopliv et al., [1996] highlight that the SRP solutions (or estimation of C_R) for Magellan arcs are poorly determined during co-estimation of gravity field, which is an indication to be aware of the presence of errors due to radiation pressure mis-modeling in the gravity field itself[5]. Nevertheless, the empirical parametrization done by Konopliv et al., [1999] is not explored beyond this investigation, but it highlights the necessity to estimate empirical acceleration, together with initial conditions, if the changes in non-gravitational accelerations due to maneuvers/momentum dumps are to be modeled. The statistics of the estimated biases over an entire gravity phase are presented in Table 6.2.

---

[3] This is not generally true because the orbital plane is perturbed by third-body disturbances, cross-track maneuvers (if any), orbital precession. As a result, the β-angle will not be exactly the same after one period.

[4] During hide maneuver, the HGA looks at the Sun. As a result, the direct radiation pressure due to the illuminated HGA is to be countered with thrust, thereby leading to an acceleration in the radial direction..

[5] Venus Gravity Handbook was documented for development of 90 D/O gravity field. While *Konopliv et al., [1996]* provide an outlook to improve SRP modeling by modeling detailed orientation an reflectivity coefficients for Magellan, it is unclear if the state-of-the-art Venus gravity model of 180 D/O incorporates this improvement [6], [4].

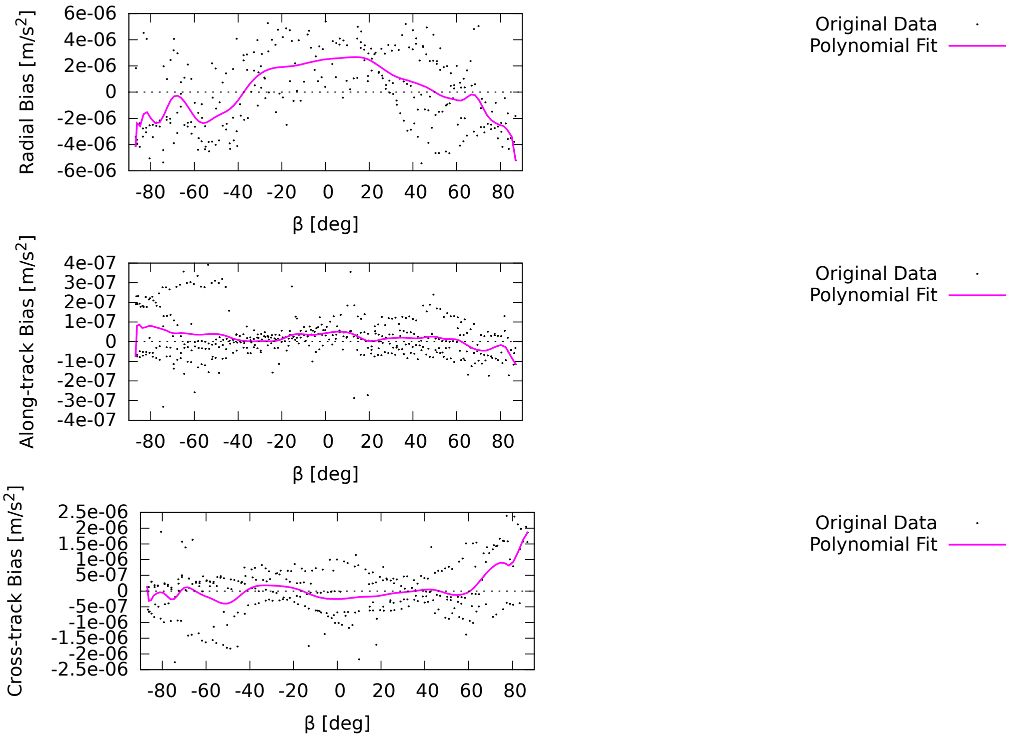

Figure 6.6: Polynomial fit of the daily estimated acceleration bias in radial, along-track and cross-track directions from SPICE orbits. The original data points are also shown in form of scatter data (black dots).

Statistics	**Radial** [m/s^2]	**Along-track** [m/s^2]	**Cross-track** [m/s^2]
Mean	1.85E-8	2.2E-8	2.85E-8
Standard Deviation	2.84E-6	1.06E-7	8.04E-7
RMS	2.83E-6	1.08E-7	8.05E-7

Table 6.2: Statistics of acceleration bias in radial, along-track and cross-track direction, observed over an entire gravity phase, starting from 8-August-1993 to 13-October-1994. The outlying data points are not included in estimation. As an approximation, data points that are four times the RMS are treated as outliers because they represent unreal values.

6.1.3. Issues With Empirical Parametrization

The use of scaling factors to asses (and improve) the quality of non-gravitational force modeling has been introduced in Section 4.4 Chapter 4. For the sake of quick recapitulation, scaling factors are empirical parameters that are estimated along with initial conditions to empirically scale non-gravitational accelerations to their expected magnitudes. Scaling factors are available in Bernese GNSS Software and produce excellent results for Earth-based POD. However, they have not been used in this project successfully. Initial orbit determination tests, with scaling factors active, show that for some days the estimated scale values are as high as 10^{14}, particularly for radiation pressures. The unrealistic values for some days are independent of the observation type (i.e. SPICE vectors or Doppler). However, further investigation was done by estimating one scaling factor for drag, SRP and PRP accelerations for an entire gravity phase of the mission, and assessing the formal errors in the scaling factors. It was observed that the formal errors are high for some days days with unrealistic scaling factor estimates, thereby suggesting a poor parameter estimation for those days.

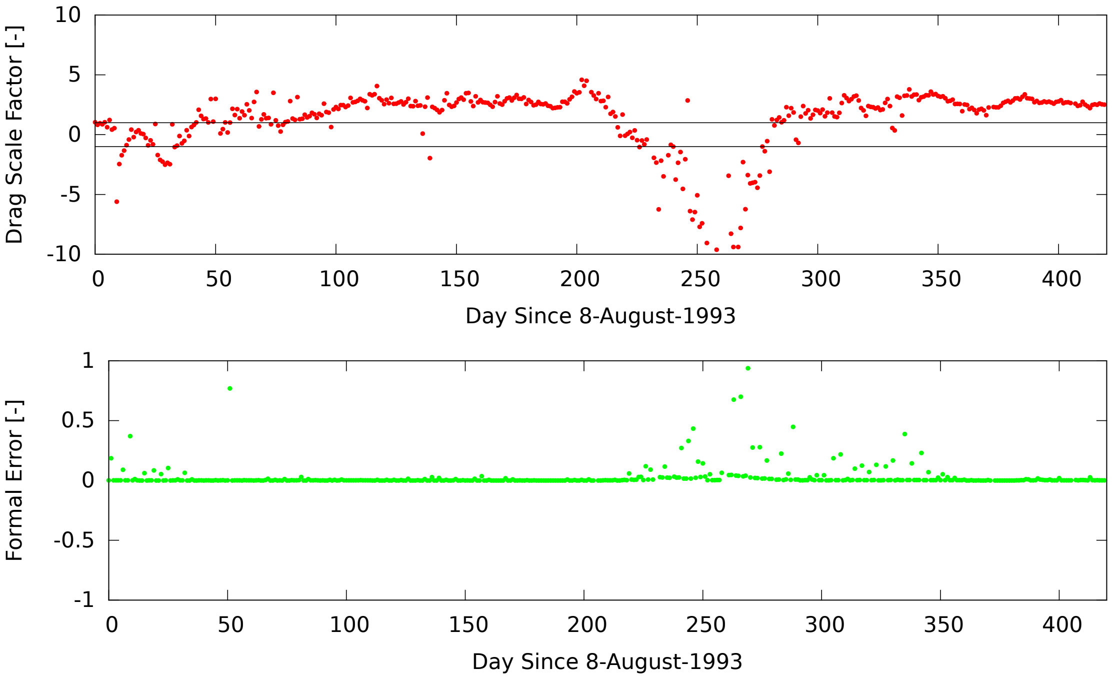

Figure 6.7: Estimated drag scaling factors (top) and their corresponding formal error (bottom) for an entire gravity phase (Cycle 5 and Cycle 6). Note that for some days the scaling factor values reach as high as 5000 and have not been included in the plot. The horizontal black lines in the top plot indicate 1 and -1 on the Y-axis.

Figure 6.7 shows the drag scaling factors values and their formal errors for an entire gravity cycle. The orbit setup consists of no other empirical and pseudo-stochastic parameters except drag scaling parameter, with cannonball as the spacecraft model. Furthermore, SPICE orbits are being used as observations. For most of the days, it can be observed that the formal errors of drag scaling factors are significantly less than the estimated values, thereby indicating a stable parameter estimation. However, if observed closely, one can see that for some days between 0-50 and 200-300, the scaling factors are negative. Intuitively, a negative scaling factor is not possible in case of correct implementation of drag model (see Section 5.2 of Chapter 5), yet the formal errors are lower than the estimated scaling parameter. While it is difficult to associate unrealistic scaling values to software bug, it is to be noted that the scaling parameters are being estimated freely in Bernese GNSS without providing apriori constraints. Nevertheless, it is not exactly understood why the values of drag scaling factors are negative for some days. Perhaps, the modeled accelerations due to non-gravitational forces are so weak for some days that scaling parameters cannot be estimated freely while expecting realistic values. Similar unrealistic high values have been observed while estimating acceleration biases for some other days that were different than that for drag scaling factors. To over come this, it is recommended that apriori constraints, in form of Bayesian estimation, should be applied to the empirical parameters to prevent them from absorbing defects more than they should. The values of empirical parameters, estimated by using SPICE orbits as observations, can be used to constrain the expected values of empirical parameters while using Doppler observations. However, it is expected that the required constraint will vary with data arc and one has to experiment with the chosen constraints by carefully observing the Doppler residual for each LSQ-adjustment and the formal errors in the parameter estimation. Just as the discussions in Sections 5.3.4 and 5.3.5, it is important to keep in mind that the observations used in this test are positions from SPICE orbits. As a result, it is likely that the parameters are compensating for the missing parametrization, that is required to be as close to SPICE orbits as possible. As an initial observation from Figure 6.7, it can be seen that the evolution of positive drag scaling factors fluctuates aggressively throughout the gravity phase. Assuming that this fluctuation was true while using Doppler observations, it is a clear indication that the quality of drag model is not sufficient. This is expected because the empirical VIRA densities and scale heights are not perfect and suit better with PVO mission, which was one of the contributers for developing VIRA [6] (see Section 1.4 of Chapter 1). To support this conclusion, it was found from the literature study that the densities for Magellan orbit determination are not well determined as those for PVO due to higher altitude and short orbit period [6]. To have a way around, Konopliv et al., [1999] constrain the density solutions for Magellan to $1 \times 10^{-12}\ gm/cm^3$ with 100% uncertainty [4], [6]. Nevertheless, drag scaling factor, when active and constrained to realistic values, can give an insight to the quality of the density model and it would be interesting to assess the empirical density model with estimated drag scaling factor, by initially using a simple cannonball setup and then extending the analysis with macro-model while using Doppler observations. Improvements in the atmospheric density solutions for Venus can definitely contribute towards better orbit determination and gravity recovery capability. In this section, only drag scaling factors have been discussed. Unrealistic values of scaling factors for radiation pressures (as high as 10^{14} with similarly high magnitudes for formal errors) were also observed and a discussion regarding this is not included in this report. Given the limitation with their unconstrained estimation, all the empirical parameters are disabled for now while processing Doppler observations as their unconstrained presence in the LSQ-adjustment degrade the estimated orbits, leading to a convergence far away from SPICE state vectors (up to 18 km, based on tests).

6.2. Doppler Data Arc Selection & Orbit Parametrization

It has been understood from Section 6.1 that processing Magellan Doppler tracking data is not a straightforward task due to lack of continuous tracking, ramp errors, and inability to use freely-estimated empirical parameters, particularly acceleration bias and scaling factors for Doppler processing. While a Reduced-dynamic Orbit modeling produces discernible results while using SPICE vectors as observations, a similar orbit parametrization is not suitable when Doppler observations are used as it leads to large unrealistic estimated values that either degrade the orbit or cause the program to crash. Furthermore, handling of spurious maneuvers like AMD and hides have not been investigated in this project and are necessary to deal with by using empirical parametrization and constraints while modeling Magellan's orbit around Venus. Nevertheless, tracking data for two consecutive days have been chosen by referring to SPICE orbits such that there are no suspicious maneuvers. This can be easily identified as large discontinuities in the SPICE positions, that are present after every 2-3 days (the average arc length of SPICE orbits varies from 2-3 days). It is a common practice to cut the data arc precisely before large propulsive maneuvers. Taking this into consideration, two consecutive days with no discontinuities in the SPICE positions have been chosen to analyze the impact of spacecraft model on modeled non-gravitational accelerations. Furthermore, the observations are given equal weight of 1. However, for future investigations, one can refer to Venus Gravity Handbook to know the strategy that was followed by Konopliv et al., [1996] to weight the observation data.

Regarding orbit parametrization, the estimated empirical acceleration biases have been used extensively, with SPICE vectors as observations, to get an insight into the orbit parametrization done by Konopliv et al., [1999]. Hence, it can now be understood that the errors due to imperfect non-gravitational force models and maneuvers can be absorbed by setting up additional parameters that are estimated during LSQ-adjustment along with the initial conditions. The Bernese GNSS Software allows an empirical estimation of acceleration biases, 1-CPR accelerations and a scaling factor for each non-gravitational acceleration. It is important to highlight that these empirical parameters are estimated freely and are not constrained apriori. As a result, they tend to absorb significant errors, leading to unrealistic values, while using Doppler observations. It has been observed through several tests that presence of unconstrained acceleration biases and scaling factors in the orbit parametrization degrade Doppler-based orbits, thereby resulting a converged orbit that is several kilometers away from SPICE orbits. As a result, no empirical parameters are included for estimation of Doppler-based orbits. Instead, the estimated value of drag scale factor, for each spacecraft model, with SPICE as observations is used for Doppler-based orbit determination. The orbit parametrization used for Doppler-based orbit determination is presented in table below:

Setup	Value	Comments (if any)
Geopotential Model	SHGJ180U	D/O 180
Solid Tides (k_2)	0.295	File: TID_VEN.TPO
JPL Ephemeris	DE430	-
Third-body Perturbations	Yes	-
General Relativistic Corrections	Yes	Schwarzschild, Lense-Thirring, De Sitter
Surface Forces	Drag, SRP, PRP	C_D used from SPICE test
Spacecraft Model 1	Cannon-ball	-
Spacecraft Model 2	Macro-model	Moving solar panels
Atmosphere Model	VIRA	Venus-GRAM Software package
Attitude	ATT_1 and ATT_2	See Section 4.4
Spacecraft Mass [kg]	2,500	-
Integration Step Size	10 seconds	Constant

Table 6.3: Orbit setup for Doppler-based orbit determination for a data arc containing Days 146, 147 of 1994.

6.3. Model & Attitude Performance

6.3.1. Drag

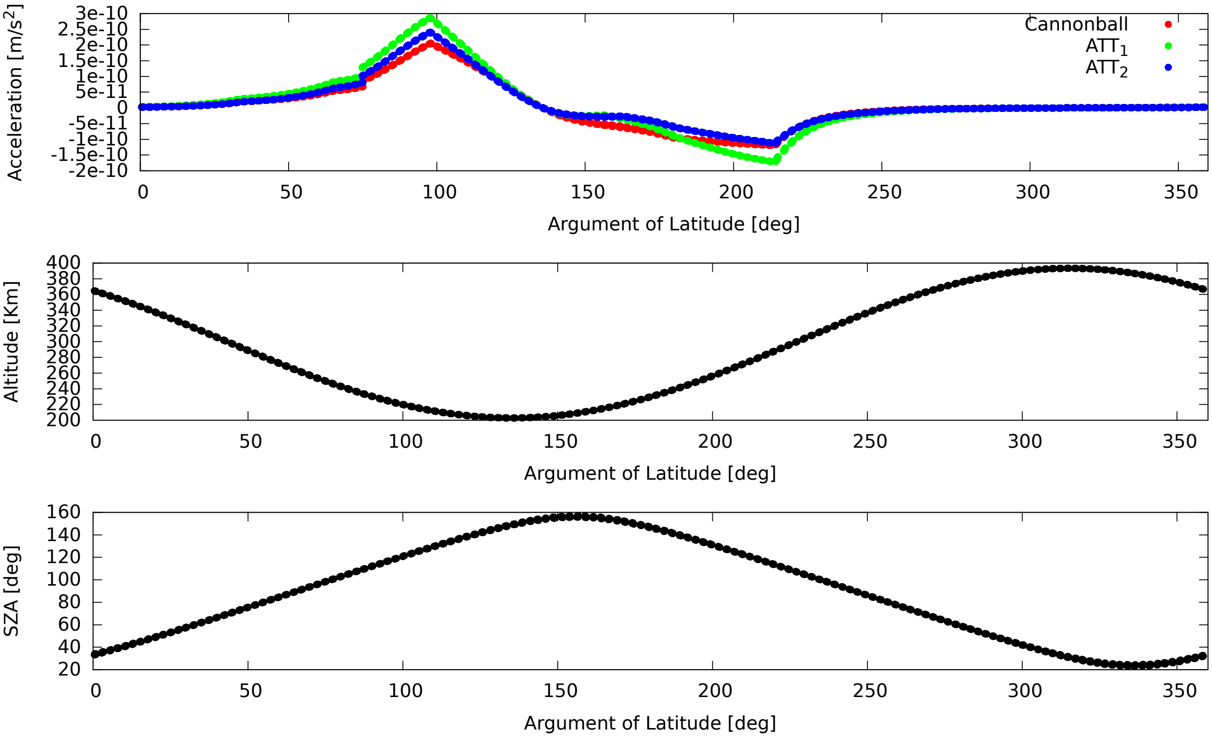

Figure 6.8: Top: Radial component of drag acceleration vector for different spacecraft model configuration. **Middle:** Altitude Evolution. **Bottom:** Solar Zenith Angle (SZA) evolution. The plot is sampled for 100 data points for Day 116 of 1994.

Speaking of the impact of spacecraft model and attitude configuration, it can be seen in Figure 6.8 that the shape of the drag acceleration curve is sensitive to the choice of spacecraft model and attitude in all directions. However, the along-track drag acceleration component is approximately 100 times larger than the radial component and 10,000 times larger than the cross-track component. As a result, it is expected that impact on estimated orbits will be largest due to the along-track component for a given choice of spacecraft model. From Figure 6.9, it can be observed that the changes in drag acceleration is highest for ATT_1 as compared to the other two spacecraft configurations as Magellan completes one orbit. This is because of the underlying attitude assumption that specifies an explicit alignment of solar panel axis along the velocity vector (see Section 4.4 of Chapter 4). Furthermore, the spacecraft area facing the direction of velocity vector changes as the solar panel is rotating slowly to directly look at Sun and is largest at the peak of drag acceleration at around 100^o argument of latitude. The peak of the along-track acceleration component is approximately 25% greater than that of the cannonball model (see Table 6.5 for statistics).

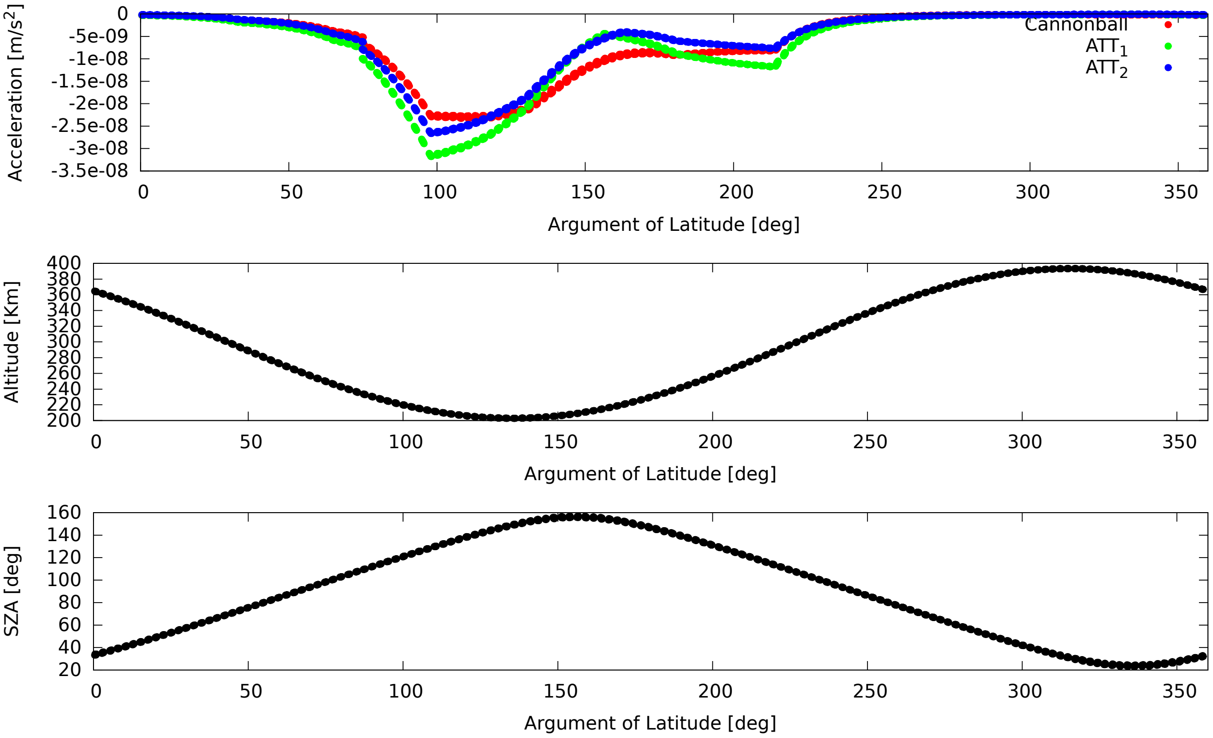

Figure 6.9: Top: Along-track component of drag acceleration vector for different spacecraft model configuration. **Middle:** Altitude Evolution. **Bottom:** Solar Zenith Angle (SZA) evolution. The plot is sampled for 100 data points for Day 116 of 1994.

From Figures 6.8, 6.9 and 6.10, it can be clearly seen that the drag acceleration on spacecraft is dominated by a component in the along-track direction. Furthermore, lower altitudes over $100^o - 200^o$ latitude indicate the periapsis region over which the magnitudes of drag acceleration is large. As per the discussion in Section 3.1 of Chapter 3, the atmospheric densities of upper atmosphere (beyond 150 km) are also dependent on the SZA (see Figure 3.5), in addition to the altitude. An interesting aspect to be mentioned about drag acceleration and SZA is that for Day 116, for which the plots are shown, larger SZA angles over the periapsis region are contributing to reduce the magnitude of acceleration due to drag force. However, a significantly smaller value of drag acceleration magnitude for higher altitudes, despite of lower SZA, indicate that the atmospheric densities , and consequently the drag acceleration magnitudes, are more sensitive to the change in spacecraft altitude than to the change in SZA. This observation is in agreement with that observed in Figure 3.5, where the atmospheric density as function of altitude is shown for various SZA angle values. A close look in the statistics presented in Table 6.4, 6.5, 6.6 reveals that the modeled drag acceleration magnitudes are larger for ATT_1 than the other spacecraft models. This is counter-intuitive since ATT_1 assumes a minimum drag configuration (see Section 4.4 of Chapter 4). The most likely cause of such discrepancy is the rotating solar panel, with assumed rotation rate of 0.00147 rad/s, that always looks towards the Sun which is at high SZA between argument of latitudes $50^o - 60^o$. As a result, it is likely that the vertically aligned solar panel is contributing to the modeled drag acceleration. Lastly, a discontinuity is observed in the acceleration curve at approximately 250 km altitude in all directions (75^o argument of latitude). This is due to the fact that Venus-GRAM uses VIRA model to estimate densities up to 250 km and a thermosphere model developed by MSFC, NASA to estimate densities for altitudes beyond 250 km [42].

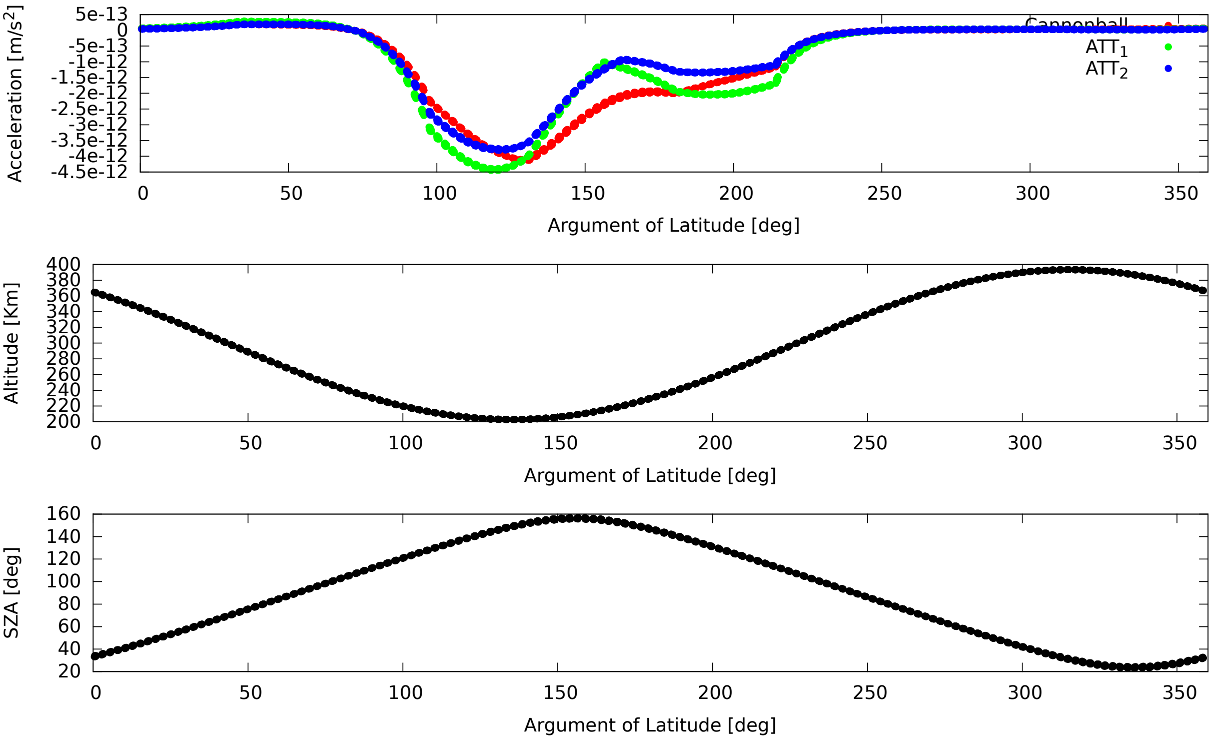

Figure 6.10: Top: Cross-track component of drag acceleration vector for different spacecraft model configuration. **Middle:** Altitude Evolution. **Bottom:** Solar Zenith Angle (SZA) evolution. The plot is sampled for 100 data points for Day 116 of 1994.

Statistics	**Cannonball** $[m/s^2]$	**Macro-model** (ATT_1) $[m/s^2]$	**Macro-model** (ATT_2) $[m/s^2]$
Mean	5.74E-12	1.27E-11	1.30E-11
Standard Deviation	6.98E-11	9.17E-11	7.16E-11
RMS	7.01E-11	9.26E-11	7.28E-11
Maximum Value	0.20E-09	0.28E-09	0.24E-09
Minimum Value	-0.11E-09	-0.17E-09	-0.11E-09

Table 6.4: Statistics of modeled drag acceleration in radial direction for different spacecraft model and attitude configuration.

Statistics	**Cannonball** $[m/s^2]$	**Macro-model** (ATT_1) $[m/s^2]$	**Macro-model** (ATT_2) $[m/s^2]$
Mean	-5.98E-09	-6.88E-09	-5.56E-09
Standard Deviation	7.32E-09	8.75E-09	7.43E-09
RMS	9.46E-09	1.11E-08	9.28E-09
Maximum Value	-0.16E-09	-0.77E-10	-0.85E-10
Minimum Value	-0.23E-07	-0.31E-07	-0.26E-07

Table 6.5: Statistics of modeled drag acceleration in along-track direction for different spacecraft model and attitude configuration.

Statistics	**Cannonball** [m/s^2]	**Macro-model** (ATT_1) [m/s^2]	**Macro-model** (ATT_2) [m/s^2]
Mean	-8.47E-13	-8.70E-13	-7.16E-13
Standard Deviation	1.30E-12	1.37E-12	1.16E-12
RMS	1.55E-12	1.62E-12	1.36E-12
Maximum Value	0.19E-12	0.28E-12	0.19E-12
Minimum Value	-0.41E-11	-0.44E-11	-0.38E-11

Table 6.6: Statistics of modeled drag acceleration in cross-track direction for different spacecraft model and attitude configuration.

6.3.2. SRP

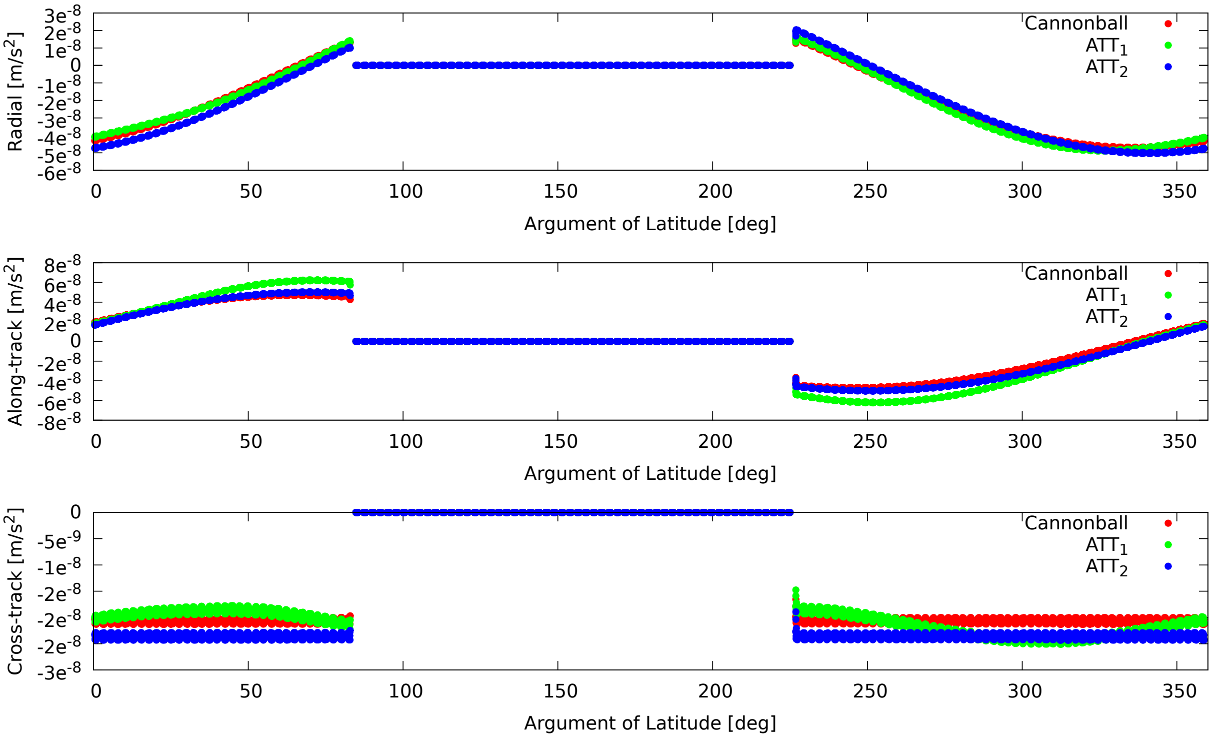

Figure 6.11: From Top: SRP acceleration profile in radial, along-track and cross-track direction for different spacecraft model choice. The data point with with $0\ m/s^2$ correspond to eclipse conditions. The plot is sampled for 100 data points for Day 116 of 1994.

Figure 6.11 shows SRP acceleration profile for different spacecraft and attitude configurations. It can be seen that radial and along-track components of SRP acceleration are almost twice the magnitude than for the cross track direction. However, it is interesting to see that the shape of the acceleration curve does not change significantly in all the directions for cannonball and macro-model with ATT_2. This is because the illuminated area of the spacecraft (approximately $10\ m^2$) is almost similar for cannonball and macro-model with ATT_2 since solar panels are always pointing towards Sun, which is the underlying assumption to formulate ATT_2 (see Section 4.4 of Chapter 4). For this data arc that includes Days 116-117, the β-angle varies from 25^o to 22^o. A question arises whether β-angle will have an influence on the SRP acceleration profile for different spacecraft and attitude configuration. As an educated guess, it can be expected that the acceleration profile for cannon-ball and ATT_2 will be more-or-less the same irrespective of β-angle because the illuminated area will not change. On the other hand, the modeled SRP acceleration profile shows visible variations with respect to other spacecraft model for ATT_1, particularly in along-track and cross-track directions. This is because of the varying area, due to movement of solar panels when trying to orient towards Sun, and realignment of $\pm X$ axis with respect to the velocity vector that also contributes towards the varying area.

6.3.3. PRP

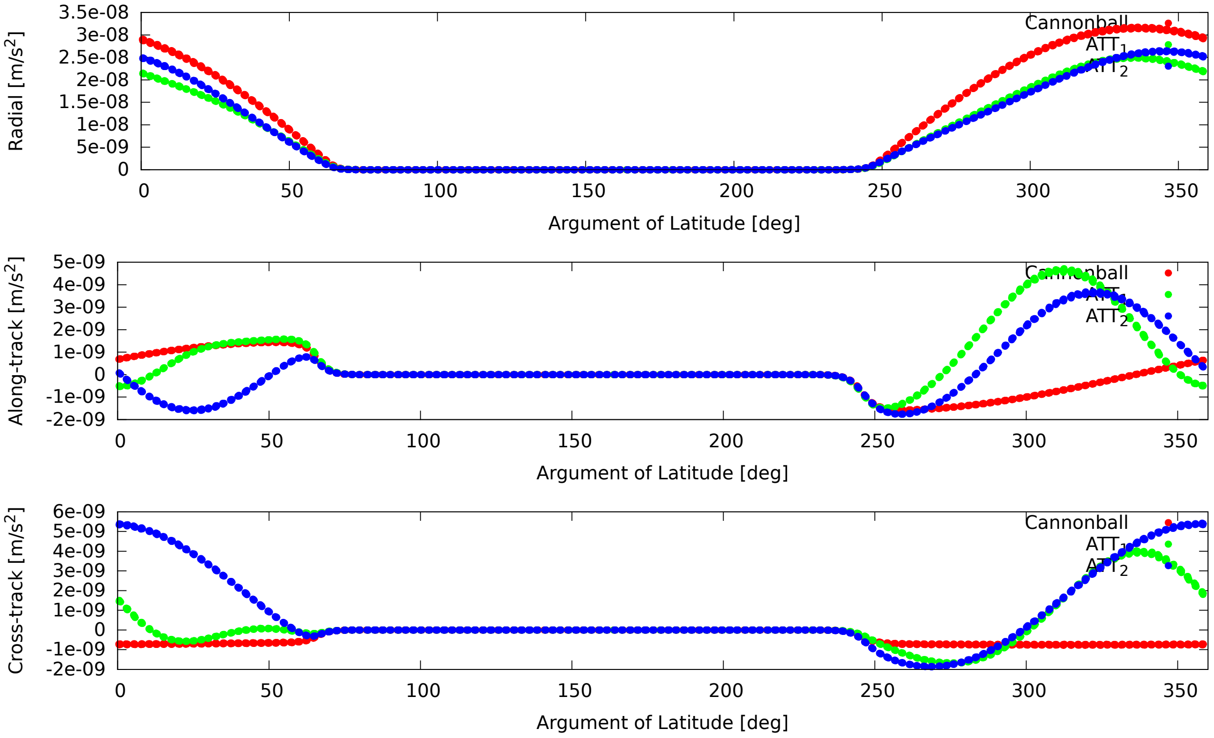

Figure 6.12: From Top: R-PRP acceleration profile in radial, along-track and cross-track direction for different spacecraft model choice. The data points with with $0\ m/s^2$ correspond to eclipse conditions. The plot is sampled for 100 data points for Day 116 of 1994.

From Figure 6.12, it can be seen that the R-PRP acceleration is dominated by the radial component, which is at approximately an order of magnitude larger than the other two components. Furthermore, the obvious similarity of the acceleration curve is visible in the radial direction for cannonball and macro-model with ATT_1. On the other hand, the difference in the acceleration curves are larger in along-track and cross-track direction, for a given spacecraft model and attitude configuration. Since along-track and cross-track components are smaller in magnitudes than that of the radial component, it is expected that this variation in the modeled acceleration, with spacecraft model, will not have a significant effect on the estimated orbit. Furthermore, if observed closely, the peak value of R-PRP acceleration in the radial direction with ATT_1 is approximately 30% smaller than that for cannonball. This is mainly due to the fact that macro-model with ATT_1 is aligning the solar panel with the velocity vector (i.e. rotation about Y-axis), thereby shadowing the otherwise illuminated plates.

Speaking of impact of spacecraft model on E-PRP acceleration profile, it can be seen in Figure 6.13 that cannonball model is generating an acceleration that is only in the radial direction. Furthermore, the shape of E-PRP acceleration curve remains almost constant and any sinusoid-like variation is mainly due to Magellan's orbit profile. On the other hand, ATT_1 and ATT_2 show visible changes in the acceleration curve and have non-zero acceleration magnitudes in along-track and cross-track direction. Note that the variations in E-PRP acceleration for ATT_2 are periodic and exhibit smooth sinusoidal evolution. This is mainly because of the perpendicular alignment of solar panel axis ($\pm X$) with the Sun, that causes a periodic variation in the panel area illuminated by E-PRP. On the other hand ATT_1 leads to abrupt variations which is mainly due to interaction between the alignment of $\pm X$-axis with the velocity vector and rotation of solar panel to look at the Sun, thereby leading to abrupt changes in illuminated panel area.

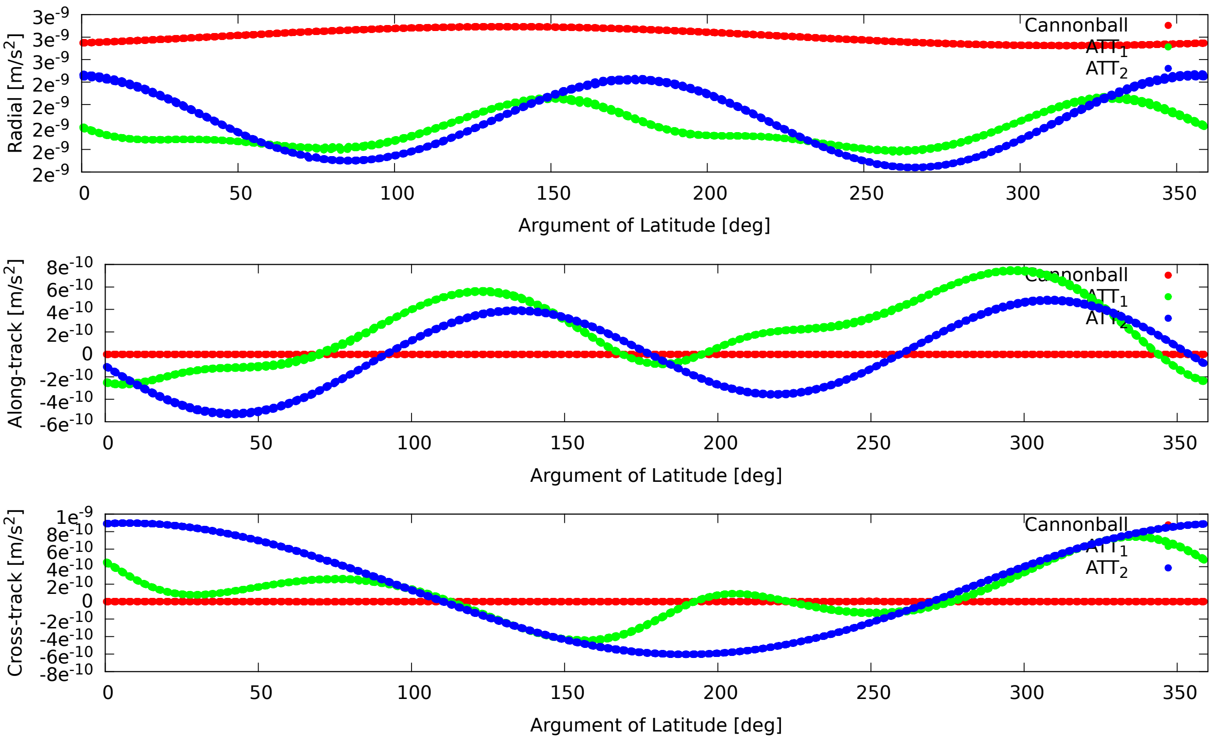

Figure 6.13: From Top: E-PRP acceleration profile in radial, along-track and cross-track direction for different spacecraft model choice. The plot is sampled for 100 data points for Day 116 of 1994.

6.3.4. Analysis By Empirical & Pseudo-stochastic Parametrization With SPICE

Now we know that the shapes of modeled accelerations due to surface forces are sensitive to the choice of spacecraft model and attitude assumption. In this section, the results of further investigations with empirical and pseudo-stochastic parametrization are presented. Impact of spacecraft model and attitude assumption was analyzed by conducting orbit determination tests with one-month SPICE orbits (of 24 hour arc length) as observations. The empirical parametrization is similar to that discussed in Section 5.3.5 of Chapter 5, and an orbit and parameter estimation test has been done over a period of 30 days, starting from 8-August-1993. However, before proceeding with discussion of the results, the reader has to assume that SPICE orbits represent the absolute truth about Magellan's orbit (even if this is not generally true). With this assumption in mind, the reader also has to consider the fact that SPICE positions have discontinuities that appear for every 2-3 days for which the estimated empirical parameters are unrealistic with large formal errors. Those days with sudden discontinuities are identified as the days with large RMS differences in radial. along-track and cross-track directions, and are omitted from supporting the scientific analysis (see Section A.5 of Appendix for RMS of the orbit fit using PCAs and biases only).

The comparison of estimated biases for spacecraft model and attitude assumptions in Figure 6.14 shows a shift along +Y-axis particularly in along-track (by a factor of 1.13) and cross-track direction (by a factor of 1.19). Moreover, a constant positive shift occurs for all the days when surface forces are introduced in the orbit modeling. This is mainly due to the assumed values of C_D and C_R that cause the mean of the modeled acceleration in along-track and cross-track to shift along Y-axis that is absorbed by the acceleration bias in a given direction. In addition to the non-dimensional coefficients, the assumed values of spacecraft mass and its area also contribute to this constant shift along Y-axis, if assumed incorrectly. It is interesting to see that the estimated biases do not appear to be as sensitive to the choice of spacecraft model and attitude configuration as to the switching on th surface forces. This indicates that the choice of spacecraft model and attitude configuration do not create an obvious shift in the mean of the modeled surface forces. In this case, a positive shift (or increment) in the along-track acceleration bias indicates poor assumption of C_D, spacecraft mass or its area that leads to (constant) errors in the modeled drag acceleration. In a similar sense, a constant positive shift in radial and cross-track direction, along which the radiation forces are dominant, indicate a poor assumption of C_R, mass and area of the spacecraft. Ideally, if the implemented surface forces were perfect (or identical to that of SPICE orbits), then the amplitude of biases would be zero in all directions which is an indication that the dynamic models are fully-able to represent Magellan's motion in its orbit. Nevertheless, estimation of acceleration biases give an insight into the accuracy of the assumed physical properties of the spacecraft and one can adjust their values such that the magnitude of acceleration biases reduce in all directions.

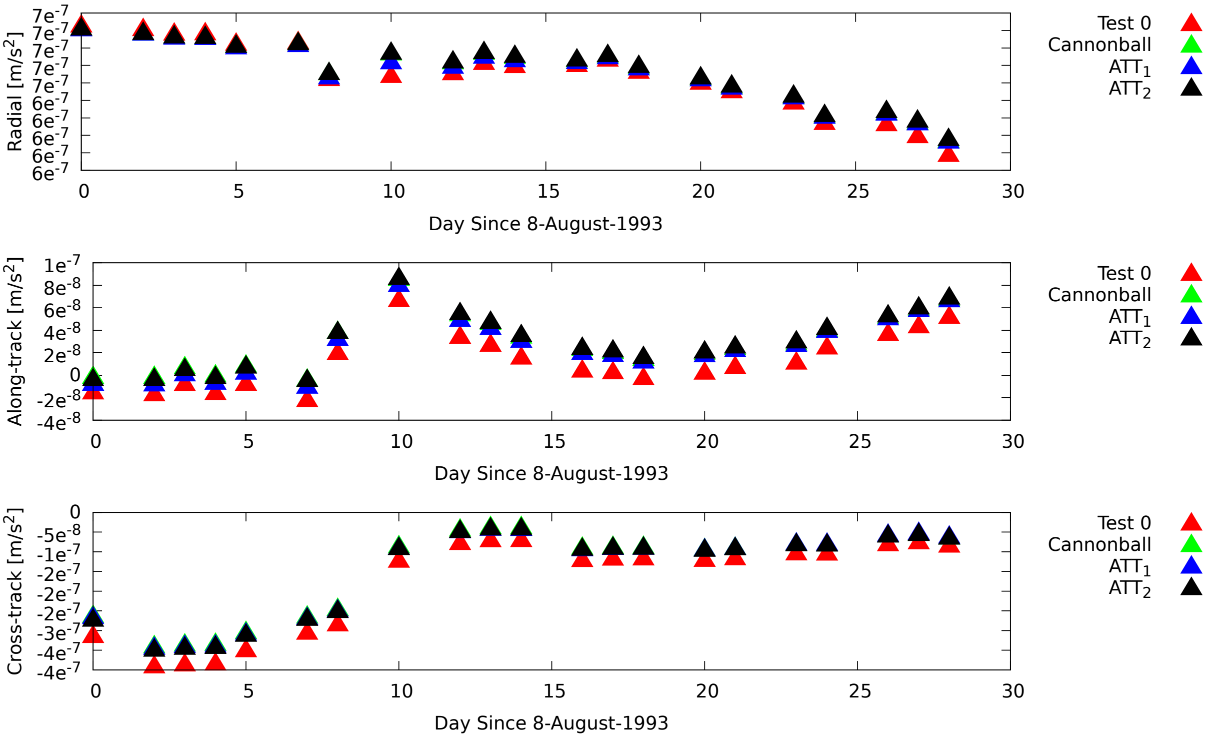

Figure 6.14: From Top: Comparison of the daily estimated biases for spacecraft model and attitude configuration in radial, along-track and cross-track direction for one month. Note that Test 0 is parametrized with PCAs and acceleration biases without surface forces.

In Section 5.3.5 of Chapter 5, PCAs have been used to asses the quality of non-gravitational models. For the sake of quick recap, the amplitude of PCAs reduce with the improvement in surface force models. The tests discussed in this section use PCAs to assess the sensitivity of the modeled acceleration to the choice of spacecraft model and attitude assumption. Figure 6.15 shows the standard deviation observed in the daily statistics of estimated PCAs. It can be seen that the standard deviation reduce in all directions, with maximum reduction (of up to 40%) in cross-track direction. Interestingly, it can be seen that the amplitude of PCAs do not change significantly in the radial direction in all the cases. This indicates that the orbit is not sensitive to surface forces in radial direction and any error in the modeled accelerations will not have a significant impact on the estimated positions in the radial direction. Just as expected, the choice of spacecraft model and attitude assumption has no significant impact in all directions as compared to the introduction of surface forces in the orbit model. A similar inference can be derived for the comparison of daily RMS values of the estimated PCAs, shown in Figure 6.16.

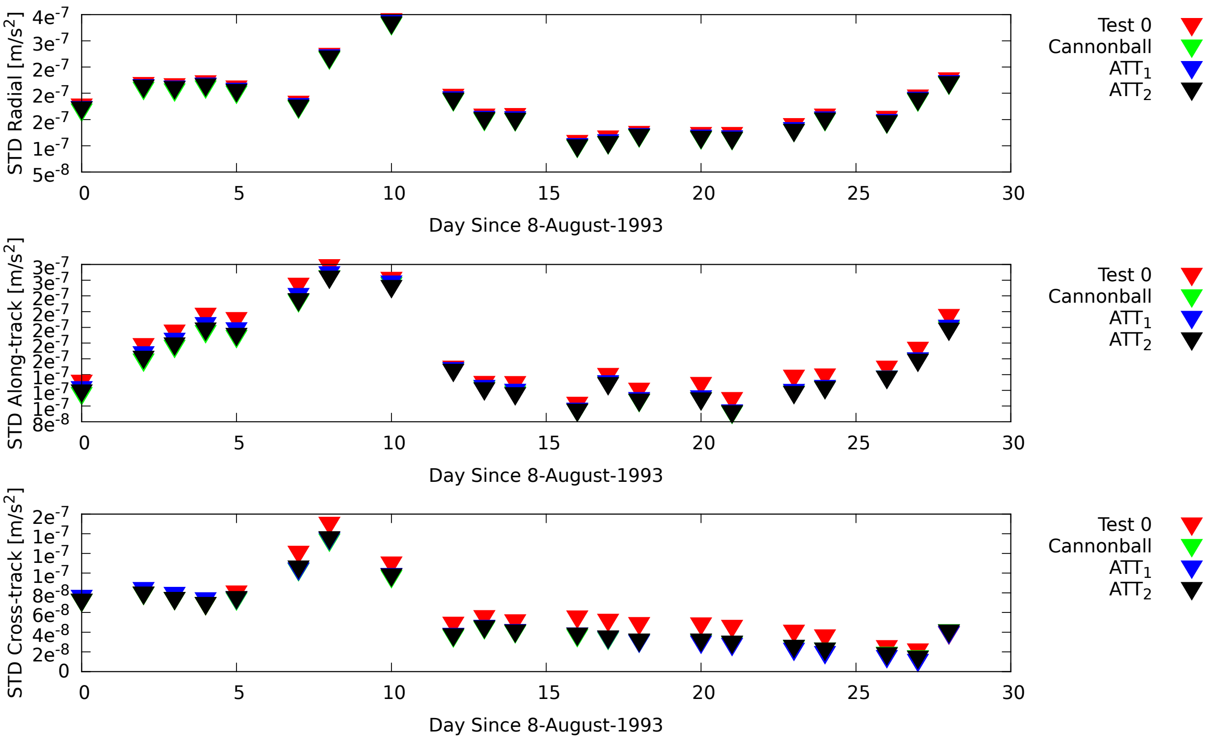

Figure 6.15: From Top: Comparison of the daily standard deviation of estimated PCAs for spacecraft model and attitude configuration in radial, along-track and cross-track direction for one month. Note that Test 0 is parametrized with PCAs and acceleration biases without surface forces.

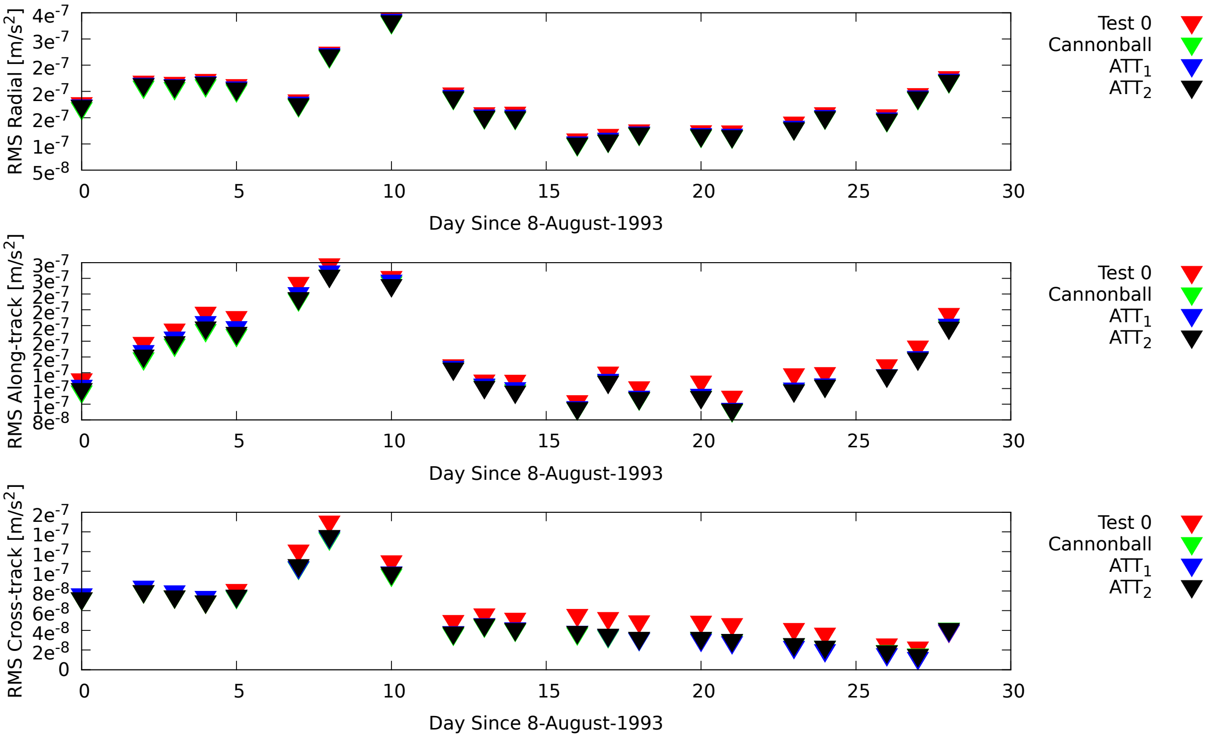

Figure 6.16: From Top: Comparison of the daily RMS values of estimated PCAs for spacecraft model and attitude configuration in radial, along-track and cross-track direction for one month. Note that Test 0 is parametrized with PCAs and acceleration biases without surface forces.

Now let us assess the quality of the surface forces. From all the figures above, it can be seen that the empirical biases and pseudo-stochastic PCAs have amplitudes that are comparable to those of the modeled surface accelerations even in the presence of surface forces. This further reinforces that fact that the implemented models for surface forces in this project are far from being perfect, due to which the parameters are still absorbing modeling defects. However, it is important to recall that SPICE orbits are being used as observations and the parameters are absorbing the differences in orbit modeling done for this project and that of SPICE, thereby attempting to reduce the differences in the estimated state vectors. Nevertheless, the scaling factors can aid in fine-tuning the non-gravitational forces in parallel with empirical and pseudo-stochastic parameters. As a start, one can estimate the scaling factors and then observe the amplitudes of estimated acceleration biases and PCAs (which should reduce in amplitudes for accurate modeling) with SPICE orbits as observations. Despite of this, if the amplitudes of the parameters do not reduce, then it is a clear indication that the orbit determination of Magellan also relies on additional empirical parametrization to fine-tune the dynamic models. Nevertheless, the impact of surface forces and spacecraft models on the orbits has not yet been discussed. In the next section, the impact of surfaces forces on orbit determination of Magellan is presented with real Doppler tracking data over longer arc length of 48 hours to allow the orbit errors (or differences) due to attitude build up over large time-span.

6.3.5. Doppler-based Orbit Determination

In Section 6.2, it was conveyed that the unconstrained estimation of empirical parameters in Bernese GNSS Software was not feasible for Doppler-based orbit determination of Magellan. As a result, a way-around was established to fine tune the incorrect apriori assumption of C_D and C_R without estimation of scaling factors. In this section only the results with "tuned" C_D are presented due to limited time for the project. First one drag scale factor, over the entire arc, is estimated by using SPICE orbit as observations, with only the drag force active. Subsequently, the estimated scaling factor value for each spacecraft model is multiplied by the fixed apriori $C_D = 1.25$ in the drag force model and Doppler-based orbit determination is done by estimating only the six initial conditions. The data arc, of 48 hours, chosen for this analysis comprises of SPICE (positions) and Doppler observations for Day 146 and 147 of 1994. These two days are chosen particularly because they have no discontinuities in SPICE positions, thereby indicating no suspicious maneuvers (see Section 6.1) that can complicate the analysis. For this project, only the orbits with "tuned" C_D are assessed for each spacecraft model and C_R is fixed to 1.4. The setup for Doppler-based orbit determination is as per Table 6.1.

For SPICE-based orbit determination, the data arc is parametrized with drag force and only the drag-coefficient is estimated over a data arc as an additional empirical parameter, for each spacecraft model. The resulting orbit fits are shown in the Figure 6.17:

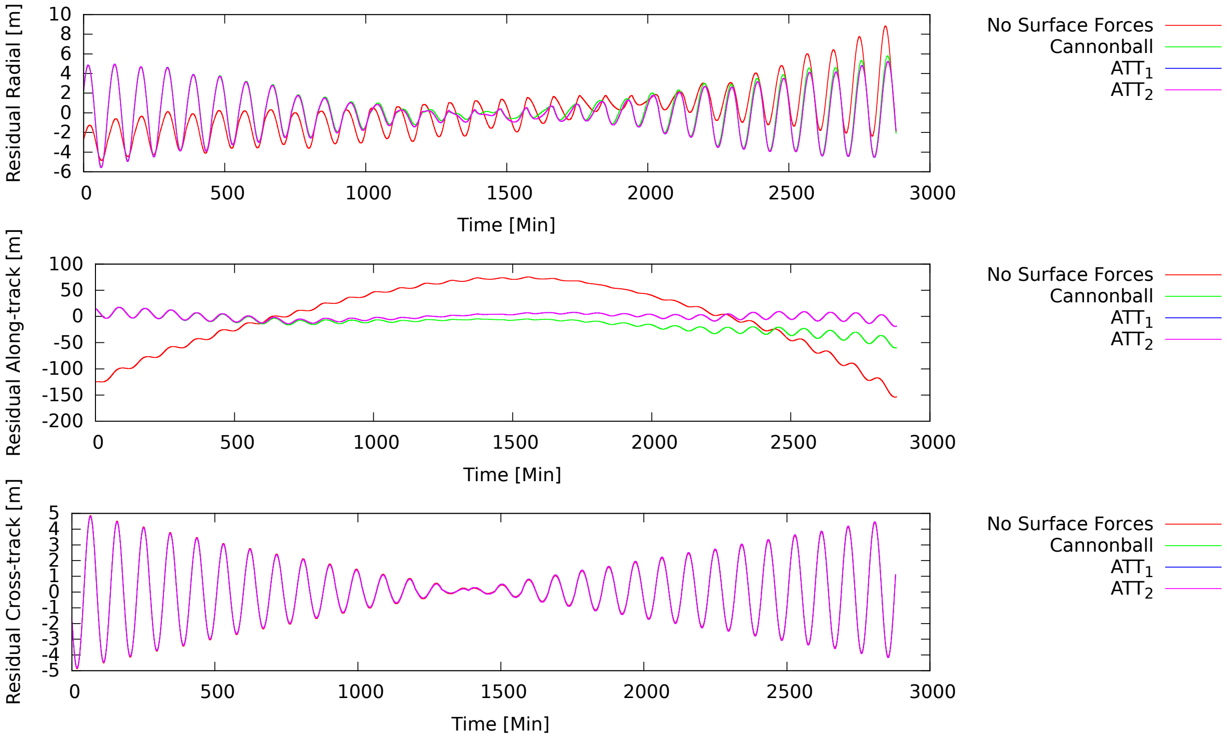

Figure 6.17: From Top: Comparison of the position residuals for spacecraft model and attitude configuration in radial, along-track and cross-track direction for data arc containing Day 146 and Day 147 with SPICE positions as observation. Note that a large part of the along-track error is removed by estimation of drag scaling factor. The residuals in radial and cross-track are significantly lower than those in the along-track.

It is expected that orbit in the along-track direction will show largest sensitivity to drag force. This is what's seen in Figure 6.17, where the residuals in the along-track direction reduce to about 30 m (RMS). However, this drastic reduction of residuals in along-track direction is mostly due to the fact that the drag scaling parameter is absorbing modeling defects in drag acceleration. A striking observation to be made is the better LSQ-fit of the orbits with ATT_1 and ATT_2 in the along-track direction, where the residuals are closely-scattered around zero in the second-half of the data arc. However, the most important part of this test is the knowledge of the estimated values of the drag-scale factor for each spacecraft model and attitude configuration. They are tabulated below:

Cannonball	ATT_1	ATT_2
-1.00916 ± 0.0002932	-1.02070 ± 0.0003545	-1.16126 ± 0.0004022

Table 6.7: Estimated values of drag scaling factors for each spacecraft model and attitude configuration for data arc containing Days 146 and 147 of 1994. The formal errors are shown to highlight stable parameter estimation. Note that the negative values are observed because SPICE orbits are used as observations. Furthermore, if we compare the above values with the that of Figure 6.7 (Days 292 an 293 starting from 8-August-1993 correspond to Days 146 and 147 of 1994) it can be observed that the days chosen for this data arc belong to those days between Days 200-300 with unrealistic parameter estimation that is characterized by negative values. The precise values of drag scaling factor and the formal errors, in Figure 6.7, for Day 146 and 147 are -0.688312 ± 0.0078473 and -1.00810 ± 0.0078496 respectively.

The fixed apriori $C_D = 1.25$ was multiplied with the estimated drag scaling factor values, given in Table 6.7, for each spacecraft model for Doppler-based orbit determination. The model performance was evaluated based on Doppler residuals and SPICE orbit comparison.

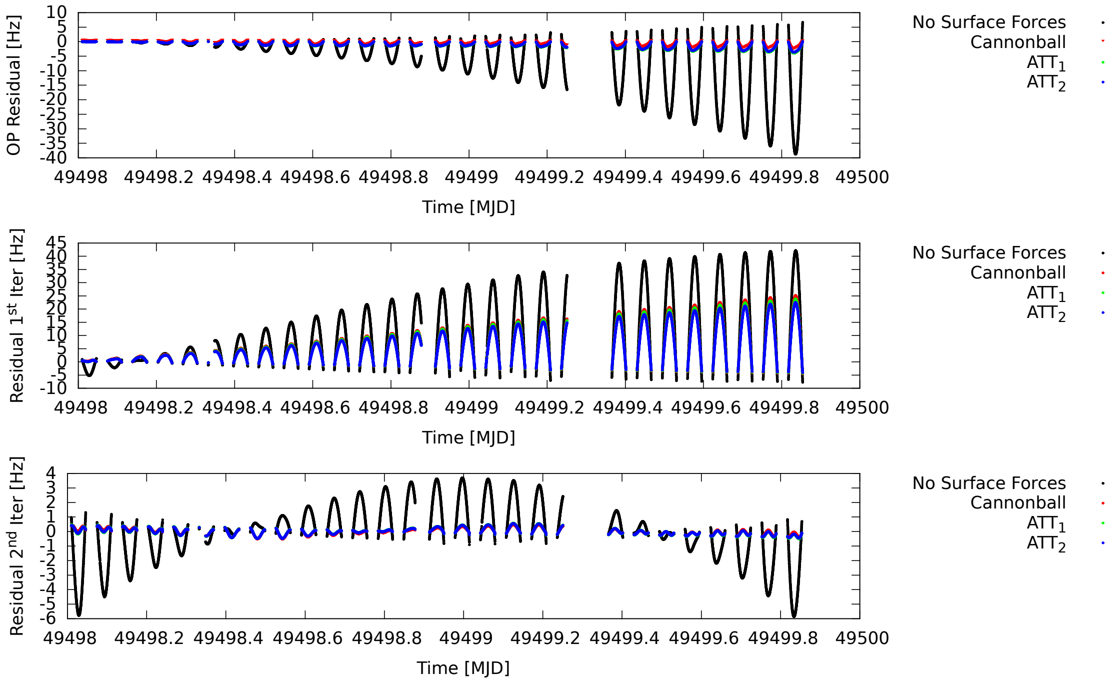

Figure 6.18: From Top: Comparison of the Doppler residuals for spacecraft model and attitude configuration, shown for each iteration. **OP:** Orbit Propagation.

The iterative algorithm for LSQ estimator adjusts the initial conditions (in the case of Doppler-based orbit determination, Keplerian elements) such that the square of the residuals is minimum (see Section 2.6 of Chapter 2). This iterative regime is continued till the adjustment in initial conditions becomes negligible for next iteration, which is an indication of convergence of the initial conditions. Keeping this in mind, it can be seen from Figure 6.18 that the Doppler residuals “shoot up” for the first LSQ-adjustment. This is possible due to the fact that estimation problem is not linear before the first LSQ-fit, as a result of which the estimator first adjusts the initial conditions so that they are in the linearity of LSQ estimation. On the other hand, the residuals in second LSQ-adjustment “settle down”, indicating that the orbits are now converging with respect to the newly adjusted initial conditions and the estimation problem is linear after the first LSQ-adjustment. For this test, it was observed that the adjustment in the initial conditions for third LSQ-adjustment translate to cm-level (not shown). Considering this small change, maximum of two LSQ-adjustments were allowed for Doppler-based orbit determination to save some processing time.

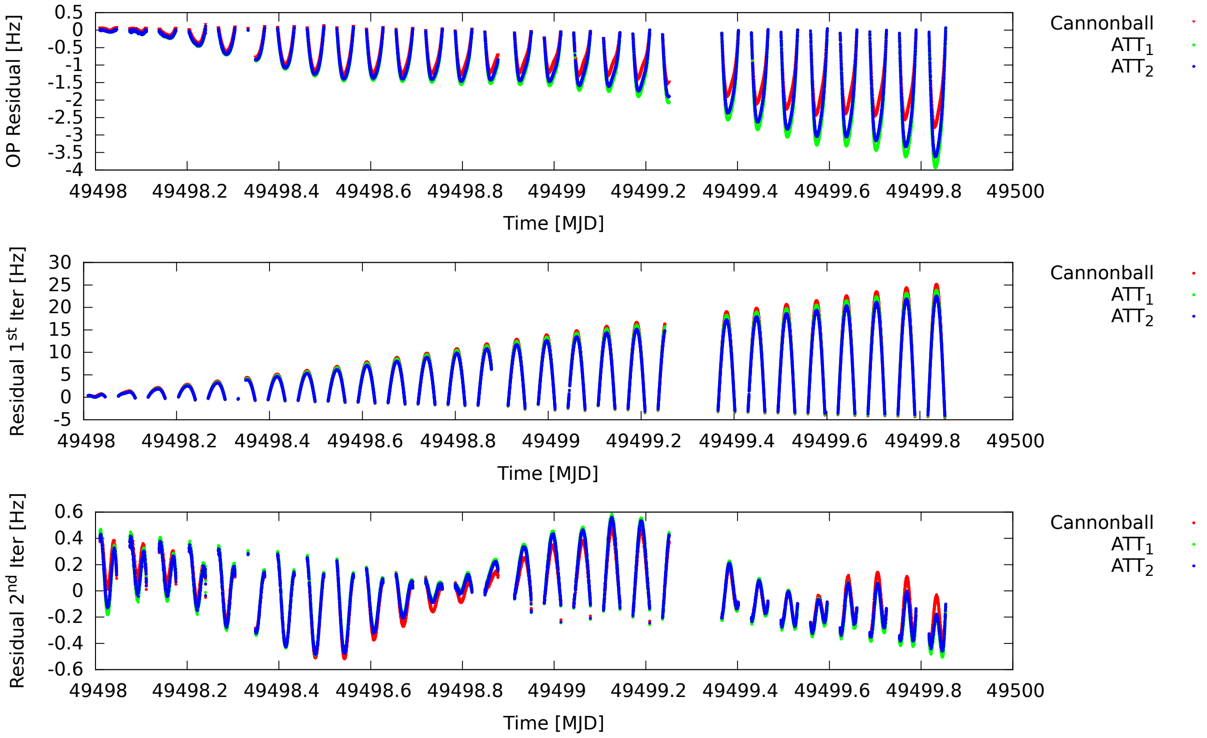

Figure 6.19: From Top: Relative comparison of the Doppler residuals for each spacecraft model and attitude configuration, shown for each iteration. **OP:** Orbit Propagation.

Statistics	No Surface Forces	Cannonball	ATT_1	ATT_2
Mean	-0.00114	0.00027	0.00024	0.00019
Standard Deviation	2.06433	0.21425	0.23624	0.22392
RMS	2.06420	0.21425	0.23623	0.22391

Table 6.8: Statistics of the Doppler residuals for second LSQ-adjustment.

By observing the second LSQ-adjustment in Figure 6.19, it can be seen that macro-model with ATT_2 gives the best residuals. To see it clearly, the statistics, given in Table 6.8, show that the statistical mean is minimum for macro-model with ATT_2. However, there are still large signatures present in the residuals that appear for every pass, indicating a presence of strong 1-CPR acceleration. Given that β-angle for this data arc is approximately -24^o, it is possible that this 1-CPR acceleration is acting in either radial or cross-track direction, perhaps due to SRP and R-PRP mis-modeling (or due to incorrect assumption of C_R).

By juxtaposing Figure 6.20 and Tables 6.9, 6.10, 6.11 it can be seen that the positions in radial, along-track and cross-track direction are improved the most for macro-model with ATT_2. However, a sign change in the along-track mean of the positions for all the spacecraft model indicate that the along-track component of the accelerations still miss some critical parametrization to absorb error in the mean, perhaps C_R or empirical constant along-track acceleration which is comparable to net surface acceleration in the same direction (see Figure 6.6 for the empirical acceleration magnitude). On the other hand, it is also possible that the freely estimated drag scaling factor values by using SPICE positions are absorbing a part of missing empirical parametrization, thereby leading to a negative drag scaling factor values, which may be unrealistic and can cause this shift in the mean. However, the fact that ATT_2 gives the lowest standard deviation, in position residuals, is a strong indicator that the macro-model with ATT_2 is able to superiorly "capture" the temporal details of surface forces. Nevertheless, the large standard deviations, of up to 2 km, in cross-track direction for all the tests with surface forces indicate an error in orientation of orbital plane (or orbital inclination) which is could be due to mis-modeling in radiation accelerations, or incorrect assumption of C_R.

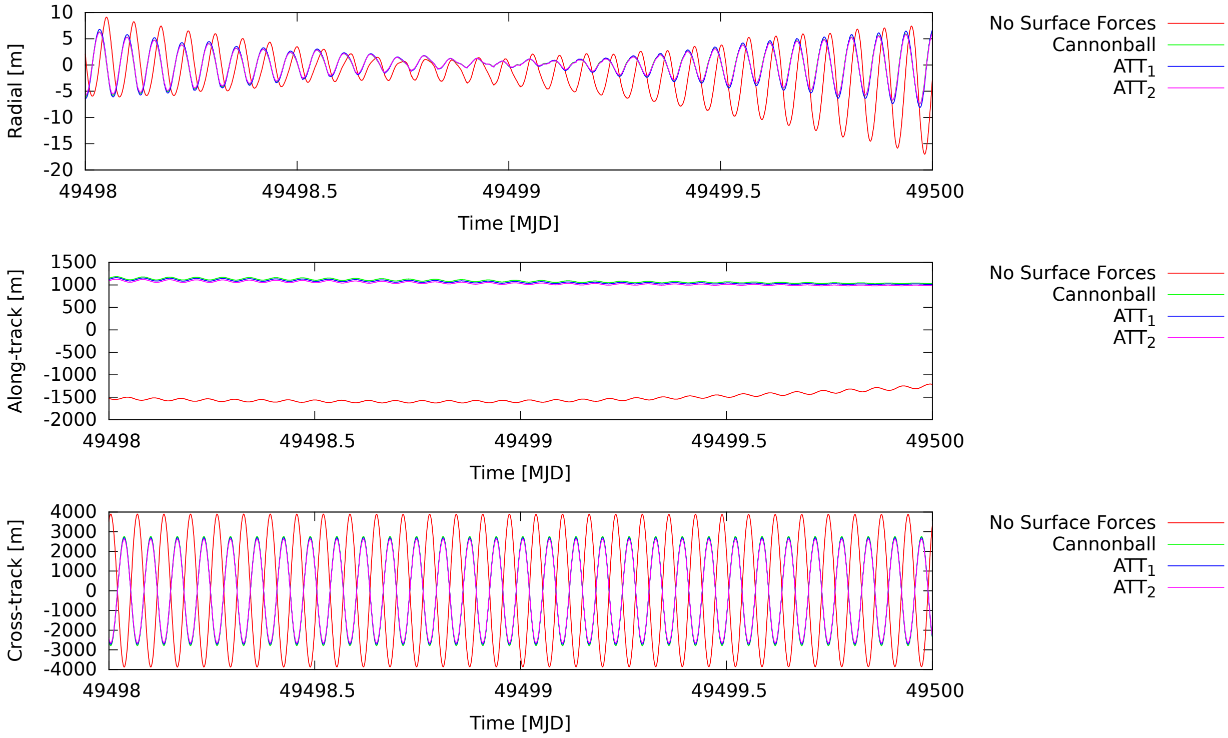

Figure 6.20: From Top: Comparison of the position residuals with respect to SPICE orbits.

Statistics	No Surface Forces	Cannonball	ATT_1	ATT_2
Mean	-1.62	0.09	0.09	0.10
Standard Deviation	4.67	2.59	2.82	2.55
RMS	4.94	2.60	2.82	2.55
Maximum Value	9.11	6.30	6.79	6.23
Minimum Value	-16.98	-7.36	-8.06	-7.32

Table 6.9: Statistics of position residuals in radial direction when compared with SPICE orbits.

Statistics	No Surface Forces	Cannonball	ATT_1	ATT_2
Mean	-1517.16	1088.82	1063.50	1034.11
Standard Deviation	97.75	41.28	39.91	38.91
RMS	1520.31	1089.60	1064.25	1034.84
Maximum Value	-1205.91	1183.82	1160.06	1126.78
Minimum Value	-1625.99	1026.72	1007.92	978.56

Table 6.10: Statistics of position residuals in along-track direction when compared with SPICE orbits.

Statistics	No Surface Forces	Cannonball	ATT_1	ATT_2
Mean	20.44	-14.74	-14.39	-14.00
Standard Deviation	2738.57	1959.81	1913.82	1861.10
RMS	2738.17	1959.52	1913.55	1860.83
Maximum Value	3893.76	2761.80	2696.94	2622.60
Minimum Value	-3866.86	-2781.96	-2716.66	-2641.80

Table 6.11: Statistics of position residuals in cross-track direction when compared with SPICE orbits.

While analyses of macro-model performance over one data arc cannot be sufficient, it can now be understood that the orbit is highly sensitive to the non-dimensional coefficients, namely C_D and C_R, that highlights the role of scaling factors estimation in improving the non-gravitational force modeling by fine-tuning the coefficients with LSQ-adjusted scaling parameters. This fact is also supported by a quantitative comparison of the statistics between setup with no-surface forces and setups with surface forces (with different spacecraft model), that shows the relative change in position residual is the largest when surface forces are introduced in the orbit modeling. This confirms that the accuracy of the orbit is more dependent on the quality of implemented surface forces than on the choice of spacecraft model and attitude assumption. This was also inferred from the empirical and pseudo-stochastic parametrization test in Section 6.3.4 where large changes in statistical properties of the additional parameters are observed as soon as surface forces are activated.

Regarding the impact of spacecraft model and attitude assumption on the orbits, by comparing the statistics of estimated orbits for spacecraft model and attitude assumption (see Tables 6.9, 6.10, 6.11), it is clear that macro-model with ATT_2 performs the best in modeling the drag force for this particular data arc, thereby leading to an absolute improvement of approximately 500 m (3D RMS) in along-track direction and about 100 m (3D RMS) improvement over cannonball model. Furthermore, orbits with ATT_2 show improvements in all directions. If this was true for all the days, then the attitude assumption of maximum power output is indeed close to the absolute truth of Magellan's attitude. Nevertheless, from Table 6.7, a large scaling factor magnitude of 1.16 (13% larger than cannonball) indicates that the assumed value of $C_D = 1.25$ underestimates the drag acceleration for ATT_2 with solar panels strictly pointed towards the Sun. This also highlights that the choice of attitude assumption affects the exposed surface area and panel orientation, which has an impact on the form factor of spacecraft and consequently on C_D. Nevertheless, the lowest standard deviation in position for ATT_2 in all directions show that the macro-model with maximum power output assumption is able to model the surface forces better than the other spacecraft models for this arc. However, a word of caution to be mentioned is that the test setup is still incomplete without "tuning" of C_R and without performing Doppler-based orbit determination over several data arcs. Furthermore, a negative value of drag scaling factor adds against the validity of this test as the value may be unrealistic. Nevertheless, by this test, we now know a starting point on how to asses the performance of spacecraft model with Doppler observations by using the scaling factors. As a further step, one must estimate scaling factors for all the surface forces, for each spacecraft model and attitude assumption, over several data arcs. Subsequently one must compare the scaling factors, which should be close to unity for a better model performance. Just as the analysis of position differences in this section, one can observe the improvements in the position errors to get a convincing evidence of which attitude assumption (or spacecraft model) is the best.

6.4. Discussion

Several challenges and open issues were identified through this project. First, a bug in the Doppler routine was identified that introduced a bias in the computed values of Doppler observations, that was not visible in the previous uses of code. In order to fix this, independent validation tests was required for which the light-time computations were compared to that from the external software. From Figure 6.1, it can be seen that simulated Doppler residuals with SPICE orbit, for Day 122 of 1994, are in excellent agreement with that of CNES' GINS orbit determination software, thereby confirming an affirmative validation of the correctness in Doppler modeling. Subsequently, the ramp errors, as one observed in Figure 6.3, posed another challenge to select healthy data arcs while processing tracking data pertaining to gravity cycle. While it has been suggested by Konopliv et al., [1999] that this can be fixed by increasing or decreasing ramp rates by up to 0.000005 Hz/s, this has not been explored in this project and the tracking data above a certain threshold have been eliminated, that also leads to exclusion of observations that are affected due to ramp error. In order to maximize gravity recovery, it is recommended to explore strategies to fix the ramp errors as it has been observed that some consecutive days are affected by ramp-errors and this may pose a challenge while processing in longer data arcs, as this leads to smaller number of observations.

It has been discussed that hide maneuvers and AMD events occur at least once every orbit. Hide maneuvers, in particular, tend to modify the magnitude of SRP accelerations for an instance over which hide maneuver is taking place. In order to realize the importance of hide maneuvers in non-gravitational force modeling, the acceleration biases were estimated over an entire gravity cycle by using SPICE positions as observations. From Figure 6.4, a systematic cyclic variation was observed for the daily value of radial acceleration bias for the gravity phase of the mission. Furthermore, by fitting the daily values of acceleration biases to a polynomial and then plotting them as function of β-angle, it was observed that the radial bias exhibits a strong correlation with β-angle and this can be seen in Figure 6.6. However, it is not conclusive whether this correlation exists solely due to hide maneuver or due to mis-modeling of radiation pressure in SPICE orbits. Konopliv et al., [1996] highlight that the SRP solutions (or estimation of C_R) for Magellan arc are poorly determined (meaning that the apriori uncertainty/formal error is not reduced). As a part of their future outlook while developing of 90 D/O gravity field, Konopliv et al., [1996] affirm that the next Venusian gravity recovery studies shall be supported with improved spacecraft modeling. However, it is unclear from the literature for state-of-the art 180 D/O gravity field model whether a detailed spacecraft modeling was incorporated [6], [4]. As a result, one must be aware of the possibilities of SRP-related errors in the gravity field model (SHGJ180U) itself. Furthermore, from the same figure, it can be seen that the magnitude of biases is an order of magnitude larger in radial and cross-track direction than in along-track direction and are of the magnitude $10^{-6}\ m/s^2$, which is comparable to the non-gravitational accelerations. Since SPICE orbits yield minimum Doppler residuals, it is important to add empirical accelerations in orbit parametrization to model the hide maneuvers (or to absorb mis-modeling errors due to radiation pressures) if one expects orbits as close to SPICE.

It was expected that the empirical parameters, namely acceleration biases and scaling factors shall not only aid in assessing the quality of non-gravitational force models, but also absorb any modeling deficiency and additional accelerations due to maneuvers. However, the empirical parameters are estimated freely in Bernese GNSS Software, resulting into either unrealistic values of the estimated empirical parameters, or severe degradation of the orbit solutions. Nevertheless, the low value of formal errors in estimated scaling factors for most of the daily arcs, as shown in Figure 6.7, indicates a stable estimation of empirical scaling factors, which is also the case for acceleration biases. However, the need to obtain realistic values of empirical parameters enforces the necessity to constrain the extent to which the values of empirical parameters can be estimated. However, a strategy to constrain the empirical parameters has not been explored in this project and of course can be treated as possible future improvements. Nevertheless, it is important to mention that several attempts were made to choose the best orbit parametrization. The impulses due to AMD events were modeled by estimating pseudo-stochastic pulses for every 60 minutes, i.e. at least once per orbit, and were constrained to 5 mm/s as per the inferences made from [4]. While the orbits exhibited convergence that was as close as 200 m to SPICE orbits, the Doppler residuals were still larger than that for SPICE. Furthermore, tests were also conducted by estimating 1-CPR empirical acceleration in radial, along-track and cross-track direction in addition to the pseudo-stochastic pulses. However, it is likely that free-estimation of 1-CPR accelerations led to singularity in their estimated values in the first LSQ fit, thereby leading to unstable estimation of parameters and initial conditions. Considering the inconclusiveness of the tests done with empirical 1-CPR and pseudo-stochastic pulses, the results have not been shown in this report. As a result, the Doppler-based orbit determination is restricted by a purely dynamic orbit model with all the surface forces active and with “tuned” values of C_D for each spacecraft model and a fixed $C_R = 1.4$, while restricting the parameter estimation to initial conditions.

The impact of non-gravitational modeling and choice of spacecraft model was assessed by two different approaches: 1) Analysis of empirical constant acceleration bias and pseudo-stochastic PCAs with SPICE orbits as observations, and 2) Analysis of Doppler-based orbit determination. For the first approach, the estimated empirical acceleration biases and PCAs for each spacecraft model, over one month starting from 8-August-1993, were compared to those of setup with surface forces inactive. For the second approach, the drag scaling factor for each spacecraft model and attitude assumption was estimated along with six initial conditions over a data arc containing Days 146 and 147 of 1994 with SPICE positions as observations. Subsequently, the drag scale estimate, corresponding to each spacecraft model, was multiplied with fixed $C_D = 1.25$ in the drag model and the estimation of only the six initial conditions was done with Doppler observations. The statistical properties of PCAs and acceleration biases, from Figures 6.14, 6.15, and 6.16 show that the parameters are more sensitive to the modeling of non-gravitational forces than to the choice of spacecraft model and attitude assumption. This is further supported by Doppler-based orbit determination test where the presence of surface forces, irrespective of the spacecraft model, has larger impact on the orbits and Doppler residuals than the spacecraft models (see Figures 6.18, 6.19, 6.20). As a result, the first crucial step is to focus on improving the non-gravitational force modeling by using powerful empirical parameters, such as scaling factors, to tune the model parameters (particularly, tune C_D and C_R). Subsequently, any additional accelerations due to maneuvers or secondary acceleration errors arising from mis-modeling of surface forces can be modeled with empirical accelerations such as constant biases and 1-CPRs. Once the modeling of surface forces is of sufficient quality, i.e. that gives the best Doppler residuals and positions, only then one can introduce macro-models with attitude assumptions, and can fine-tune it by observing the behavior of empirical parameters.

7

Conclusions & Recommendations

This chapter brings the reader to the end of this challenging project. In the framework of gravity recovery, the goal for this thesis was to answer the following low-level research question:

LQ1: How important are the surface force models in the orbit determination of Magellan?

To answer the above question, following objectives (OBJx) were defined for this research:

1. ***OBJ1: Verification and Validation of current implementation for non-gravitational forces in Bernese GNSS Software v5.3.***
2. ***OBJ2: Characterization of challenges in Doppler processing.***
3. ***OBJ3: Development and implementation of macro-model and attitude laws for Magellan.***
4. ***OBJ4: Investigation of the impact of surface forces and spacecraft model on orbit determination.***

In this chapter, first the conclusion in regards to the objectives shall be summarized, followed by an answer to **LQ1** based on the synthesis derived from the objectives. Finally, recommendations shall be given to support the future analysis of Magellan orbit determination in the framework of gravity recovery.

7.1. Conclusion

OBJ1: Verification and Validation of current implementation for non-gravitational forces

The goal of Verification was to confirm that the implemented surface forces show correct physical behavior. First, the modeling of drag acceleration was verified by observing the angle between Magellan's velocity vector with respect to atmosphere and the resultant drag acceleration vector, which should be exactly equal to 180^o. From Figure 5.1, it can be confirmed that drag acceleration has been implemented correctly since the required angle stays 180^o with negligible double-precision numerical errors. Second, implementation of SRP model was verified by choosing a Day 131 of 1994 for which β-angle is close to zero and then confirming that the angle between SRP acceleration vector and spacecraft-Sun unit vector is 180^o, again with negligible numerical errors (see Figure 5.2). Third, implementation of R-PRP model was verified to be correct by observing the angle between SRP acceleration vector and R-PRP acceleration vector for a day with β-angle is close to zero. If implemented correctly, the angle between R-PRP and SRP acceleration vectors should be exactly equal to 180^o at that instant for which Magellan is exactly between Sun and Venus (see Figure 5.5). Finally, implementation of E-PRP model was verified by observing the angle between Magellan's position from Venus' center and E-PRP acceleration vector. In ideal case, this angle should be zero because E-PRP is directed radially away from the center of the planet. However, from Figure 5.6, small non-zero values of this angle are observed. This is due to the fact that the entire planetary surface is divided into small grids of 1^o resolution for modeling E-PRP acceleration. As a result, it is possible that Magellan sees girds with different intensities, depending on its location over Venus, that contribute towards the net E-PRP acceleration, thereby resulting into small inclination of E-PRP acceleration with respect to spacecraft's position.

The goal of Validation was to make sure that the implemented models for surface forces give expected magnitudes of accelerations. For this purpose, back of the envelope calculations were done for each surface force and the results were compared with the acceleration magnitudes of the modeled forces. A comparison of back of the envelope calculations to that of the modeled acceleration magnitudes show a close agreement, with possible differences mainly due to approximated calculations in the former.

Back of the envelope validations were further supported by orbit determination. For this purpose, two days, namely Day 220 of 1993 and Day 122 of 1994, were chosen to represent different orbit profile and impact of surface forces on the orbits were analyzed. It was observed that for Day 220 of 1993, the orbit improves, with respect to SPICE, when all the surface forces are present, with drag acceleration producing highest impact on the orbit. On the other hand, activating surface forces tend to slightly degrade the orbit on Day 122 of 1994. The possible explanation would be the different orbit parametrization in SPICE, done by Konopliv et al., [1999], for the chosen days that are also reflected on the initial conditions for both the days. Less sensitivity of orbit, on Day 122 of 1994, to the surface forces is an indicator of initial conditions from SPICE orbits that were aggressively parametrized during their estimation. This was further supported by orbit determination with empirical and pseudo-stochastic parameters estimation. PCAs when estimated with SPICE positions as observations confirm the presence of additional empirical accelerations for both the days (see Figures 5.20 and 5.21), even when surface forces are active. However, this interpretation can be dismissed with the fact that the surface forces, while being valid and correctly implemented, are still not perfect due to the incorrect assumptions of spacecraft physical specifications and/or non-dimensional force coefficients (C_D and C_R). It is expected that the estimated scaling factors, one for each surface force, should absorb these defects in the implemented models and give a clear picture of the modeling quality.

OBJ2: Characterization of challenges in Doppler processing.

Through literature studies and personal discussions with GSFC, NASA, it was quickly realized that processing Magellan's tracking data is not a straightforward task. However, in addition to the inherent problems, such as ramp errors, several other unforeseeable issues/bottlenecks were encountered, majority of which could not be resolved due to limited time of the project. Instead, the challenges in Doppler processing were characterized, one-by-one, as they were encountered during the course of this project and an attempt was made to resolve each bottleneck to the best of abilities. The detailed discussion of the challenges was presented in Section 6.1 of Chapter 6 and is summarized with their current status in Table 7.1.

Issue	**Probable Reason/ Source**	**Status**	**Recommendation (if any)**
Doppler Routine Bug	Incorrect Call of JPL planetary ephemeris	Fixed	-
Ramp Error	Truncation in ramp-rate during recording	Pending	Increase or decrease ramp rate as per [6]
Missing Acceleration	Required to model maneuvers	Pending	Add empirical acceleration biases
Unconstrained Empirical Parameters	Leading to unrealistic parameter estimation	Pending	Add the capability to constrain empirical parameters with apriori constraints

Table 7.1: A brief summary of the challenges in processing Magellan tracking data. The future investigations, with Bernese GNSS Software, need to address the pending bottlenecks for a successful gravity recovery. The reader is encouraged to read Section 6.1 for detailed discussion.

OBJ3: Development and implementation of macro-model and attitude laws for Magellan

The previous researches on Venusian gravity recovery restricted the spacecraft model to cannonball due to lack of information on Magellan's attitude and the physical properties. Considering this, one of the goals in this project was to use an extended macro-model, with moving solar panels, and implement attitude based on limited information on the orbit design of gravity phase (see Section 1.5). A 3D CAD model of Magellan was developed by using commercially available software Autodesk 360 with reference to the dimensions of the major components available in "The Magellan Venus Explorer's Guide", compiled by Young [1990] [54]. Based on the 3D CAD model, a 16-plate macro-model that specifies the plate-area of each surface component was created (see Table A.1 in Appendix for the macro-model plate specifications). To compensate for the lack of information on attitude, two assumptions were implemented and tested with the extended macro-model: ATT_1 assumes a minimum drag configuration that aligns the solar panels ($\pm X$) with the spacecraft's velocity vector, whereas ATT_2 assumes maximum power output that aligns the normal of the solar panel in the direction of the Sun. For both the attitude assumption, the HGA antenna ($+Z$) points towards Earth for DSN tracking. Regarding the optical properties of surface components, no information is available in the literature, as a result the values were assumed and no further refinement was attempted.

OBJ4: Investigation of the impact of surface forces and spacecraft model on orbit determination.

The impact of non-gravitational modeling and choice of spacecraft model was assessed with two different approach: 1) Analysis by empirical and pseudo-stochastic parameters with SPICE orbits as observations, and 2) Doppler-based orbit determination, with real tracking data as observations. For the first approach, the estimated empirical acceleration biases and PCAs for each spacecraft model, over one month starting from 8-August-1993, were compared to those of setup with surface forces inactive. For the second approach, the drag scaling factor for each spacecraft model and attitude assumption was estimated along with six initial conditions over a data arc containing Days 146 and 147 of 1994 of SPICE positions. Subsequently, the drag scale estimate, corresponding to each spacecraft model, was multiplied with fixed $C_D = 1.25$ and the estimation of only the six initial conditions was done with Doppler observations. For first approach, the statistical properties of PCAs and acceleration biases, from Figures 6.14, 6.15, and 6.16 show that the parameters are more sensitive to the modeling of non-gravitational forces than to the choice of spacecraft model and attitude assumption. This is further supported by Doppler-based orbit determination test (or the second approach), where the presence of surface forces, irrespective of the spacecraft model, has larger impact on the orbits than the spacecraft models and Doppler residuals (see Figures 6.18, 6.19, 6.20).

Speaking of choosing the favorable attitude assumption, a clear conclusion cannot be yet derived for two reasons: 1) a test with "tuned" C_D and C_R is not yet done, and 2) the test was not done for several data arcs, which could otherwise give a clear picture. Nevertheless, for the chosen data arc with Days 146 and 147, the Doppler-based orbit determination test with "tuned" C_D shows that macro-model with ATT_2 performs the best. This can be characterized by reduction in the RMS and standard deviation of position residuals (see Tables 6.9, 6.10 and 6.11). In particular, the reduction in standard deviation in the position residuals indicates an improvement in the modeling of temporal part of modeled surface forces.

LQ1: How important are the surface force models in the orbit determination of Magellan?

Speaking purely from orbit determination perspective, it can be seen from Figure 6.18 that the Doppler residuals are significantly less for each LSQ-adjustment when surface forces are active. Smaller Doppler residuals are strong indication of better estimation of initial conditions during LSQ-adjustment. Furthermore, the position residuals, given in Figure 6.20, show that the surface forces have immediate impact on the orbit determination. Significant reduction in standard deviation and RMS of position residuals, in along-track and cross-track direction, by introducing a simple surface force modeling with cannonball affirms that the precise orbit determination of Magellan is characterized by accurate modeling of the surface forces (see Tables 6.9, 6.10, and 6.11 for statistics). However, non-gravitational force models are often the largest source of errors in orbit determination. This is also true in case of Venus orbiters due to imperfect atmosphere models and lack of accurate physical properties of spacecraft, particularly C_D and C_R. However, these imperfections can be easily tuned by estimation of scaling factors for surface forces. It was indirectly shown through Doppler-based orbit determination in Section 6.3.5 that "scaled" values of C_D alone is capable of improving the orbits, where the Doppler residuals in the orbit propagation alone is significantly less than those for an orbit setup without surface forces. This means that, out of all the parameters for surface force accelerations, C_D and C_R are the most important parameters that determine the quality of non-gravitational force modeling. However, a concern regarding the unrealistic negative value of drag scaling factors arises, in Section 6.3.5 of Chapter 6, that suggests more work needs to be done for realistic estimation of scaling factors.

7.2. Recommendations

A thesis is never perfect but can serve as starting point for future investigations. Through this research, several challenges in data processing and orbit determination of Magellan were identified that need to be solved one-by-one before proceeding towards a successful gravity recovery. Several recommendations were briefly discussed, throughout this report, that can support future work in this domain, only the critical recommendations are summarized below.

1. **Constraining Empirical Parameters:** It was mentioned several times that Bernese GNSS freely estimates empirical parameters. This is rather counterintuitive since it has been observed through several tests, particularly with Doppler observations, that the empirical parameters, when freely estimated, absorb more errors than they should, thereby leading to a severe degradation of the orbit solutions. By having appropriate constraints enabled through Bayesian estimation, the future investigator can have better control over orbit parameterization which is expected to be different for different data arcs, depending on the nature of Magellan's orbit over a selected data arc.

2. **Solving Ramp Errors:** The ramp errors in the tracking data, observed for some days in the gravity phase, have been pointed out in Chapter 6. While Konopliv et al., [1999] suggest a way-around by increasing or decreasing ramp rates by up to 0.000005 Hz/s for incorrect ramps, this has not been verified and tested in this project and the future investigator must explore strategies to fix this inherent issue, perhaps estimate a frequency bias to absorb this error. Unfortunately for this project, the data above certain threshold in the residual (up to 0.02 Hz) have been treated as outliers during preprocessing. This is counterintuitive to process Magellan's DSN data for gravity recovery as it leads to less number of observations, that can otherwise be used to their full extent.

3. **Choosing Appropriate Rotation Elements:** The ambiguity in selection of rotation elements have been discussed in Section 4.3 Chapter 4. As an educated guess, it was thought that the solution of rotation elements derived by konopliv et al., [1999], as a part of gravity field model development, would be more compatible with the apriori gravity field model SHGJ180. However, a simple orbit fit comparison with the rotation elements tabulated in Table 4.3, show that for some days the rotation elements given by Konopliv et al., [1999] result in an orbit improvement of up to 500 m, whereas for some days a degradation of up to 1 km has been observed, when compared against the orbit with rotation elements given by Davis et al., [2005] (see Figure A.2). As a result, before starting with scientific analysis, it is important to explicitly choose the appropriate rotation elements.

4. **Explicit Surface Forces Comparison:** The validation of the implemented surface forces was done by a less elegant "back of the envelope" calculations. Initially, it was expected the validation will be done by comparing the time-series of modeled acceleration to that of an external source (e.g. GEODYNE orbit determination software by GSFC). Unfortunately, a timely procurement of the outputs from external sources was not possible and a primitive manual calculations were done to support the validation tests. An external comparison will provide more confidence in the implemented models for non-gravitational forces.

5. **Maneuver Handling:** Colloquially speaking, Magellan was a restless beast that performed 15 AMDs per 24 hours (1 for each orbit). The detailed information on AMD events are explicitly

available on PDS server of NASA and one can exploit this knowledge to efficiently handle maneuvers with pseudo-stochastic pulses. Furthermore, large maneuvers like hides and star calibration can be modeled with powerful empirical parameters like acceleration biases and 1-CPR. The estimated acceleration biases, with SPICE orbits as observations, show empirical constant accelerations that are up to $10^{-6}\ m/s^2$ with strong correlation of radial bias with β-angle (see Figure 6.6). Initially, it was thought that this correlation can be associated with the hide maneuvers (which also depend on the β-angle of the Sun). However, it was rather difficult to correlate hide-induced accelerations for extreme β-angles of $\pm 90^o$ during which it was expected that the cross-track accelerations will exhibit strong correlation with β-angle. Nevertheless, empirical acceleration biases provided a unique insight into the orbit parametrization of SPICE orbits and as an initial step, one can constrain the estimation of biases closely to the values observed with SPICE orbits.

6. **Attitude Improvement:** This is specifically for the investigators who are looking to improve non-gravitational force modeling by using macro-models. The attitude during hide maneuver is such that the HGA is pointing towards the Sun to protect the spacecraft bus. The exact duration and start-stop times of hides are exclusively documented in Venus gravity Handbook compiled by Konopliv et al., [1996]. With this information, it is possible to incorporate the change in attitude during hide maneuver by implementing conditional statements in the attitude that allows the macro-model to orient HGA towards the Sun during hide event. The properties of macro-model, in particular the optical and non-dimensional force coefficients and mass, can be improved further (or tuned) by adjusting them as per the estimated biases and scaling factors.

7. **Estimation Of Scaling Factors:** From Section 6.3.5, it can be seen that the Doppler-based orbit estimation is highly sensitive to C_D scaling factor. A similar test can be done with C_R scaling factor for each spacecraft model to know how sensitive are the non-gravitational force models to the radiation forces. Furthermore, by estimating C_D and C_R scaling factors over multiple days for each spacecraft model and attitude configuration, it can be possible to choose the best attitude assumption by observing for Doppler-based orbits, Doppler residuals and the estimated parameters.

Bibliography

[1] J. M. Boyce, Magellan mission to venus, (1990).

[2] N. F. de Groot, Radio frequency selection and interference prevention, in Deep Space Telecommunications Systems Engineering (Springer, 1983) pp. 517–555.

[3] W. Folkner, Dsn station locations and uncertainties, TDA Progress Report , 42 (1996).

[4] A. Konopliv, W. Banerdt, and W. Sjogren, Venus gravity: 180th degree and order model, Icarus **139**, 3 (1999).

[5] P. K. Seidelmann, B. A. Archinal, M. F. A'hearn, A. Conrad, G. Consolmagno, D. Hestroffer, J. Hilton, G. Krasinsky, G. Neumann, J. Oberst, et al., Report of the iau/iag working group on cartographic coordinates and rotational elements: 2006, Celestial Mechanics and Dynamical Astronomy **98**, 155 (2007).

[6] A. S. Konopliv and W. L. Sjogren, Venus gravity handbook, (1996).

[7] L. Cerri and P. Ferrage, DORIS satellites models implemented in POE processing, Tech. Rep. (SALP-NT-BORD-OP-16137-CN, 2012).

[8] D. T. Lyons, W. L. Sjogren, R. E. Lock, and R. S. Austin, Beyond aerobraking: Designing the magellan global gravity experiment, (1993).

[9] A. Jäggi, G. Beutler, and U. Hugentobler, Efficient stochastic orbit modeling techniques using least squares estimators, A Window on the Future of Geodesy , 175 (2005).

[10] J. C. Neuman, Solar thermal vacuum tests of magellan spacecraft, in 16th Space Simulation Conference: Confirming Spaceworthiness into the Next Millennium, Vol. 3096 (1991) p. 1.

[11] R. Saunders, A. Spear, P. Allin, R. Austin, A. Berman, R. Chandlee, J. Clark, A. Decharon, E. De Jong, D. Griffith, et al., Magellan mission summary, Journal of Geophysical Research: Planets **97**, 13067 (1992).

[12] J.-P. Barriot, N. Vales, G. Balmino, and P. Rosenblatt, A 180th degree and order model of the venus gravity field from magellan line of sight residual doppler data, Geophysical research letters **25**, 3743 (1998).

[13] B. C. Bigelow and A. M. Dressler, Imacs, the multiobject spectrograph and imager for magellan: a status report, in Instrument Design and Performance for Optical/Infrared Ground-based Telescopes, Vol. 4841 (International Society for Optics and Photonics, 2003) pp. 1727–1739.

[14] F. Lerch, C. Wagner, D. Smith, M. Andson, J. Brownd, and J. Richardson, Gravitational field models for the earth (gem 1 and 2), (1972).

[15] X. Liu, Global gravity field recovery from satellite-to-satellite tracking data with the acceleration approach, (2008).

[16] M. Ananda, W. Sjogren, R. Phillips, R. Wimberly, and B. Bills, A low-order global gravity field of venus and dynamical implications, Journal of Geophysical Research: Space Physics **85**, 8303 (1980).

[17] B. Williams, N. Mottinger, and N. Panagiotacopulos, Venus gravity field: Pioneer venus orbiter navigation results, Icarus **56**, 578 (1983).

[18] H. Niemann, R. Hartle, W. Kasprzak, N. Spencer, D. Hunten, and G. Carignan, Venus upper atmosphere neutral composition: Preliminary results from the pioneer venus orbiter, Science **203**, 770 (1979).

[19] G. Keating, R. Tolson, and E. Hinson, Venus thermosphere and exosphere: First satellite drag measurements of an extraterrestrial atmosphere, Science **203**, 772 (1979).

[20] S. K. Wong, T.-H. You, J. D. Giorgini, L. Lim, and P. Chadbourne, Navigating through the venus atmosphere, (1994).

[21] R. H. Lyon, Geosynchronous orbit determination using space surveillance network observations and improved radiative force modeling, Ph.D. thesis, Massachusetts Institute of Technology (2004).

[22] P. W. Kenneally, High Geometric Fidelity Solar Radiation Pressure Modeling via Graphics Processing Unit, Ph.D. thesis, University of Colorado at Boulder (2016).

[23] V. Girardin, Impact of non-gravitational forces on gps-based precise orbit determination of low earth orbiters, (2016).

[24] S. Goossens, F. G. Lemoine, P. Rosenblatt, S. Lebonnois, and E. Mazarico, Venus gravity field modeling from magellan and venus express tracking data, in Lunar and Planetary Science Conference, Vol. 48 (2017).

[25] M. Allen, G. Chin, et al., The vesper mission to venus, in Bulletin of the American Astronomical Society, Vol. 30 (1998) p. 1106.

[26] B. Schutz, B. Tapley, and G. H. Born, Statistical orbit determination (Academic Press, 2004).

[27] T. Strutz, Data fitting and uncertainty: A practical introduction to weighted least squares and beyond (Vieweg and Teubner, 2010).

[28] H. Bock, G. Beutler, and U. Hugentobler, Kinematic orbit determination for low earth orbiters (leos), in Vistas for Geodesy in the New Millennium (Springer, 2002) pp. 303–308.

[29] D. Hobbs and P. Bohn, Precise orbit determination for low earth orbit satellites, Annals of the Marie Curie Fellowships **4**, 128 (2006).

[30] A. Jäggi, U. Hugentobler, and G. Beutler, Pseudo-stochastic orbit modeling techniques for low-earth orbiters, Journal of Geodesy **80**, 47 (2006).

[31] J. Marshall, P. Antreasian, G. Rosborough, and B. Putney, Modeling radiation forces acting on satellites for precision orbit determination, in Astrodynamics 1991 (1992) pp. 73–96.

[32] E. Doornbos, Modeling of non-gravitational forces for ers-2 and envisat, Delft Institute for Earth-Oriented Space Research, Delft University of Technology, Delft, The Netherlands (2001).

[33] H. Bock, Efficient methods for determining precise orbits of low earth orbiters using the global positioning system, Vol. 65 (2003).

[34] P. Swatschina, Dynamic and reduced-dynamic precise orbit determination of satellites in low earth orbits, (2009).

[35] T. D. Moyer, Formulation for observed and computed values of Deep Space Network data types for navigation, Vol. 3 (John Wiley & Sons, 2005).

[36] A. Noureldin, T. B. Karamat, and J. Georgy, Basic navigational mathematics, reference frames and the earth's geometry, in Fundamentals of Inertial Navigation, Satellite-based Positioning and their Integration (Springer, 2013) pp. 21–63.

[37] D. A. Vallado, Fundamentals of astrodynamics and applications, Vol. 12 (Springer Science & Business Media, 2001).

[38] F. W. Taylor, The Scientific Exploration of Venus (Cambridge University Press, 2014).

[39] A. Mahieux, A. Vandaele, E. Neefs, S. Robert, V. Wilquet, R. Drummond, A. Federova, and J.-L. Bertaux, Densities and temperatures in the venus mesosphere and lower thermosphere retrieved from soir on board venus express: Retrieval technique, Journal of Geophysical Research: Planets **115** (2010).

[40] S. S. Limaye, S. Lebonnois, A. Mahieux, M. Pätzold, S. Bougher, S. Bruinsma, S. Chamberlain, R. T. Clancy, J.-C. Gérard, G. Gilli, et al., The thermal structure of the venus atmosphere: Intercomparison of venus express and ground based observations of vertical temperature and density profiles☒, Icarus **294**, 124 (2017).

[41] S. Tingle, The dynamics of the venusian mesosphere and thermosphere, (2011).

[42] H. Justh, C. Justus, and V. Keller, Global reference atmospheric models, including thermospheres, for mars, venus and earth, in AIAA/AAS Astrodynamics Specialist Conference and Exhibit (2006) p. 6394.

[43] D. R. Williams, Venus fact sheet, Tech. Rep. (Tech. rep., NASA, 2005. http://nssdc. gsfc. nasa. gov/planetary/factsheet/venusfact. html, 2005).

[44] G. Schubert, General circulation and the dynamical state of the venus atmosphere, Venus , 681 (1983).

[45] K. Sośnica, Determination of precise satellite orbits and geodetic parameters using satellite laser ranging (Astronomical Institute, University of Bern, Switzerland, 2014).

[46] E. Doornbos, Thermospheric density and wind determination from satellite dynamics (Springer Science & Business Media, 2012).

[47] O. Montenbruck and E. Gill, Satellite orbits: models, methods and applications (Springer Science & Business Media, 2012).

[48] K. F. Palmer and D. Williams, Optical constants of sulfuric acid; application to the clouds of venus? Applied Optics **14**, 208 (1975).

[49] K. McGouldrick, O. B. Toon, and D. H. Grinspoon, Sulfuric acid aerosols in the atmospheres of the terrestrial planets, Planetary and Space Science **59**, 934 (2011).

[50] P. Knocke, J. Ries, and B. Tapley, Earth radiation pressure effects on satellites, in Astrodynamics Conference (1988) p. 4292.

[51] S. Bertone, D. Arnold, A. Jäggi, G. Beutler, and L. Mervart, Grail gravity field determination using the celestial mechanics approach, (2014).

[52] J. Estefan and O. Sovers, A comparative survey of current and proposed tropospheric refraction-delay models for dsn radio metric data calibration, (1994).

[53] W. M. Folkner, J. G. Williams, D. H. Boggs, R. S. Park, and P. Kuchynka, The planetary and lunar ephemerides de430 and de431, Interplanet. Netw. Prog. Rep **196**, 1 (2014).

[54] C. Young, The magellan venus explorer's guide, (1990).

[55] K. F. Wakker, Fundamentals of astrodynamics (Delft University of Technology, 2015).

[56] J. J. Lissauer and I. De Pater, Fundamental planetary science: physics, chemistry and habitability (Cambridge University Press, 2013).

[57] F. Park and B. Ravani, Bezier curves on riemannian manifolds and lie groups with kinematics applications, Journal of Mechanical Design **117**, 36 (1995).

A

Appendix

A.1. ATT_1 Attitude Matrix Derivation

Any vector in one direction can be expressed as a linear combination of a vector in that direction and a unit vector that is perpendicular to that direction. Now let $\mathbf{e_x}$ and $\mathbf{V}$ be two vectors along X-axis of Magellan's local reference frame (see Figure 4.4). Thus, this can be further expressed as a sum of $\mathbf{V}$ and linear combination of $\hat{\mathbf{e_z}}$:

$$\mathbf{e_x} = \mathbf{V} + \alpha\hat{\mathbf{e_z}} \tag{A.1}$$

Now, taking dot product of eq. (A.1) with $\hat{\mathbf{e_z}}$, we get

$$0 = \mathbf{V}.\hat{\mathbf{e_z}} + \alpha$$

Therefore,

$$\alpha = -\mathbf{V}.\hat{\mathbf{e_z}}$$

Putting the value of α in eq. (A.1) and then normalizing the final expression, the unit vector in along X-axis, $\hat{\mathbf{e_x}}$ is given as:

$$\hat{\mathbf{e_x}} = \frac{\mathbf{V} - (\mathbf{V}.\hat{\mathbf{e_z}})\hat{\mathbf{e_z}}}{\sqrt{|\mathbf{V}|^2 - (\mathbf{V}.\hat{\mathbf{e_z}})^2}} \tag{A.2}$$

Eq. (A.2) defines the X-axis of Magellan along the velocity vector of the spacecraft. Furthermore, the Z-axis that passes through HGA can be defined by unit vector $\hat{\mathbf{e_z}} = \hat{\mathbf{r}}_{Earth}$, where $\hat{\mathbf{r}}_{Earth}$ is the distance between Earth and the spacecraft. Finally $\hat{\mathbf{e_y}}$ can be obtained by taking the cross product of $\hat{\mathbf{e_x}}$ and $\hat{\mathbf{e_z}}$. Please note that the implemented attitude assumptions are verified by confirming that the attitude matrix represents a rotation matrix, and when multiplied by its transpose yields an identity matrix.

A.2. Sensitivity Tests

A.2.1. JPL Ephemeris

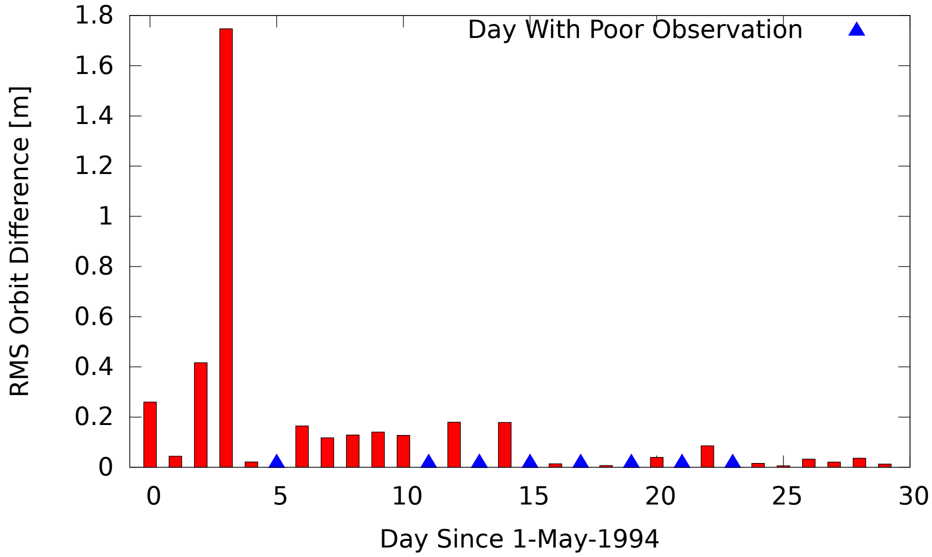

Figure A.1: Daily RMS of the orbit difference (3-dimensional) of Magellan when switching between JPL Ephemeris DE430 and DE421 over a period of one month. The orbit parametrization include only the gravity field, and Doppler data are used as observation. It can be seen that the choice of JPL Ephemeris has no significant impact on the estimated orbits.

A.2.2. Rotation Elements

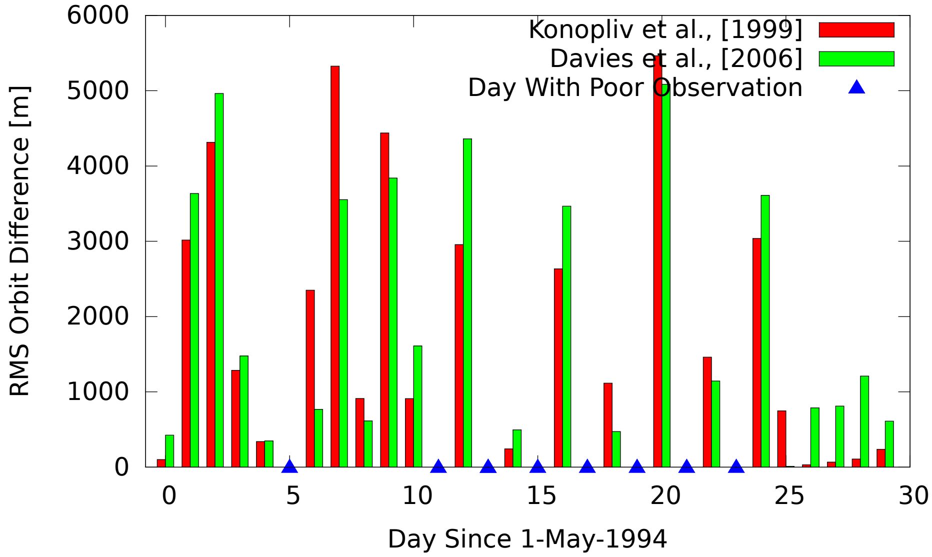

Figure A.2: Daily RMS of the orbit difference (3-dimensional) with respect to SPICE orbits between cartographic coordinates and rotation elements of *Konopliv et al., [2006]* and *Davies et al., [1999]* (see Table 4.3). The orbit parametrization, for both the comparison, include only the gravity field, and Doppler data are used as observations. It can be seen that the daily comparisons are ambiguous, thereby leading to an inconclusive result for the choice of rotational elements. It is to be noted that the RMS differences of the orbits for both the test cases are large when compared to SPICE orbits, which is mainly due to poor orbit modeling.

A.3. Macro-model File

SVN	N	A $[m^2]$	$\hat{\mathbf{n}}_2$	$\hat{\mathbf{n}}_1$	$\hat{\mathbf{n}}_2$	$\epsilon_{s,IR}$	$\epsilon_{d,IR}$	$\epsilon_{s,VI}$	$\epsilon_{d,IR}$	ϵ_{IR}	T $[K]$	Comment
18	1	1.539000	1.0	0.0	0.0	0.63	0.20	0.71	0.22	0.8	300.0	Bus 1
18	2	1.675800	0.0	-1.0	0.0	0.63	0.20	0.71	0.22	0.8	300.0	Bus 2
18	3	1.539000	-1.0	0.0	0.0	0.63	0.20	0.71	0.22	0.8	300.0	Bus 3
18	4	1.675800	0.0	1.0	0.0	0.63	0.20	0.71	0.22	0.8	300.0	Bus 4
18	5	6.321500	0.0	0.0	-1.0	0.03	0.16	0.05	0.30	0.8	300.0	Solar Panel 1, Front
18	6	6.321500	0.0	0.0	1.0	0.40	0.26	0.23	0.15	0.8	300.0	Solar Panel 1, Back
18	7	6.321500	0.0	0.0	-1.0	0.03	0.16	0.05	0.30	0.8	300.0	Solar Panel 2, Front
18	8	6.321500	0.0	0.0	1.0	0.40	0.26	0.23	0.15	0.8	300.0	Solar Panel 2, Back
18	9	1.297863	-0.38269	-0.92388	0.0	0.63	0.20	0.71	0.22	0.8	300.0	Equipment Bus 1
18	10	1.297863	0.38269	-0.92388	0.0	0.63	0.20	0.71	0.22	0.8	300.0	Equipment Bus 2
18	11	1.297863	0.92388	-0.38269	0.0	0.63	0.20	0.71	0.22	0.8	300.0	Equipment Bus 3
18	12	1.297863	0.92388	0.38269	0.0	0.63	0.20	0.71	0.22	0.8	300.0	Equipment Bus 4
18	13	1.297863	0.38269	0.92388	0.0	0.63	0.20	0.71	0.22	0.8	300.0	Equipment Bus 5
18	14	1.297863	-0.38269	0.92388	0.0	0.63	0.20	0.71	0.22	0.8	300.0	Equipment Bus 6
18	15	1.297863	-0.92388	0.38269	0.0	0.63	0.20	0.71	0.22	0.8	300.0	Equipment Bus 7
18	16	1.297863	-0.92388	-0.38269	0.0	0.63	0.20	0.71	0.22	0.8	300.0	Equipment Bus 8

Table A.1: Bernese spacecraft macro-model file for Magellan. **SVN:** Satellite Vehicle Number.

A.4. RMS Fit Using PCAs

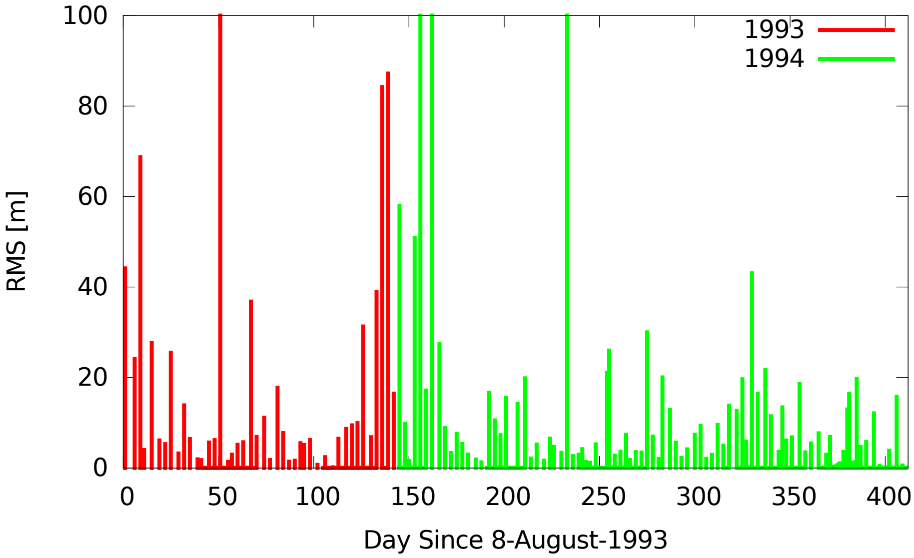

Figure A.3: RMS orbit differences (3-dimensional) with respect to SPICE orbits for an entire gravity phase (Cycle 5 and Cycle 6). Non-gravitational forces are switched off and only PCAs and acceleration biases are estimated with initial conditions. Note that large RMS (20 m or more) values for some days are ether due to discontinuities in the positions or due to poor parameter estimation.

A.5. Supplement To Section 6.3.4

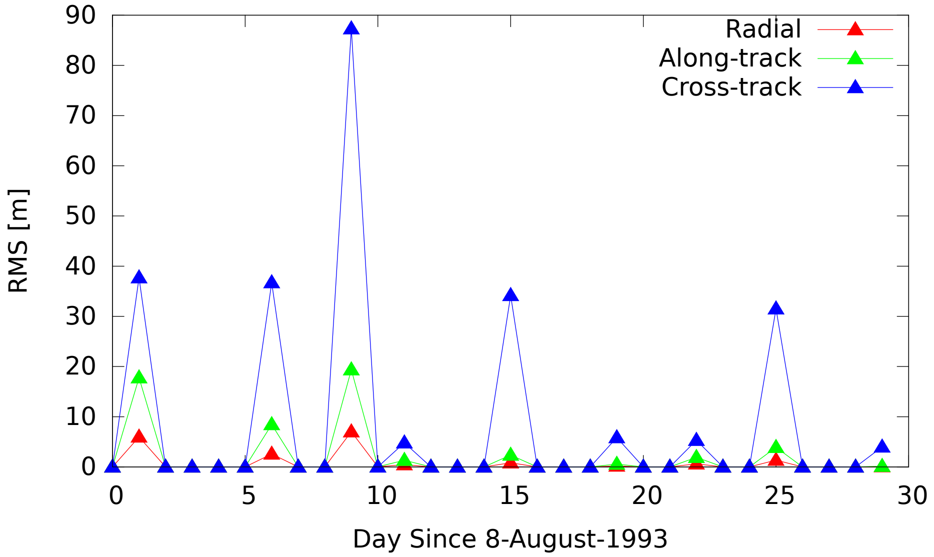

Figure A.4: RMS orbit differences with respect to SPICE in radial, along-track and cross-track direction. Note the large RMS values for some days that have discontinuities in the positions.

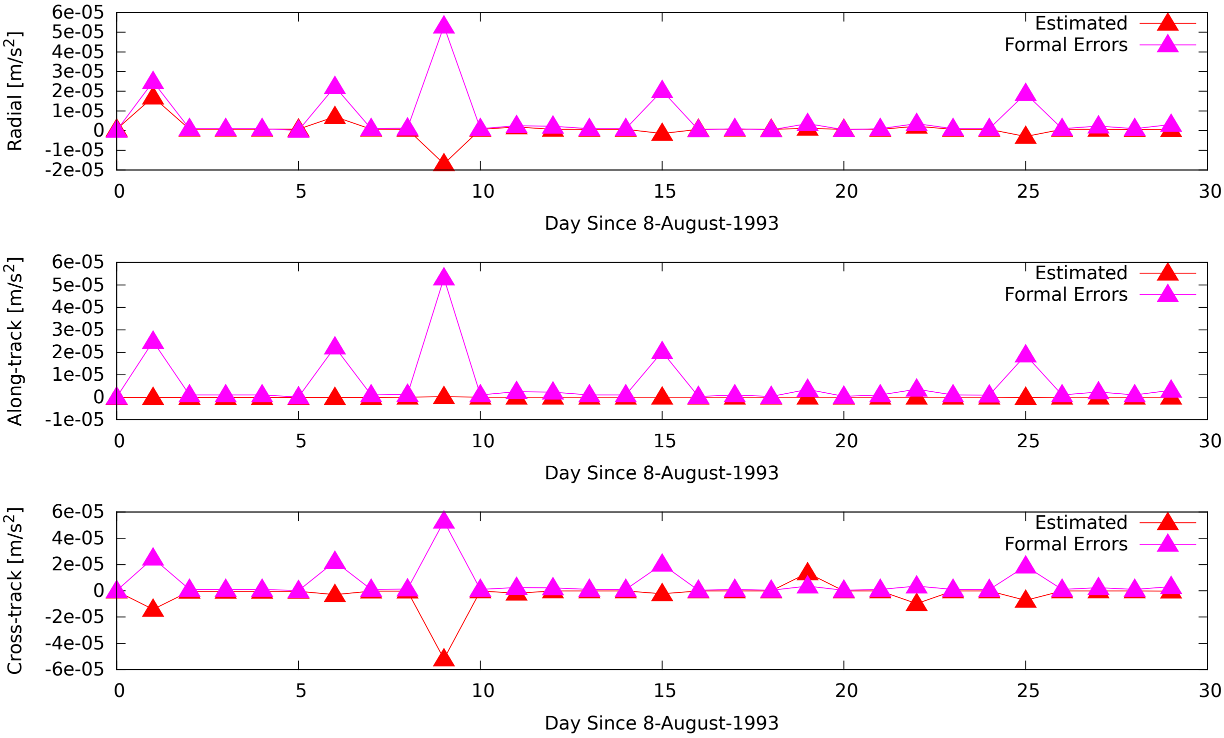

Figure A.5: Estimated empirical acceleration bias and its formal error in radial, along-track and cross-track direction. The formal errors are an order of magnitude less than the estimated values. Note that the estimated values and the formal errors for the days with discontinuities in the positions are high. As a result, such days are excluded from scientific analysis.